

FACULTY
OF MATHEMATICS
AND PHYSICS
Charles University

1

BACHELOR THESIS

2

Martin Vavřík

3

**Simulation and Reconstruction
of Charged Particle Trajectories
in an Atypic Time Projection Chamber**

4

5

Institute of Particle and Nuclear Physics

6

Supervisor of the bachelor thesis: Mgr. Tomáš Sýkora, Ph.D.

7

Study programme: Physics

8

Prague 2025

- ⁹ I declare that I carried out this bachelor thesis independently, and only with the
¹⁰ cited sources, literature and other professional sources. It has not been used to
¹¹ obtain another or the same degree.
- ¹² I understand that my work relates to the rights and obligations under the Act
¹³ No. 121/2000 Sb., the Copyright Act, as amended, in particular the fact that the
¹⁴ Charles University has the right to conclude a license agreement on the use of this
¹⁵ work as a school work pursuant to Section 60 subsection 1 of the Copyright Act.

In date
Author's signature

¹⁶ Dedication.

Title: Simulation and Reconstruction of Charged Particle Trajectories in an Atypical Time Projection Chamber **Added hyphen to avoid overfull hbox**

Author: Martin Vavřík

Institute: Institute of Particle and Nuclear Physics

Supervisor: Mgr. Tomáš Sýkora, Ph.D., Institute of Particle and Nuclear Physics

Abstract: Abstract.

Keywords: key words

¹⁷ Contents

¹⁸	Motivation	³
¹⁹	0.1 ATOMKI Anomaly	³
²⁰	0.1.1 ATOMKI Measurements	³
²¹	0.1.2 Other Experiments	⁴
²²	0.2 X17 Project at IEAP CTU	⁷
²³	1 Time Projection Chamber	⁹
²⁴	1.1 Charge transport in gases	⁹
²⁵	1.1.1 Drift	¹⁰
²⁶	1.1.2 Diffusion	¹¹
²⁷	1.2 Examples of TPCs	¹²
²⁸	1.2.1 The original TPC at PEP-4 at SLAC	¹²
²⁹	1.2.2 ALICE TPC	¹²
³⁰	1.2.3 CERES/NA45 radial-drift TPC	¹³
³¹	1.2.4 Other interesting radial-drift TPCs	¹⁵
³²	1.3 Readout	¹⁶
³³	1.3.1 Multi-Wire Proportional Chamber	¹⁶
³⁴	1.3.2 Micro-Pattern Gaseous Detectors	¹⁷
³⁵	1.4 Orthogonal Fields TPC at IEAP CTU	¹⁹
³⁶	1.4.1 Motivation and Associated Challenges	²⁰
³⁷	1.4.2 Coordinate Systems and Dimensions	²⁰
³⁸	1.4.3 Magnetic Field Simulation	²²
³⁹	2 Track Simulation	²⁶
⁴⁰	2.1 Microscopic Simulation	²⁶
⁴¹	2.1.1 First testing track	²⁷
⁴²	2.1.2 Grid-like testing sample	²⁷
⁴³	2.2 Runge-Kutta Simulation	²⁷
⁴⁴	2.2.1 Testing sample	³⁰
⁴⁵	3 Track Reconstruction	³²
⁴⁶	3.1 Reconstruction Assuming Steady Drift	³²
⁴⁷	3.2 Ionization Electron Map	³³
⁴⁸	3.2.1 Gradient Descent Algorithm	⁴⁰
⁴⁹	3.2.2 Interpolation on the Inverse Grid	⁴¹
⁵⁰	3.3 Discrete Reconstruction	⁴³
⁵¹	4 Energy Reconstruction	⁴⁵
⁵²	4.1 Cubic Spline Fit	⁴⁵
⁵³	4.2 Circle and Lines Fit	⁴⁷
⁵⁴	4.2.1 Two-dimensional fit	⁴⁸
⁵⁵	4.2.2 Three-dimensional fit	⁴⁹
⁵⁶	4.2.3 Testing on a Runge-Kutta sample	⁵²
⁵⁷	4.3 Runge-Kutta Fit	⁵²
⁵⁸	4.3.1 Testing on a microscopic sample	⁵⁵

59 Conclusion	56
60 Bibliography	60
61 List of Abbreviations	69

62 Motivation

63 Or chapter 1? MFF UK thesis template uses Introduction as an unnumbered
64 chapter, but it's not clear how they handle numbering inside the chapter. A Time
65 Projection Chamber (TPC) [refs] is a gaseous detector that reconstructs charged
66 particle trajectories by measuring the positions and drift times of ionization elec-
67 trons (and sometimes also ions) created in the gas. The energies of these particles
68 can be inferred from the curvatures of their trajectories in a magnetic field.

69 The goal of this thesis is to develop an algorithm for the reconstruction of
70 charged particle trajectories and energy in an *atypic* TPC with orthogonal elec-
71 tric and magnetic fields, hereafter referred to as the Orthogonal Fields TPC
72 (OFTPC), used in the X17 project at the Institute of Experimental and Ap-
73 plied Physics, Czech Technical University in Prague (IEAP CTU). Furthermore,
74 we present the results of testing of several (gradually improving) developed algo-
75 rithms with different samples of simulated data. Put this somewhere, (maybe just
76 the abstract?). We use the Garfield++ toolkit [1] for simulations in combination
77 with the ROOT framework [2] for data analysis and visualization. Some of our
78 more demanding simulations are run on the MetaCentrum grid [3].

79 The X17 project in IEAP CTU aims to reproduce measurements of anomalous
80 behavior in the angular correlation distribution of pairs produced by the Internal
81 Pair Creation (IPC) mechanism [4] during the decay of certain excited nuclei
82 (${}^8\text{Be}$, ${}^{12}\text{C}$, and ${}^4\text{He}$) observed by a team at ATOMKI in Hungary. I would leave
83 this here as a short summary before I explain it in more detail in the sections
84 below.

85 Add citations: X17 project, VdG. Maybe also TPC, etc.

86 0.1 ATOMKI Anomaly

87 Many different theories propose the existence of *new light boson(s)* that are weakly
88 coupled to ordinary matter [5]. These particles are potential dark matter candi-
89 dates and could contribute to a solution of other issues with the Standard Model,
90 such as the strong CP problem¹ and the anomalous muon magnetic moment. Mass
91 range of axions?

92 A possible way of detecting such bosons with a short lifetime is to observe
93 nuclear transitions of excited nuclei. If a boson was emitted during the transition
94 and subsequently decayed into an electron-positron pair, we could observe this as
95 a peak on top of the standard e^+e^- (both cursive and upright forms are used in
96 different articles) angular correlation from the Internal Pair Creation (IPC) and
97 the External Pair Creation (EPC).

98 0.1.1 ATOMKI Measurements

99 Historically, there were several measurements of the IPC in nuclear transitions
100 in ${}^8\text{Be}$ at Institute für Kernphysik (Frankfurt) [6, 7, 8] and at ATOMKI (Debre-
101 cen, Hungary) [9, 10] resulting in different anomalies with invariant mass in the

1The CP symmetry could be violated in strong interactions according to the current formulation of quantum chromodynamics, but no such violation is observed.

range 5 – 15 MeV. This motivated the development of a better spectrometer at ATOMKI.

In 2015, a group at ATOMKI observed an anomalous IPC in ${}^8\text{Be}$ [11]. They used the ${}^7\text{Li}(p, \gamma){}^8\text{Be}$ reaction at the $E_p = 1030$ keV proton capture resonance to prepare the 18.15 MeV excited state ($J^\pi = 1^+, T = 0$). This state decays predominantly through M1 transitions to the ground state ($J^\pi = 0^+, T = 0$) and to the 3.03 MeV state ($J^\pi = 2^+, T = 0$) [12]. [Transition figure – all transitions of isotopes? IPC figure?](#)

The angular correlation of the e^+e^- pairs created internally in these transitions were measured and compared to the simulation; results from a narrow $E_{\text{sum}} = 18$ MeV region are shown in Fig. 0.1a. The simulation includes boson decay pairs for different boson masses. The disparity parameter y is used to describe the asymmetry of energy between the two particles. It is defined as

$$y = \frac{E_{e^-} - E_{e^+}}{E_{e^-} + E_{e^+}}, \quad (0.1)$$

where E_{e^-} and E_{e^+} are the kinetic energies of the electron and positron.

Their experimental setup was later upgraded ([details?](#)) and used for new measurements. In 2022 the ${}^8\text{Be}$ anomaly was also measured using the $E_p = 441$ keV resonance to produce the 17.64 MeV excited state ($J^\pi = 1^+, T = 1$) which again decays primarily to the ground state and the 3.03 MeV state [12]. The anomaly was also verified for $E_p = 650$ and 800 keV where E1 transitions from the direct proton capture dominate [13]. The results for e^+e^- with $E_{\text{sum}} \in [13.5, 20]$ MeV are shown in Fig. 0.1b.

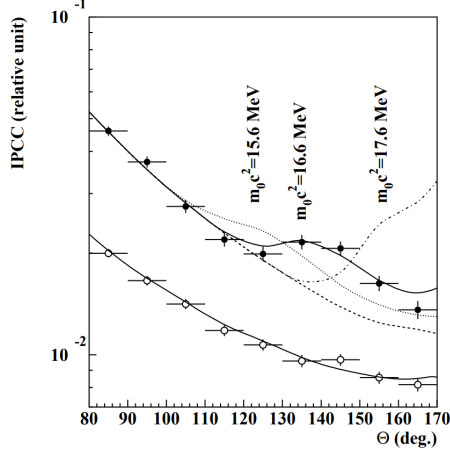
The newer setup was also used in 2021 to study the ${}^3\text{H}(p, e^+e^-){}^4\text{He}$ reaction at $E_p = 510, 610$ and 900 keV [14], inducing direct and resonant capture populating the overlapping first 20.21 MeV ($J^\pi = 0^+$) and second 21.01 MeV ($J^\pi = 0^-$) excited states [15]. The comparison of simulated and measured e^+e^- pair angular correlations in the $E_{\text{sum}} \in [18, 22]$ MeV region is shown in Fig. 0.1c.

In 2022, another anomaly was measured in the ${}^{11}\text{B}(p, e^+e^-){}^{12}\text{C}$ process [16]. The $E_p = 1388$ keV resonance was used to populate the 17.23 MeV excited state ($J^\pi = 1^-, T = 1$) with a large width $\Gamma = 1.15$ MeV [17]. This state decays mainly through E1 transitions to the ground state $J^\pi = 0^+$ and to the 4.44 MeV state $J^\pi = 2^+$. To compensate for energy losses in the target, five energies in the range $E_p = 1.5\text{--}2.5$ MeV were used. The experimental angular correlation for the 17.23 MeV transition to the ground state is shown in Fig. 0.1d.

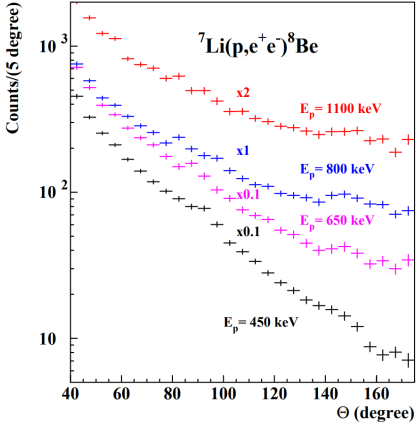
Possible explanations of the anomaly include experimental effects, higher order processes in the Standard Model [18, 19] or even a protophobic fifth force mediated by a new 17 MeV boson X17 [20]. [Not sure if the introduction should be referenced since even though it is related, it is an independent theory developed only \(?\) to explain these measurements. Zhang and Miller: <https://www.sciencedirect.com/science/article/pii/S0370269321000010> Paper from IEAP CTU: <https://arxiv.org/pdf/2309.12469.pdf>](#)

0.1.2 Other Experiments

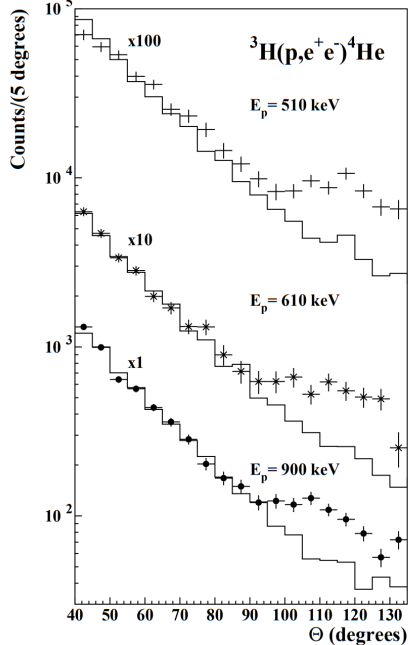
Since the ATOMKI measurements, several experiments have been initiated to attempt to replicate the results and search for the hypothetical X17 particle. The



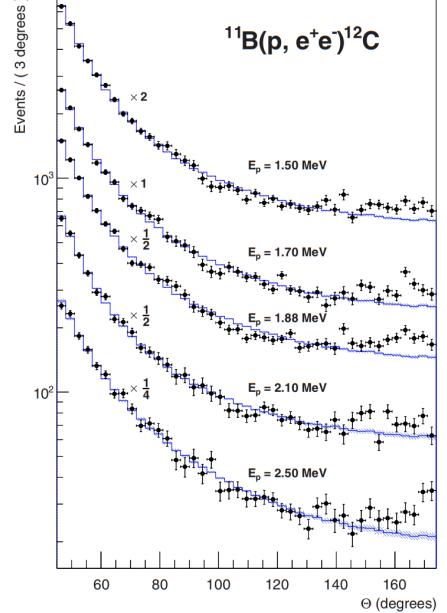
(a) Experimental e^+e^- pair correlations measured in the ${}^7\text{Li}(p, e^+e^-){}^8\text{Be}$ reaction with $|y| \leq 0.5$ (closed circles) and $|y| \geq 0.5$ (open circles) [11].



(b) Experimental e^+e^- pair correlations measured in the ${}^7\text{Li}(p, e^+e^-){}^8\text{Be}$ reaction with the improved setup for different proton beam energies [13].



(c) Experimental e^+e^- pair correlations measured in the ${}^3\text{H}(p, e^+e^-){}^4\text{He}$ reaction with $|y| \leq 0.3$ for different proton beam energies [14].



(d) Experimental e^+e^- pair correlations measured in the ${}^{11}\text{B}(p, e^+e^-){}^{12}\text{C}$ reaction for different proton beam energies [16].

Figure 0.1: The ATOMKI anomalous IPC measured for different nuclei.



Figure 0.2: Results from the Hanoi spectrometer – angular e^+e^- pair correlations measured in the ${}^7\text{Li}(p, e^+e^-){}^8\text{Be}$ reaction at $E_p = 1225$ keV [21].

following experiments have already produced results. Could cite the ATOMKI review paper here. NA64 at SPS: <https://arxiv.org/pdf/1803.07748>.

Two-arm e^+e^- spectrometer in Hanoi

The anomaly in ${}^8\text{Be}$ has been observed with a high ($> 4\sigma$ That's all they write in their article.) confidence by a team at the Hanoi University of Sciences for $E_p = 1225$ keV [21]. They built a two-arm spectrometer in collaboration with ATOMKI and calibrated it using the 17.6 MeV M1 transition. The results are shown in Fig. 0.2.

Collisions at Nuclotron in Dubna

At the Joint Institute for Nuclear Research in Dubna, signal in the form of enhanced structures in the $\gamma\gamma$ spectra at ~ 17 and ~ 38 MeV invariant masses for $p + \text{C}$, $d + \text{C}$ and $d + \text{Cu}$ reactions at momenta 5.5, 2.75, and 3.83 GeV per nucleon [22]. Monte Carlo simulations support the conclusion that the signals are a consequence of a decay of unknown particles X17 and E38.

The MEG II (Muon Electron Gamma) experiment

Experiments using the ${}^7\text{Li}(p, e^+e^-){}^8\text{Be}$ reaction were carried out at the Paul Scherrer Institute with the MEG II superconducting solenoid spectrometer [23]. Analysis of the data with $E_p = 1080$ keV exciting both of the resonances (beam fully stopping in the target) found no significant evidence supporting the X17 hypothesis, results are shown in Fig. 0.3. An upper bound (at 90% confidence) on the X17-to- γ branching ratio was set at $1.2 \cdot 10^{-5}$ for the 18.15 MeV state (larger than the ratio $5.8 \cdot 10^{-6}$ obtained by ATOMKI in 2016). Could add their 90% C.L bounds figure also. Insufficient statistics – 6.2 % (1.5σ) p-value.

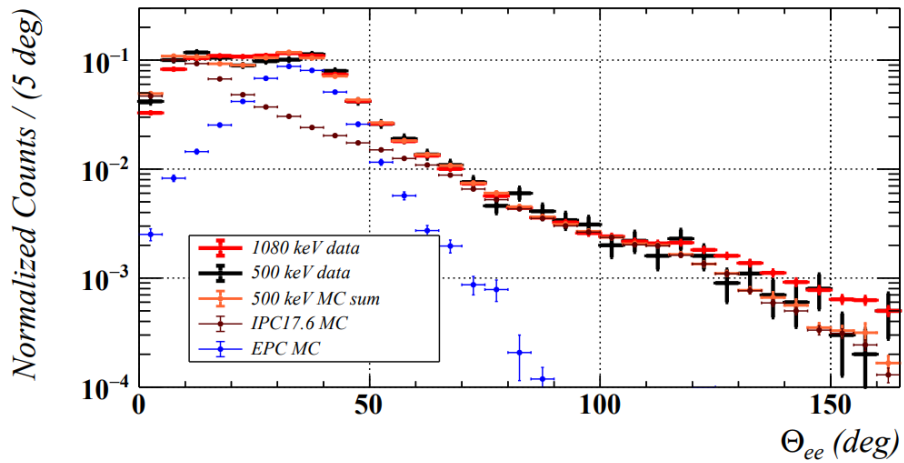


Figure 0.3: Results from the MEG II experiments – angular correlation of e^+e^- pairs with $E_{\text{sum}} \in [16, 20]$ MeV measured in the ${}^7\text{Li}(p, e^+e^-){}^8\text{Be}$ reaction with proton beam energies 500 and 1080 keV. The 500 keV dataset is fitted with Monte Carlo of both the IPC deexcitation and the EPC produced by gammas [23].

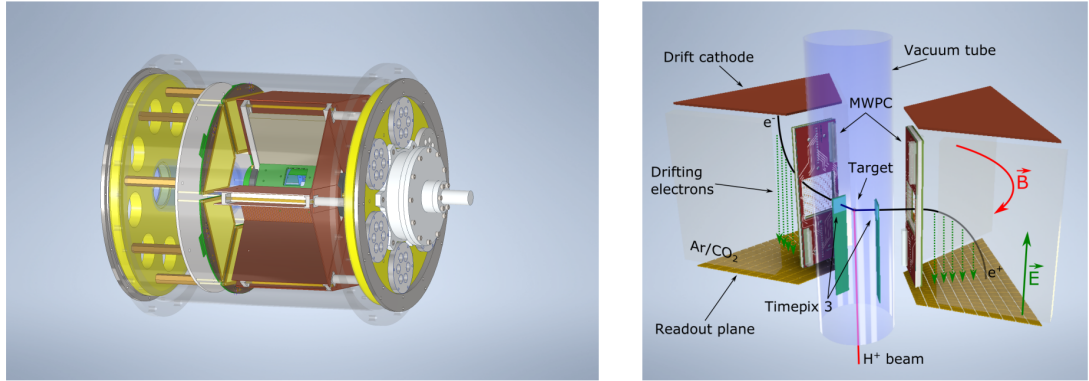


Figure 0.4: Schematics of the detector at the Van der Graaff facility at IEAP CTU (ref.).

168 0.2 X17 Project at IEAP CTU

169 The aim of the X17 project at the Van der Graaff facility of the Institute of
 170 Experimental and Applied Physics, Czech Technical University in Prague is to
 171 reproduce the results of the original ATOMKI experiments with ${}^7\text{Li}$ and ${}^3\text{H}$ tar-
 172 gets using an independent e^+e^- spectrometer. In order to effectively measure the
 173 anomaly, we need to reconstruct both the energy and the angular correlation of
 174 the e^+e^- pairs. The spectrometer will use three layers of detectors to achieve this
 175 – Timepix3 (TPX3) silicon pixel detector and Multi-Wire Proportional Cham-
 176 ber (MWPC) layers for the angle reconstruction and a Time Projection Cham-
 177 ber (TPC) layer for the energy reconstruction. The schematics of the prepared
 178 detector is in Fig. 0.4 Spectrometer CAD drawing (coordinates here or next chap-
 179 ter?). Cite some VdG paper, mention grant? Using https://cernbox.cern.ch/pdf-viewer/public/rf0oU1nqVLN3acZ/LuzH_submitted.pdf.

181 The energy of e^+e^- pair produced in the reaction is given by the energy

available E_r in the reaction and can be distributed between them arbitrarily. Nonetheless in the decay of the hypothetical X17 particle, electron and positron should have similar energy and we can therefore use a cut $|y| \leq 0.5$ in the disparity parameter (defined in Equation 0.1 **it was already used in ATOMKI figure captions, that's why it is defined prior to this**). Interesting events should rarely have a particle with an energy below $E_r/4$ (roughly 4 MeV). Electrons with such low energies are scattered significantly by even a thin layer of relatively light material, for this reason the TPX3 layer will be inside of the vacuum tube and the tube will have a thinned aluminum segment or KaptonTM windows.

TPX3 can measure (in each $55 \times 55 \mu\text{m}$ pixel of its 256×256 grid) time-of-arrival (ToA) with 1.6 ns precision and time-over-threshold (ToT) which reflects the deposited energy. This potentially allows 3D tracking if we increase the chip thickness at the cost of increased scattering. The layer can reconstruct the reaction vertex and the angular correlation with high precision.

The layer of MWPCs with sensitive area $40 \times 38 \text{ mm}^2$ will be outside of the beam pipe. It will provide an extra point on the particle trajectory which can help with the estimation of the reaction vertex and improve the TPC performance by providing its entry point.

The TPCs that are the subject of this thesis, are in a magnetic field generated by permanent magnets positioned between them and provide 3D track reconstruction and subsequent momentum and particle identification (its charge, or even type based on its stopping power). They avoid radiative losses thanks to the low density and atomic number of the gas mixture. For the readout, triple Gas Electron Multiplier (GEM) will be used. The magnetic field layout in our TPCs is atypical – orthogonal to the electric field inside the chamber, this is why we call them Orthogonal Fields TPC (OFTPC). Further details about our OFTPCs are provided in section 1.4.

1. Time Projection Chamber

A Time Projection Chamber (TPC) is a gaseous detector that uses the drift times of ionization electrons produced by a charged particle in an (ideally uniform) electric field to reconstruct the particle's 3D trajectory. The 2D projection is measured by an amplification stage at the end of the drift volume. When placed inside a magnetic field (typically parallel to the electric field), the momentum of the incident particle can be inferred from the curvature of its trajectory. Particle identification is also possible using the ionization energy loss inside the TPC (see Fig. 1.1). The following text (including Secs. 1.1 and 1.3) is based primarily on the reviews by Hilke [24] and the Particle Data Group [25].

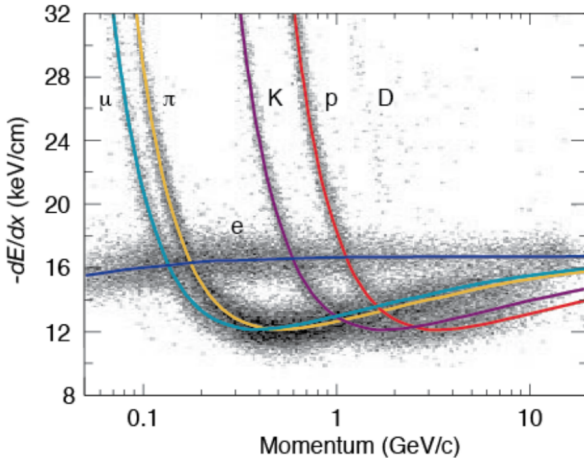


Figure 1.1: Particle identification in the PEP-4 TPC at SLAC based on the energy loss per distance $\frac{dE}{dx}$ in the 80:20 Ar:CH₄ filling at 8.5 atm pressure [26]. The reference doesn't point to the original PEP-4 article because this adapted version of the original picture that they used in the DUNE article looks better.

Large TPCs are sensitive to small distortions in the electric field (imperfections in the field cage, accumulation of positive ions in the gas volume) and to $\mathbf{E} \times \mathbf{B}$ effects on the drift velocity (see Eq. 1.1 below). Diffusion of the drifting electrons deteriorates the spacial resolution significantly, but it can be reduced up to ~ 10 times by a strong $\mathbf{B} \parallel \mathbf{E}$ field (see Eq. 1.8).

In neutrino and other rare-event experiments, large (up to 600 tons) Liquid Argon TPCs (LArTPCs) are used for particle identification and calorimetry. The ionization electrons can be drifted for many meters with a small diffusion. Scintillation photons are also measured. Negative ions?

1.1 Charge transport in gases

When a charged particle crosses the volume of a TPC, it loses energy by excitation and ionization of the detector gas (how much – from $dE/dx +$ density → footnote?). Most ionizing collision produce a single ionization electron, sometimes a few secondary electrons are produced near the collision vertex, creating a cluster. In rare cases, the ionization electron has energy large enough to create

234 a measurable track, such an electron is called a δ -electron (terminology, just like
235 bellow – technically it's a (primary) ionization electron causing other (secondary)
236 ionization).

237 After their release, the ionization electrons are separated from positive ions
238 by the electric field and they both drift and diffuse in opposite directions towards
239 the electrodes. The charges are accelerated (different word?) by the electric field
240 inside the chamber, and they lose speed by colliding with the gas particles, quickly
241 reaching a constant (for a given field \mathbf{E}, \mathbf{B}) mean drift velocity. The electrons can
242 be absorbed by electronegative impurities, such as halides, O_2 , and H_2O .

243 In mixtures with a noble gas component, if the excitation energy of the noble
244 gas is higher than the ionization potential of an admixture, more free electrons can
245 be produced through collisions of the gas particles (so-called Penning transfer)
246 and through absorption of emitted photons.

247 If the electric field is strong enough, the electrons can cause further ion-
248 ization and excitation of the gas, leading to the development of a Townsend
249 avalanche (ref).

250 1.1.1 Drift

251 In many gases (called "hot", e.g., Ar or CH_4), the drift velocity is much greater
252 than that of their thermal motion thanks to a high proportion of elastic collisions.
253 On the other hand, "cold" gases like CO_2 have a higher proportion of inelastic
254 collisions (e.g., thanks to the excitation of rotational and vibrational states) and
255 therefore much lower (value? magnitude (implied?)) drift velocity. Or maybe it
256 is not so simple, because slowing down the electrons inelastically into a certain
257 minimum of elastic scattering cross-section increases drift velocity? In case of
258 $\text{Ar}+\text{CO}_2$ this is clearly not the case for low electric fields, so maybe irrelevant
259 here (or is the effect opposite for small additions?).

260 The ions produced by the ionization lose a significant portion of their energy
261 during each collision since their mass is close to the mass of the gas particles (see
262 the source material – average energy loss during collision $\Delta E = \frac{2m_i M}{(m_i + M)^2}$, this
263 way it's more accurate). This, together with their large collision cross section,
264 makes their drift velocity much smaller (about three orders of magnitude) and
265 their energy is close to thermal. Since their momenta are not randomized to such
266 an extent during collisions, their diffusion is smaller (move this to the diffusion
267 subsection, reformulate).

268 The drift is also influenced by the magnetic field. Langevin derived a good
269 approximation for the drift velocity vector:

$$\mathbf{v}_d = \left(\frac{\mathbf{E}}{\|\mathbf{E}\|} + \omega\tau \frac{\mathbf{E} \times \mathbf{B}}{\|\mathbf{E}\| \|\mathbf{B}\|} + \omega^2\tau^2 \frac{\mathbf{E} \cdot \mathbf{B}}{\|\mathbf{E}\| \|\mathbf{B}\|} \cdot \frac{\mathbf{B}}{\|\mathbf{B}\|} \right) \frac{q\tau}{m(1 + \omega^2\tau^2)} \|\mathbf{E}\|, \quad (1.1)$$

270 where q is the charge of the particle, m is its mass, τ is the mean time between
271 collisions and $\omega = \frac{q}{m} \|\mathbf{B}\|$ is the Larmor frequency. For orthogonal fields $\mathbf{E} \perp \mathbf{B}$,
272 it can be shown that the magnetic field bends the direction of the drift by the
273 so-called Lorentz angle:

$$\tan \psi = -\omega\tau. \quad (1.2)$$

274 The drift of ions is only negligibly influenced by the magnetic field ($\omega\tau \sim 10^{-4}$
275 is small due to the low drift velocity – better (?) because it takes τ into account

²⁷⁶ and differs only by E/B ratio (if the magnetic contribution to the magnitude is
²⁷⁷ small)). In a standard TPC, \mathbf{E} is parallel to \mathbf{B} and the influence of the magnetic
²⁷⁸ field on the drift is minimal. Without magnetic field, we can write

$$\mathbf{v}_d = \frac{q\tau}{m} \mathbf{E} = \mu \mathbf{E}, \quad (1.3)$$

²⁷⁹ where μ is called charge mobility.

²⁸⁰ 1.1.2 Diffusion

²⁸¹ All of the theory is from the same source mentioned at the beginning. None of the
²⁸² simulations explicitly depend on this. Due to collisions, a cloud of electrons or
²⁸³ ions originating from the same point will show a Gaussian density distribution at
²⁸⁴ time t while drifting in the electric field $\mathbf{E} = (0, 0, E_z)$ along the z -coordinate (²⁸⁵ coordinates defined by the electric field):

$$\rho(x, y, z, t) = (4\pi Dt)^{-\frac{3}{2}} \exp\left(-\frac{x^2 + y^2 + (z - v_d t)^2}{4Dt}\right), \quad (1.4)$$

²⁸⁶ where the diffusion coefficient D can be expressed as

$$D = \frac{\lambda^2}{3\tau} = \frac{\lambda v_d}{3} = \frac{v_d^2 \tau}{3} = \frac{2\varepsilon\tau}{3m}, \quad (1.5)$$

²⁸⁷ where λ is the mean free path and ε the mean kinetic energy. The lateral diffusion
²⁸⁸ width σ_x after a drift distance L can be expressed as

$$\sigma_x^2 = 2Dt = \frac{4\varepsilon L}{3qE_z}. \quad (1.6)$$

²⁸⁹ The minimal diffusion width is given by the lowest possible energy of the particles
²⁹⁰ $\varepsilon_{\text{th}} = \frac{3}{2}kT$ (corresponding to thermal motion):

$$\sigma_{x, \text{min}}^2 = \frac{2kTL}{qE}. \quad (1.7)$$

²⁹¹ For electrons in "cold gases" (e.g., Ar/CO₂ mixture), the diffusion approaches this
²⁹² limit up to a certain field intensity (~100 V/cm at 1 atm pressure)¹. In reality, the
²⁹³ transversal diffusion of electrons can differ significantly from their longitudinal
²⁹⁴ diffusion and simulations are necessary to get a precise result.

²⁹⁵ In most TPCs, the transversal (but not the longitudinal) diffusion is reduced
²⁹⁶ by the magnetic field, since it is parallel to the electric field and curves the
²⁹⁷ diffusing electrons around their mean trajectory:

$$\frac{D_T(B)}{D_T(0)} = \frac{1}{C + \omega^2 \tau_2^2}, \quad (1.8)$$

²⁹⁸ where C and τ_2 are parameters dependent on the gas used. At low intensity of
²⁹⁹ the magnetic field, we can use an approximation $C \approx 1$ and $\tau_2 \approx \tau$.

¹For us $\sigma_{x, \text{min}} = 0.45$ mm, quite close to the actual diffusion 0.5-0.7 mm – details of the calculation.

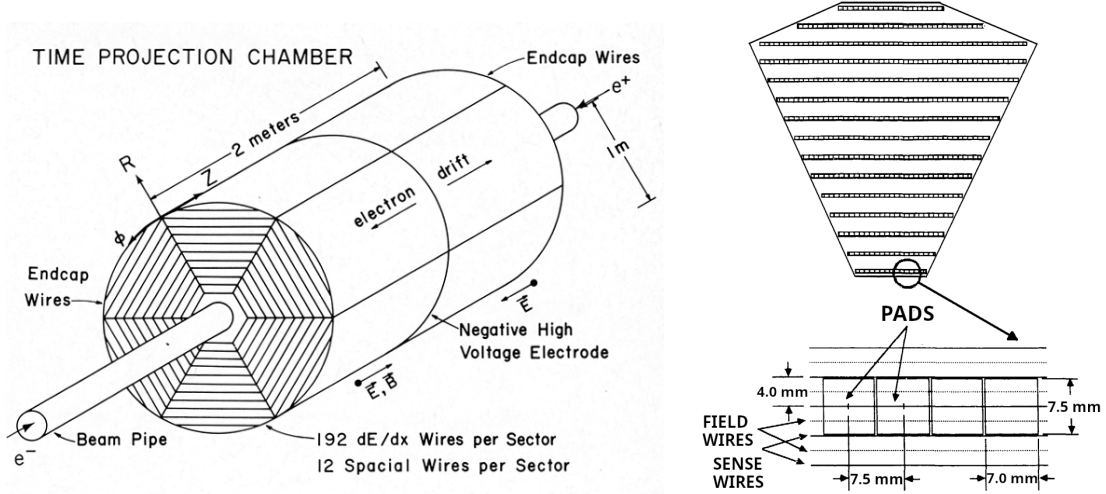


Figure 1.2: Schematic view of the PEP-4 TPC [28]. A charged particle produced in a collision in the beam pipe creates a spiral ionization track in the magnetic field. The central cathode then accelerates ionization electrons towards the endcap anode wires where they are multiplied and read out. A TPC sector with a detailed view of one of the pad rows is shown on the right [29].

300 1.2 Examples of TPCs

301 1.2.1 The original TPC at PEP-4 at SLAC

302 The original TPC used in the PEP-4 experiment at SLAC in the 1980s (Fig. 1.2)
 303 was a $2\text{ m} \times 2\text{ m}$ hollow cylinder with a central cathode that produced a strong
 304 electric field 750 V/cm , making the ionization electrons drift towards one of the
 305 endcaps [27]. It was filled with a 80:20 Ar:CH₄ mixture at 8.5 atm pressure
 306 and placed inside a 0.4 T solenoidal magnetic field. The readout consisted of
 307 MWPCs, where electrons are accelerated towards the anode wires fast enough to
 308 further ionize the gas and cause an avalanche (details are provided in Sec. 1.3.1).
 309 The wires had radial spacing 4 mm, fifteen of the sense wires had the cathode
 310 segmented into $7.0 \times 7.5\text{ mm}^2$ pads 4 mm under them (Fig. 1.2 right). When
 311 collecting electrons on the anode wire, signal is induced on the nearest 2-3 cathode
 312 pads.

313 1.2.2 ALICE TPC

314 The ALICE TPC (Fig. 1.3) is the main detector used for charged particle tracking
 315 and recognition in collisions at the ALICE experiment at the CERN LHC [30].
 316 Similarly to PEP-4, it is a hollow cylinder with outer radius 2.5 m and height 5 m.
 317 It is placed in a 0.5 T solenoidal magnetic field, and the central cathode generates
 318 a 400 V/cm electric field inside the field cage. The gas mixture in the detector
 319 is 90:10:5 Ne:CO₂:N₂, mainly chosen for its higher ion mobility compared to Ar
 320 mixtures. In 2020, the readout of the TPC was upgraded from MWPCs to stacks
 321 of four GEM foils (principle described in Sec. 1.3.2). This allows reading events
 322 continuously at a higher rate.

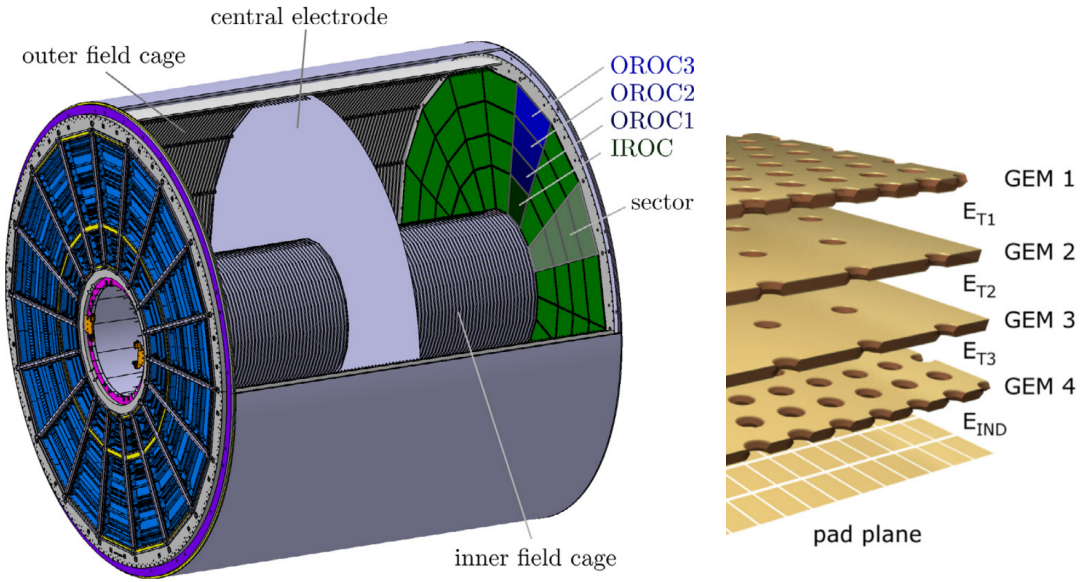


Figure 1.3: Schematic view of the ALICE TPC [31]. The readout at each endcap is divided into 18 sectors, each subdivided into an Inner Readout Chamber (IROC) with one GEM stack and Outer Readout Chamber (OROC) with three GEM stacks. A visualization of a GEM stack is on the right [32].

323 1.2.3 CERES/NA45 radial-drift TPC

324 In 1998, the CERES/NA45 (Cherenkov Ring Electron Spectrometer) experiment
 325 (Fig. 1.4) at the CERN SPS was upgraded with the first radial-drift TPC (rTPC)
 326 to achieve a higher momentum resolution [33]. Unlike a standard TPC, the elec-
 327 tric field 600–200 V/cm was arranged radially with the magnetic field (inhomoge-
 328 neous, up to 0.5 T) by two solenoidal coils with opposite polarity. The outward
 329 drift of the ionization electrons is affected by the crossing fields as shown in Eq. 1.1
 330 and the drift velocity is not uniform due to the varying electric field. The rTPC
 331 was filled with an 80:20 Ne:CO₂ gas mixture, which has relatively small diffu-
 332 sion coefficients and Lorentz angle. The readout was handled by conventional
 333 MWPCs (Fig. 1.5).

334 The field configuration in an rTPC enables a larger number of pads compared
 335 to a standard TPC, leading to improved spatial resolution and possibility of larger
 336 multiplicity rates. Since the drift time is lower, the detector is faster.

337 After an algorithm described in this thesis was developed for our OFTPCs at
 338 IEAP CTU, we noticed the similarities with the approach used by the CERES/NA45||
 339 rTPC, when accounting for the transport process of charged clusters in the com-
 340 plex fields. The detector hit coordinates (pad, time, and plane) were transformed
 341 using look-up tables. The tables were calculated using a Runge-Kutta method to
 342 integrate the Langevin approximation of the drift velocity (Eq. 1.1). The drift
 343 velocity in the radial field was calibrated using seven parallel laser rays. This
 344 calibration was then used to make a correction compared to the MAGBOLTZ
 345 Monte Carlo drift [34]. **Measured mobility differs significantly from MAGBOLTZ,**
 346 **but this might be improved in the newer versions?** The tracks were fitted using
 347 reference tables with hit coordinates of tracks simulated with GEANT Monte
 348 Carlo (**not such a big problem for us right now, might be an idea if the recon-**

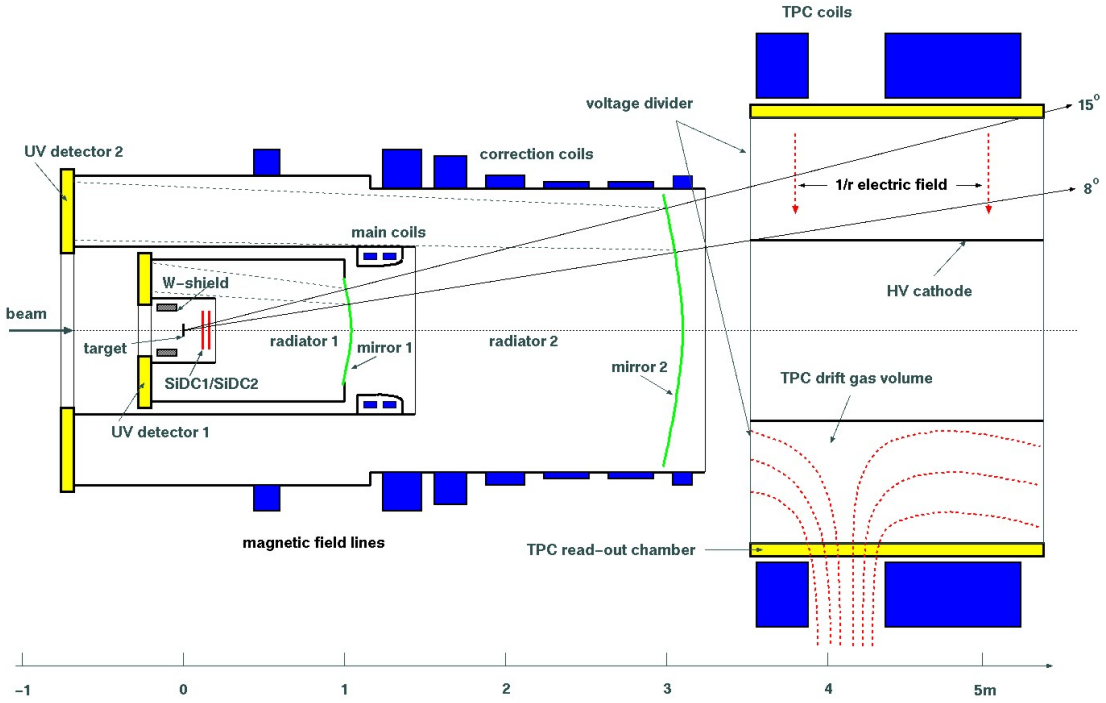


Figure 1.4: Experimental setup of the CERES/NA45 experiment with two Ring Imaging Cherenkov Counters (RICHs) on the left and a rTPC on the right. The magnetic field (red) is generated by two solenoidal coils (blue) with opposite polarity. Produced ionization electrons drift outward radially towards the readout chamber (yellow) [33].

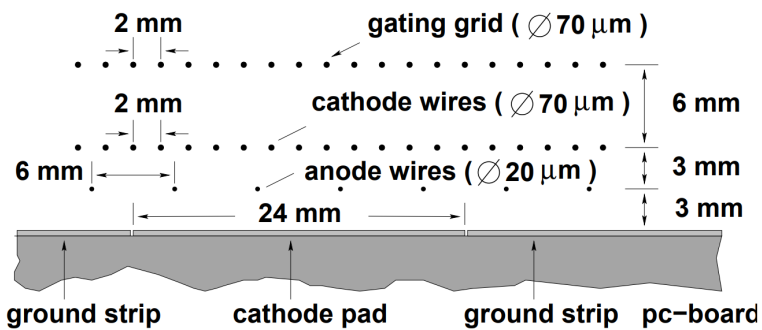


Figure 1.5: Cross section of a CERES/NA45 readout MWPC. The wires are stretched in the azimuthal direction above the pad plane. The gating grid controls the passage of electrons and ions. [33].

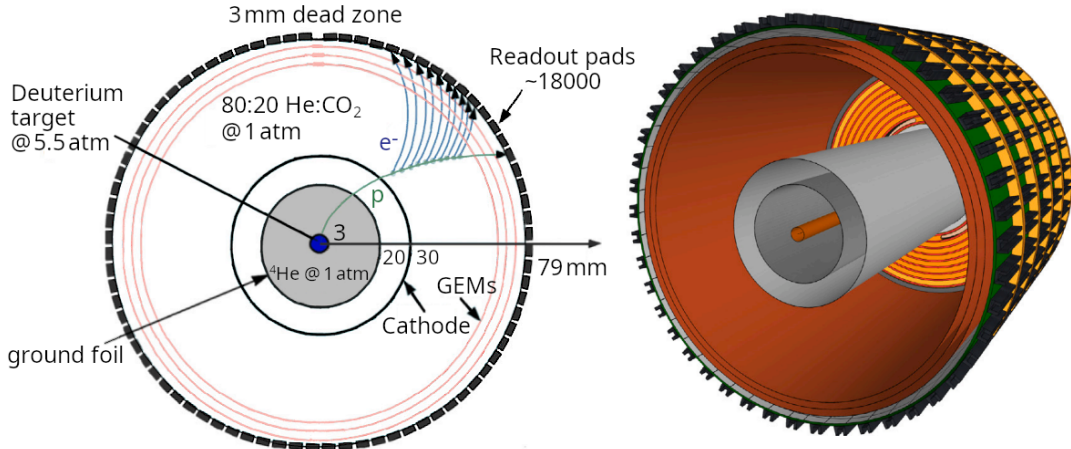


Figure 1.6: Schematic view of the BONuS12 rTPC [35].

349 construction gets too slow).

350 1.2.4 Other interesting radial-drift TPCs

351 muEDM at PSI: [https://arxiv.org/pdf/2307.01535](https://arxiv.org/pdf/2307.01535.pdf),

352 FTPC at STAR at RHIC: [https://arxiv.org/pdf/nucl-ex/0211014](https://arxiv.org/pdf/nucl-ex/0211014.pdf)

353 BONuS12 rTPC

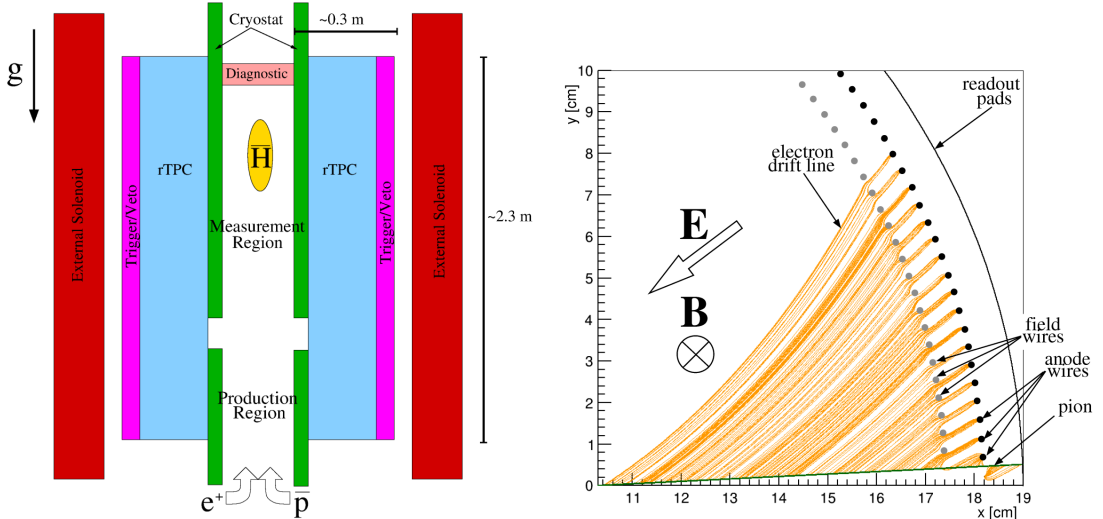
354 In 2020, the Barely Off-shell Neutron Structure 12 GeV (BONuS12) experiment
 355 used an rTPC (Fig. 1.6) to measure low-momentum spectator protons produced
 356 in $e^-d \rightarrow e^-p_sX$ scattering [35]. It was filled with a 80:20 He:CO₂ gas mixture and
 357 placed inside a 4 T solenoidal magnetic field, perpendicular to the radial electric
 358 field (1100 V/cm on average), tilting the drift (see Eq. 1.2). The amplification
 359 used cylindrical triple GEM stacks.

360 Garfield++ simulations and study of reconstructed tracks have shown that the
 361 radial component of the drift velocity almost proportional to the radial electric
 362 field, and the r -coordinate can be reconstructed using an analytical formula. Sim-
 363 ilarly, the azimuthal component is nearly proportional to the radial component,
 364 resulting in a largely constant Lorentz angle between the radial and actual direc-
 365 tion, and the ϕ -coordinate can be solved analytically. The remaining z -coordinate
 366 stays undistorted. The momentum is determined by fitting tracks with a helix,
 367 while accounting for the energy losses (the small variability of magnetic field along
 368 the z -axis has a negligible effect).

369 ALPHA-g rTPC

370 In 2023, the Antihydrogen Laser Physics Apparatus (ALPHA) collaboration pub-
 371 lished results of measurements of antihydrogen (\bar{H}) annihilation² after release
 372 from magnetic confinement, showing that it behaves in a way consistent with grav-
 373 itational attraction to the Earth [36]. They used a 2.3 m long rTPC (Fig. 1.7a)

²The main \bar{p} annihilation mode is into several π^\pm and π^0 , only the π^\pm tracks are long enough to be reconstructed. The scattering of π^\pm is not negligible, and photons from π^0 decay create e^+e^- pairs as background.



(a) Sketch of ALPHA-g. Antiprotons and positrons are injected from the bottom and form \bar{H} in a Penning trap while being cooled by the cryostat (green). The annihilation is reconstructed by the rTPC (blue).

(b) Cross section view of the rTPC (Garfield++ simulation). The electrons (orange) produced by a pion track (green) drift towards the anode wires, while influenced by the axial magnetic field. The size of the field and anode wires is exaggerated.

Figure 1.7: Schematic view of the ALPHA-g detector [37].

with a 40 cm outer and 20 cm inner diameter in a 1 T solenoidal magnetic field, and filled with an Ar/CO₂ mixture [37]. The readout consists of an MWPC (Fig. 1.7b). The radial confinement of the cold \bar{H} is achieved with a superconducting octupole magnet, the axial with a set of so-called *mirror* coils.

The r -coordinate of the ionization cluster is reconstructed from the drift time using a tabulated space-time relation. The 3D position of the interaction (cluster) vertex is obtained by matching the wires and pads by drift time using a k-d tree algorithm. Reconstructed tracks are fitted with a helix using the least squares method [38].

1.3 Readout

1.3.1 Multi-Wire Proportional Chamber

In most TPCs operated in experiments, Multi-Wire Proportional Chamber (MWPC) was used for the readout (Fig. 1.8). The electrons enter the chamber through a cathode grid and get accelerated by a strong electric field towards the parallel, thin anode wires and create an avalanche, multiplying the signal. The trajectory can be reconstructed from the drift time and two coordinates measured using

- a) two segmented cathodes (wires or strips) rotated by 90° or
- b) the ratio of charge collected on two sides of the hit resistive wires.

For high counting rates, the positive ions from the avalanches accumulate, creating a space charge that distorts the electric field. This can be solved by using a gating grid near the readout plane to collect these ions at the cost of introducing a dead time in the detector.

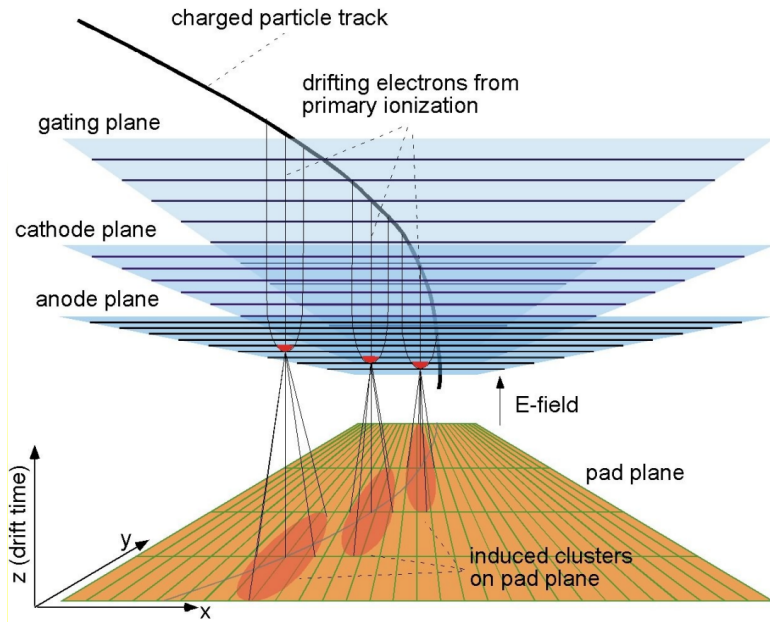


Figure 1.8: Schematic view of the ALICE MWPC readout (working principle) [39].

396 1.3.2 Micro-Pattern Gaseous Detectors

397 In order to avoid MWPC limitations (e.g., diffusion, wire $\mathbf{E} \times \mathbf{B}$ effect, space
 398 charge effects), a family of Micro-Pattern Gaseous Detector (MPGD) technologies
 399 are being developed. The readouts can reach higher spatial resolution (down to
 400 $30\text{ }\mu\text{m}$) with faster response time (ns range) and much higher rate capability.

401 Gas Electron Multiplier

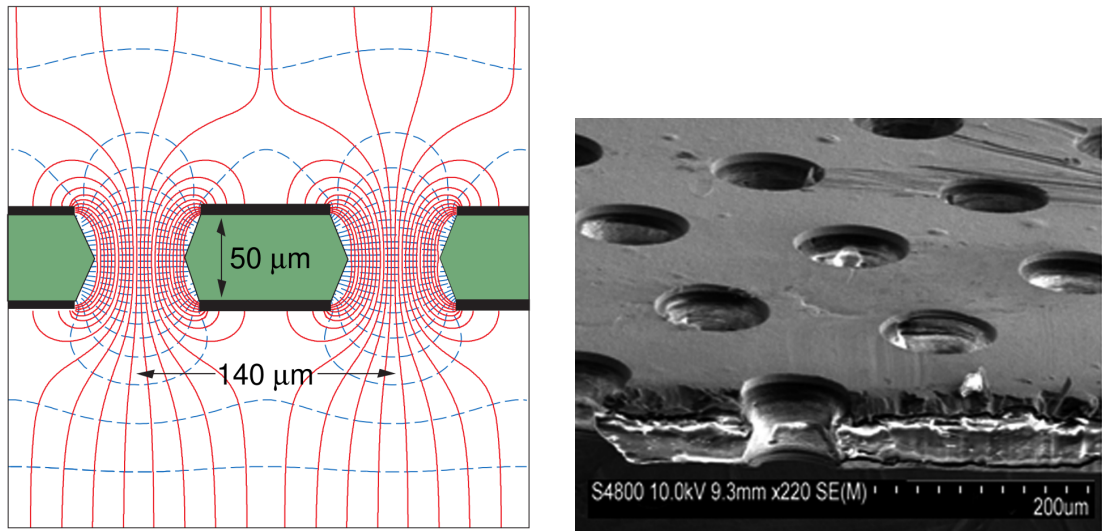
402 A Gas Electron Multiplier (GEM) is a thin metal-coated polyimide sheet with
 403 a dense pattern of small, chemically etched holes (Fig. 1.9). The amplification is
 404 achieved by applying voltage across the metal layers and placing the foil between
 405 two moderate uniform electric fields. This creates a strong electric field inside the
 406 holes that accelerates the incoming electrons and causes avalanches (see Fig. 1.10).
 407 Some charges may land on the dielectric surfaces due to diffusion, modifying the
 408 field and affecting gain.

409 Double or triple stacks of GEMs are usually used to create a sufficient gain
 410 while maintaining stability (reducing discharges). From the last foil, the electrons
 411 drift to a segmented anode where the signal is read. The ion backflow is reduced
 412 compared to MWPC.

413 A cheaper alternative (especially for large area coverage) is a THick GEM
 414 (THGEM) with a ~ 10 -fold upscaling of geometrical parameters. It can be made
 415 by mechanically drilling holes into a standard Printed Circuit Board (PCB) and
 416 creating a circular rim around the holes by etching the metal coating.

417 Micromegas

418 In a MICRO-MEsh GAseous Structure (Micromegas) (in sources I viewed it is not
 419 capitalized) electrons pass through a fine mesh (made out of very thin wires) into



(a) A schematic view of a GEM cell with its typical dimensions, electric field lines (red), and equipotentials (blue) [25].

(b) A scanning electron microscope image of a GEM foil [40].

Figure 1.9: Gas Electron Multiplier (GEM).

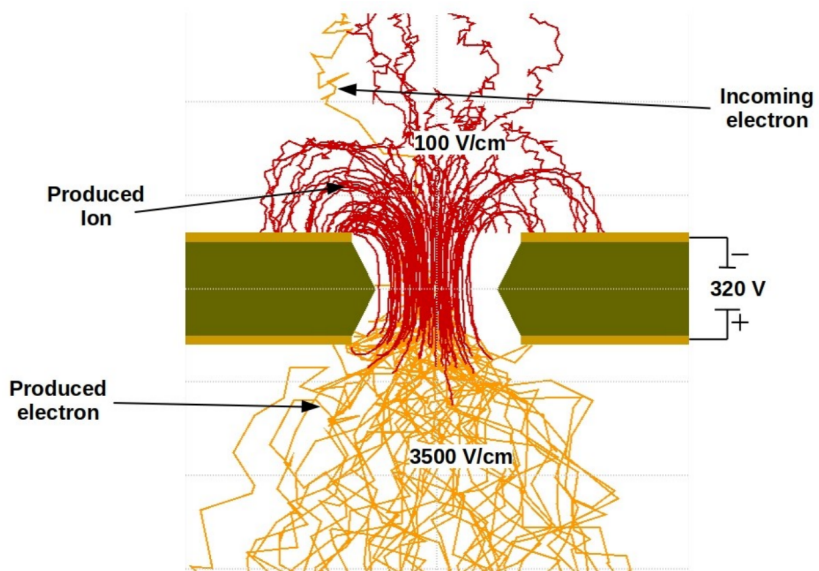
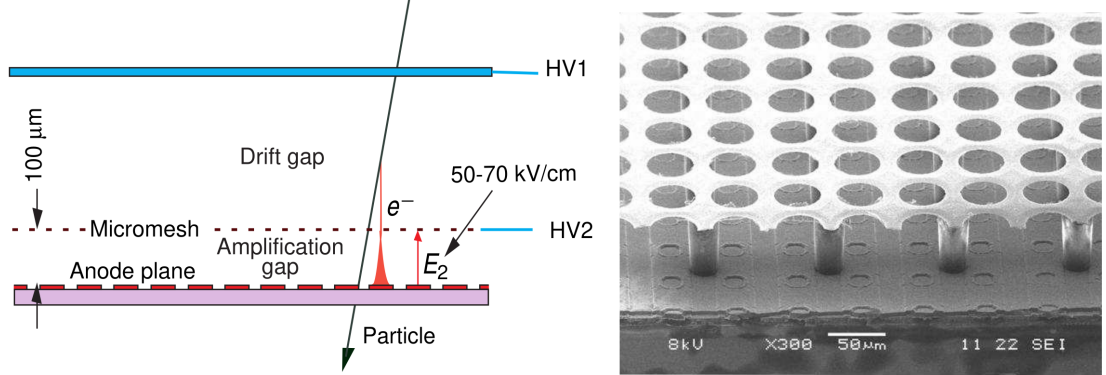


Figure 1.10: Garfield simulation of an avalanche in a GEM hole [41]. An incoming electron (orange) is accelerated in the strong electric field of the GEM and causes further ionization multiplying the number of free electrons (orange). Most of the produced cations (red) are captured by the GEM cathode.



(a) A schematic view of a Micromegas detector.

(b) A scanning electron microscope image of a Micromegas "GridPix" detector.

Figure 1.11: MICRO-MEsh Gaseous Structure (Micromegas) [25].

a narrow amplification gap where they are multiplied in the high field and read as a signal on the segmented anode (Fig. 1.11a). Very high field ($30-80 \text{ kV/cm}^2$) is necessary to achieve sufficient gain. Ion backflow is heavily suppressed by the mesh.

A Timepix chip (a high granularity pixel detector) can be used for the readout anode to achieve the best spatial resolution, making an integrated readout called GridPix (Fig. 1.11b). Thanks to the high spatial resolution, it is possible to distinguish individual electron clusters, which enables a new method of particle identification.

429 Other MPGDs

430 A Resistive Plate WELL (RPWELL) consists of a THGEM with only the top
 431 side metal-coated, mounted on a resistive film deposited on a thin isolating sheet
 432 (which is read out similarly to a Resistive Plate Chamber (RPC)). Due to the
 433 higher field in the closed holes of the THGEM, a higher gain can be reached for
 434 the same voltage. A Micro-RWELL (μ -RWELL) is a similar architecture with
 435 ~ 7 times smaller pitch (distance between holes). These options provide a better
 436 spark resistance and could allow to cover large areas for a lower cost.

437 A Micro-Pixel Gas Chamber (μ -PIC) is a PCB with anode strips on one side
 438 and orthogonal cathode strips on the other. The cathode has a resistive coating
 439 and a regular pattern of uncoated regions with anode "dots" penetrating the PCB
 440 at the centers.

441 1.4 Orthogonal Fields TPC at IEAP CTU

442 At IEAP CTU, we are going to use six identical atypical TPCs with inhomogeneous toroidal magnetic field **orthogonal** to the electric field (details below),
 443 hereafter referred to as Orthogonal Fields TPC (OFTPC). It has the shape of
 444 isosceles trapezoidal prism 16 centimeters high with triple-GEM readout on one
 445 of its bases. Dimensions of the OFTPC are discussed in detail in section 1.4.2
 446 below. Throughout this thesis, we assume a uniform electric field along the z axis
 447 with $E_z = -400 \text{ V/cm}$. Isn't the field affected by the MWPCs? Eventually a sim-

ulation will be needed. Measured particles enter the OFTPC through a window after crossing the MWPC. Gas mixture used in the detector (70/30) and its effect – some graph with the mixture, reasons for the choice. Add a figure of the real TPC. More about the design choices.

1.4.1 Motivation and Associated Challenges

The reasons for the unusual field layout are mostly cost related:

- a) we use permanent magnets instead of a solenoid and parallel fields are difficult to accomplish this way,
- b) granularity of the TPC readout is limited in order to fit one SAMPA/SRS hybrid in each sector – parallel fields would bend the trajectories parallel to the readout requiring more pads and different architecture.

In this thesis, we will show that such a setup can reach a similar energy resolution as common cylindrical TPCs while reducing the overall cost.

The layout introduces two complications to the track reconstruction – the trajectory in inhomogeneous field is not circular and the drift is distorted by the magnetic field as shown in the Equation 1.1(in our case $\omega\tau \approx 0.08$ for 0.3 T assuming $\mu \approx 0.25$ T⁻¹, varies inside the detector). We will deal with these effects in the upcoming chapters.

The diffusion in such setup is larger since parallel orientation reduces diffusion by curling the electrons in the x - y direction (see Equation 1.8), but for our relatively weak magnetic field and short drift distance, the difference is negligible.

1.4.2 Coordinate Systems and Dimensions

In order to describe events in our detector, we use three distinct spaces: the detector space \mathcal{D} , the readout space \mathcal{R} and the pad space \mathcal{P} (different spaces that describe different things and each has their own coordinate system, so maybe rename the section somehow?). Each space is later used to represent ionization electrons at different stages of the detection process: their creation in the gas, their final position when hitting the readout plane, and finally their representation in the discrete pad space.

Detector Space

The detector space \mathcal{D} represents the physical space of our detector. We describe it using Cartesian coordinates (x, y, z) . The z -axis is the detector's axis of symmetry, with its negative direction aligned with the proton beam. The origin $(0, 0, 0)$ is located at the center of the irradiated target. The positive x -axis passes through the center of one the OFTPCs along the intersection of its two planes of symmetry. The y -axis is then chosen to maintain a right-handed coordinate system.

Since the detector has a hexagonal symmetry, we use only one of its sectors in this work – the first sector $\mathcal{D}_1 \subset \mathcal{D}$ which is defined by the condition:

$$(x, y, z) \in \mathcal{D}_1 \Leftrightarrow |y| \leq x \tan \frac{\pi}{6}. \quad (1.9)$$

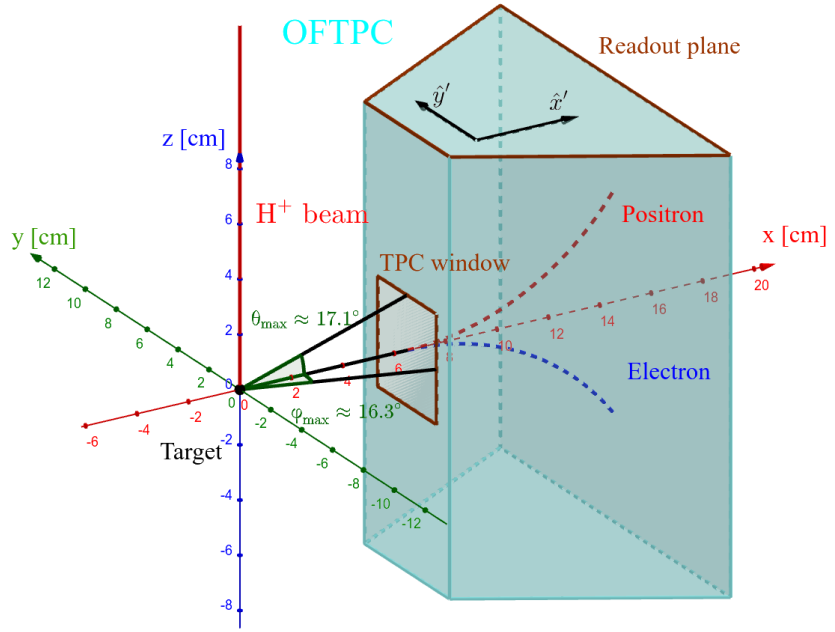


Figure 1.12: Schematics of the first sector OFTPC with detector space coordinates.

488 Simulations in this sector can be applied to all sectors by rotating the coordinates
 489 accordingly. The volume of the OFTPC in this sector, which has the shape of
 490 a trapezoidal prism, has these boundaries:

$$x \in [x_{\min}, x_{\max}] = [6.51, 14.61] \text{ cm}, \quad (1.10)$$

$$z \in [z_{\min}, z_{\max}] = [-8, 8] \text{ cm}, \quad (1.11)$$

$$y_{\max}(x_{\min}) = -y_{\min}(x_{\min}) = 2.75 \text{ cm}, \quad (1.12)$$

$$y_{\max}(x_{\max}) = -y_{\min}(x_{\max}) = 7.45 \text{ cm}, \quad (1.13)$$

491 where $y_{\max}(x)$ is the maximal value of the y -coordinate for a given x . The read-
 492 out is located at $z = 8$ cm; for some purposes, we also define the distance to
 493 the readout $d_r = 8 \text{ cm} - z$ as an alternative to the z -coordinate. **Keeping this**
 494 **paragraph as it is because the OFTPC volume is distinct from the first sector**
 495 **and some parts of this thesis use the space beyond this volume.** The OFTPC
 496 window has width 3.8 cm and height 4.0 cm.

497 We also use spherical coordinates (r, θ, φ) with the elevation angle θ measured
 498 relative to the xy plane. Angles θ and φ are useful when describing the direction
 499 of e^+/e^- tracks. Their maximal values considered for the initial direction in
 500 simulations are $\theta_{\max} \approx 17.1^\circ$ and $\varphi_{\max} \approx 16.3^\circ$ as shown in Fig. 1.12.

501 Readout Space

502 The readout space \mathcal{R} represents the drift time and final positions of ionization
 503 electrons as measured by an ideal continuous readout. We describe it using
 504 coordinates (x', y', t) , where x' and y' correspond to the detector coordinates at
 505 the readout plane ($z = 8$ cm).

506 Currently not entirely sure how to put this into a figure since only x' and
 507 y' correspond to the detector coordinates, it will make more sense when

508 **visualizing the map.** The drift time t is approximately proportional to d_r .

509 Pad Space

510 The pad space \mathcal{P} represents the time bin and pad number of ionization electrons
511 as measured by an ideal discrete readout:

$$\mathcal{P} = \{(n_{\text{pad}}, n_t) \in \mathbb{N}^2 \mid n_{\text{pad}} \leq 128\}. \quad (1.14)$$

512 **Rewrite to reflect this:** Technically both values can be zero as defined in the
513 code (max channel 127). It is not really a subspace of \mathcal{R} but there is a mapping
514 from \mathcal{R} to \mathcal{P} . It is a discretization of a part of \mathcal{R} , the mapping can be adjusted
515 depending on the simulation. If we assume uniform electric field there will be
516 gaps, we don't use gaps in the reconstruction since the electrons should be pulled
517 towards the pads.

518 The readout of the OFTPC will consist (is the design final?) of 128 rectangular
519 pads arranged in a staggered pattern. Parameters of the pad layout are shown
520 in Fig. 1.13. The bottom left corner of n -th pad has coordinates $(x_{1,n}, y_{1,n})$, the
521 top right $(x_{2,n}, y_{2,n})$ and its center has coordinates $(x_{c,n}, y_{c,n})$. The gap between
522 neighboring pads is $g = 0.08$ cm. Time will be read out in discrete bins of size
523 $t_{\text{bin}} = 100$ ns (details?). Could also describe pad-related functions.

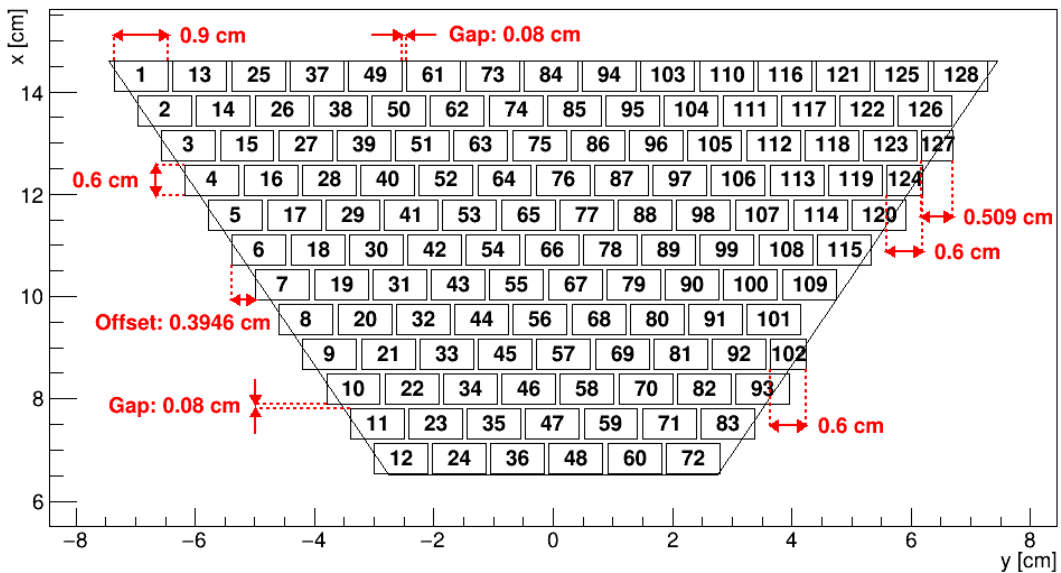
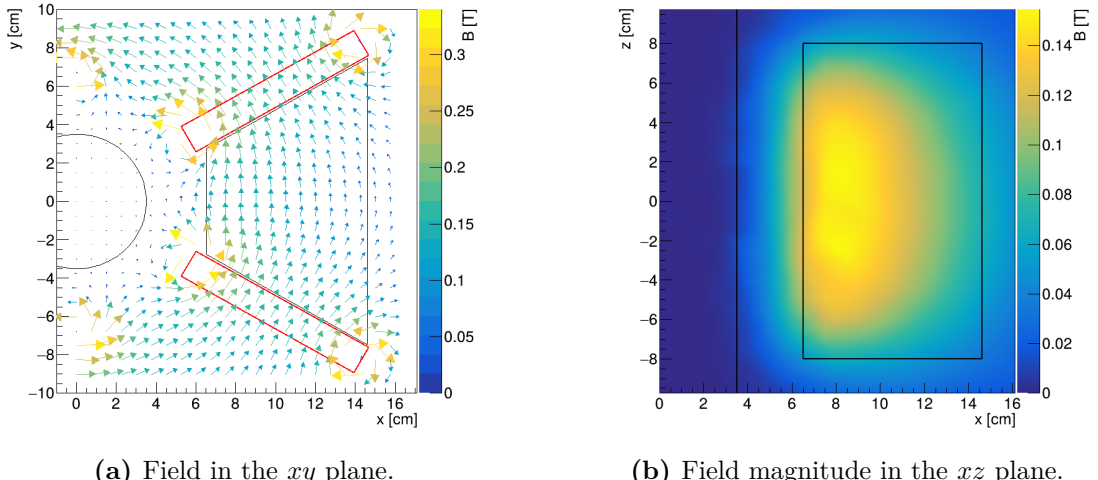


Figure 1.13: Pad layout of the OFTPC and its parameters. Pads 102, 124 and 127 are irregular, the rest has the same dimensions.

524 1.4.3 Magnetic Field Simulation

525 The magnetic field inside our detector is produced by six permanent magnets. It
526 was simulated using Ansys Maxwell (citation) which gives us values on a regular
527 grid. More details, vacuum tube, magnets (homogeneous?, density?). Visualization
528 of the magnetic field is shown in Fig. 1.14. Whenever we need to work with
529 values outside this grid, we use trilinear interpolation described below.



(a) Field in the xy plane.

(b) Field magnitude in the xz plane.

Figure 1.14: Magnetic field simulation results. The OFTPC volume and the vacuum tube are marked with black lines, the magnets are marked with red lines. **The coordinates of the magnets from the CAD drawing seem to be 9/10 of the ones from the magnetic simulation (confirm and fix).**

530 Trilinear Interpolation

531 Trilinear interpolation is a 3D generalization of linear interpolation³. It can be
 532 used to interpolate a function whose values are known on a regular grid with
 533 rectangular prism cells. We use this simple method for interpolating the magnetic
 534 field, and it is later used in Section 3.2.1 to interpolate the Ionization Electron
 535 Map, a key component of our track reconstruction algorithm. In both cases, we
 536 use a regular cubic grid (apparently it is also called a [Cartesian grid](#)).

537 Let us consider a cell of our regular grid (a cube) with an edge of length a
 538 containing the point $\mathbf{C} = (x, y, z)$ where we want to interpolate a function
 539 $f: \mathbb{R}^3 \rightarrow \mathbb{R}$. We know the values of this function at the vertices of the cell
 540 $\mathbf{C}_{ijk} = (x_0 + ia, y_0 + ja, z_0 + ka)$, where $\mathbf{C}_{000} = (x_0, y_0, z_0)$ is the origin of the
 541 cell ([is that clear?](#)), and $i, j, k \in \{0, 1\}$ are indices. We also define the points $\mathbf{C}_{ij} =$
 542 $= (x, y_0 + ia, z_0 + ja)$ and $\mathbf{C}_i = (x, y, z_0 + ia)$. Then the interpolated value $\hat{f}(\mathbf{C})$
 543 can be calculated as a composition of three linear interpolations (see Fig. 1.15):

$$\hat{f}(\mathbf{C}_{ij}) = (1 - x_d) f(\mathbf{C}_{0ij}) + x_d f(\mathbf{C}_{1ij}), \quad (1.15)$$

$$\hat{f}(\mathbf{C}_i) = (1 - y_d) \hat{f}(\mathbf{C}_{0i}) + y_d \hat{f}(\mathbf{C}_{1i}), \quad (1.16)$$

$$\hat{f}(\mathbf{C}) = (1 - z_d) \hat{f}(\mathbf{C}_0) + z_d \hat{f}(\mathbf{C}_1), \quad (1.17)$$

544 where x_d , y_d , and z_d are given as follows:

$$x_d = \frac{x - x_0}{a}, \quad y_d = \frac{y - y_0}{a}, \quad z_d = \frac{z - z_0}{a}. \quad (1.18)$$

³Linear interpolation in point $x \in (x_1, x_2)$ of a function $f: \mathbb{R} \rightarrow \mathbb{R}$ known in points $x_1 < x_2$ is the convex combination $\hat{f}(x) = (1 - x_d)f(x_1) + x_d f(x_2)$, where $x_d = \frac{x - x_1}{x_2 - x_1} \in (0, 1)$.

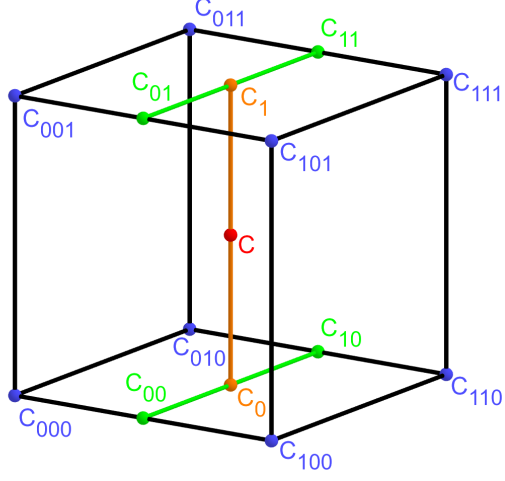


Figure 1.15: Visualization of trilinear interpolation as a composition of linear interpolations (inspired by [42]). We want to interpolate the value in the red point \mathbf{C} . First we interpolate between the four pairs of blue points sharing the last two indices along the x -axis (Eq. 1.15), then between the two pairs of the resulting green points along the y -axis (Eq. 1.16) and finally between the two resulting orange points along the z -axis to get the final red value (Eq. 1.17).

545 We can also write

$$\hat{f}(\mathbf{C}) = \sum_{i,j,k \in \{0,1\}} t_x^i t_y^j t_z^k f(\mathbf{C}_{ijk}), \quad (1.19)$$

$$t_\alpha \stackrel{\text{def}}{=} \begin{pmatrix} t_\alpha^0 \\ t_\alpha^1 \end{pmatrix} = \begin{pmatrix} 1 - \alpha_d \\ \alpha_d \end{pmatrix}, \quad (1.20)$$

546 where $\alpha \in \{x, y, z\}$ is an index. This gives a nice geometric interpretation to the
547 trilinear interpolation as shown in Fig. 1.16. From this form and the figure, it is
548 apparent that the final interpolated value does not depend on the order of axes
549 along which we perform linear interpolations (see Fig. 1.15). Furthermore, we
550 can write $\hat{f}(\mathbf{C})$ as a polynomial:

$$\hat{f}(\mathbf{C}) = \sum_{\alpha, \beta, \gamma \in \{0,1\}} \sum_{i=0}^{\alpha} \sum_{j=0}^{\beta} \sum_{k=0}^{\gamma} (-1)^{(\alpha-i)+(\beta-j)+(\gamma-k)} f(\mathbf{C}_{ijk}) x_d^\alpha y_d^\beta z_d^\gamma. \quad (1.21)$$

551 We take advantage of this form when generalizing trilinear interpolation to irreg-
552 ular grid in section 3.2.2.

553 Maybe a citation here, although I am not sure it is necessary since it could
554 be considered common knowledge. The last two equations are my own (but I'm
555 not sure that's worth mentioning unless there's a citation).

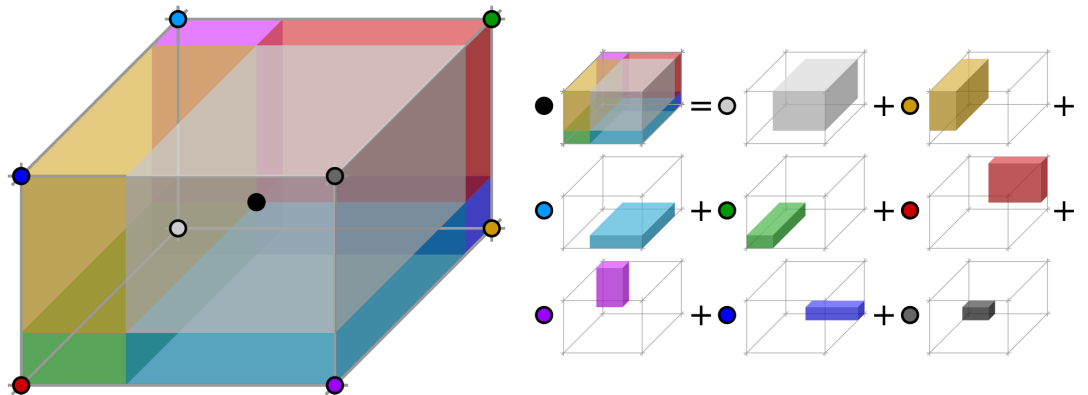


Figure 1.16: Geometric interpretation of trilinear interpolation as expressed in Equation 1.19. The colored dots represent the values in given points and the colored boxes represent the volume in the opposite corner by which the corresponding values are multiplied. The black dot represents the interpolated value which is multiplied by the entire volume [43].

2. Track Simulation

In order to develop and test the reconstruction algorithm, electron and positron tracks are simulated inside the first detector sector \mathcal{D}_1 (see Section 1.4.2) with different initial parameters (origin, initial direction and kinetic energy). Two approaches are currently used to simulate tracks, each of them for different purpose.

The **Microscopic Simulation** uses the Garfield++ toolkit [1]. Within this toolkit:

- a) Magboltz, since it is mentioned later. Or maybe just class MediumMagboltz with the collision rates?
- b) the High Energy Electro-Dynamics (HEED) program [44] is used to simulate the primary particle,
- c) the class *AvalancheMicroscopic* to simulate the drift of secondary electrons created by ionization in the gas.

This is the most precise and time-consuming simulation used; our current goal is to be able to successfully reconstruct its results and determine our best-case energy resolution.

The **Runge-Kutta Simulation** uses the 4th order Runge-Kutta numerical integration (add citation for Runge-Kutta) to simulate the trajectory of the primary particle in the electromagnetic field inside the detector. It is relatively fast since it does not simulate the secondary particles. It is used as part of our reconstruction algorithm and for testing some parts of the reconstruction.

All of these simulations require the knowledge of the electromagnetic field (both **E** and **B**) inside the detector. A uniform electric field of $400 \text{ V}\cdot\text{cm}^{-1}$ is assumed. The magnetic field was simulated in Maxwell (see Section 1.4.3). add citation

Single track in positive x direction or initial parameter randomization. Importance of gas composition, used gas compositions.

2.1 Microscopic Simulation

The microscopic simulation, the most detailed simulation used in this work, is performed using the Garfield++ toolkit [1].

The electron transport properties are simulated using the program Magboltz (add citation), (details?). Two different gas mixtures were compared – 90:10 and 70:30 Ar:CO₂. The second mixture will be used in our detector (this was probably known a priori, but the first tests that I started with used 90/10, so maybe just note that the results justify the fact so far). The temperature is set to 20 °C, the pressure is atmospheric.

The primary track is simulated using the program HEED, which is an implementation of the photo-absorption ionization model [44] (see the reference, moved it to the end of sentence). This program provides the parameters of ionizing collisions. HEED can also be used to simulate the transport of delta electrons; we do not account for these in the current simulation (but plan to include them in the future – maybe mention only in the conclusion/future section). The photons created in the atomic relaxation cascade (fluorescence reabsorption, related to the spread of avalanches in GM det.?) are also not simulated.

600 Finally, we use the microscopic tracking provided by the class *AvalancheMicroscopic* in Garfield++ to simulate the drift of the ionization electrons. Each
 601 electron is followed from collision to collision using the equation of motion and
 602 the collision rates calculated by Magboltz (how fast is this? maybe it slows down
 603 the simulation when spreading it across multiple jobs?).

604 Add more detailed and better description of HEED, and microscopic tracking
 605 (each their own subsection?). Could also mention Monte Carlo (requires gas file
 606 generation - Magboltz) and Runge-Kutta simulation implemented in Garfield,
 607 why we don't use them (another subsection? rename the section to Garfield++
 608 simulation and mention all relevant parts?).

610 2.1.1 First testing track

611 The first electron track simulated for testing purposes was chosen to have a special
 612 set of parameters:

- 613 • the starting point of the track is the origin of the coordinate system,
- 614 • the initial direction is along the positive x -axis,
- 615 • the momentum is 8 MeV/c (the kinetic energy is 7.505 MeV).

616 Such a track moves in the XZ plane in the toroidal magnetic field of the detector,
 617 because the particle's velocity vector is always perpendicular to the field. At first,
 618 we simulated such a track in 90:10 Ar:CO₂ gas mixture, later we added a simu-
 619 lation in 70:30 Ar:CO₂, which we plan to use in our detector. The comparison of
 620 both simulations is in Fig. 2.1.

621 2.1.2 Grid-like testing sample

622 In order to test all steps of the reconstruction, a sample of tracks with a grid-like
 623 distribution of parameters was generated on MetaCentrum. Five sets of 9702
 624 tracks were generated with every combination of these parameters:

- 625 • electron and positron tracks,
- 626 • 11 different kinetic energies $E_{\text{kin}} \in [3, 13]$ MeV,
- 627 • 21 different azimuth angles $\varphi \in [-16.3^\circ, 16.3^\circ]$ and
- 628 • 21 different elevation angles $\theta \in [-17.1^\circ, 17.1^\circ]$.

629 A visualization of a set of e^+/e^- tracks with the same kinetic energy is shown in
 630 Fig. 2.2 (plotting actual HEED tracks using ROOT should be also possible (but
 631 hard to make look good?)). In the 70:30 Ar:CO₂ atmosphere, each track takes
 632 5-30 CPU hours to simulate. Every tenth point on the drift line was stored, the
 633 whole sample has 3.1 terabytes (or 1.4 gigabytes without drift lines).

634 2.2 Runge-Kutta Simulation

635 The Runge-Kutta simulation in this work uses the Runge-Kutta 4th order (RK4)
 636 method to numerically integrate the equation of motion of a relativistic charged
 637 particle in an electromagnetic field. Given a system of first order differential
 638 equations

$$\frac{dy}{dt} = \mathbf{f}(t, \mathbf{y}(t)) \quad (2.1)$$

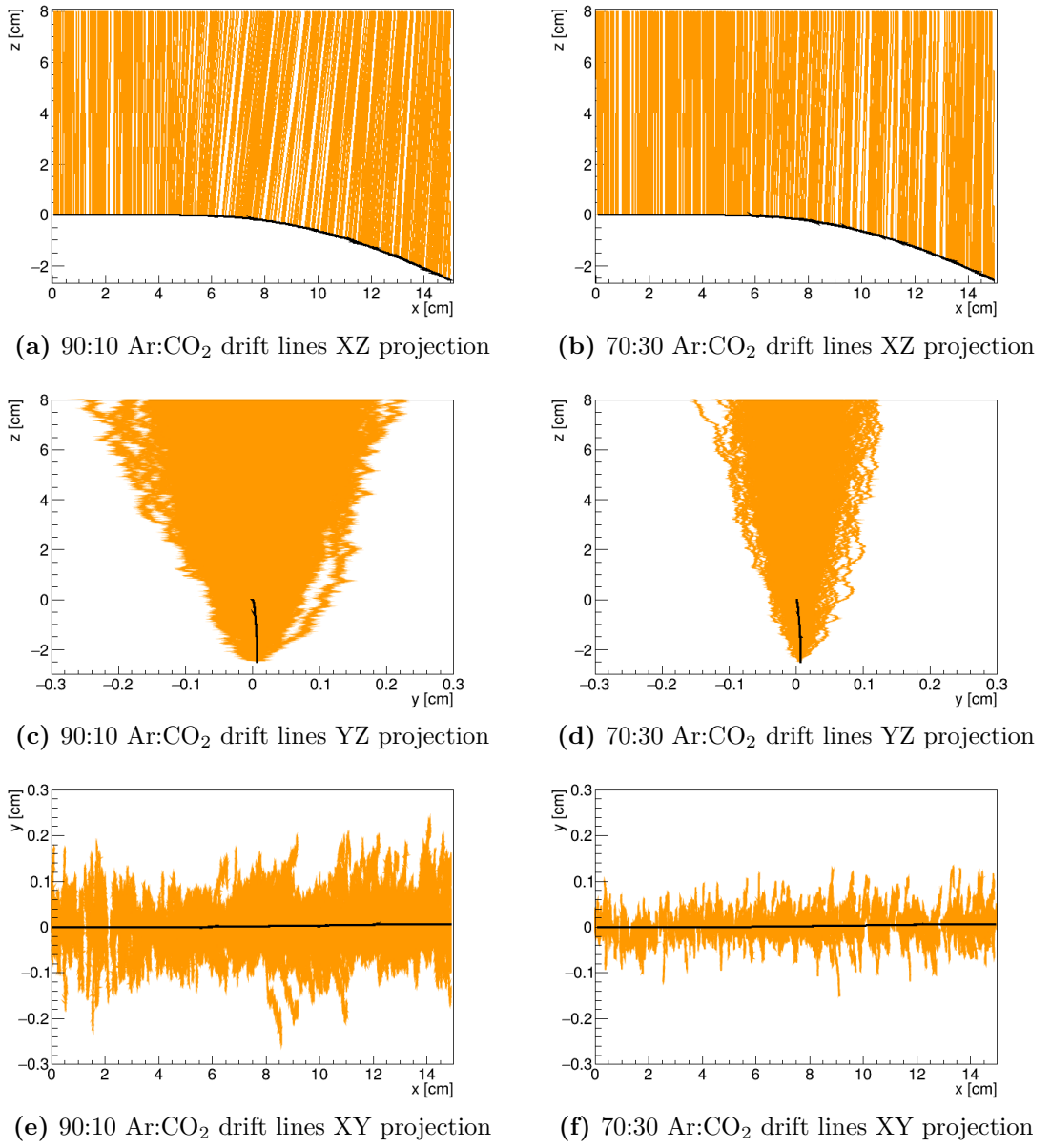


Figure 2.1: Comparison of drift lines for two different gas mixtures 90:10 and 70:30 Ar:CO₂. The electron track is marked in black, the drift lines of the ionization electrons are marked in orange. In this example, we assume a larger OFTPC volume with readout at $z = 8$ cm.

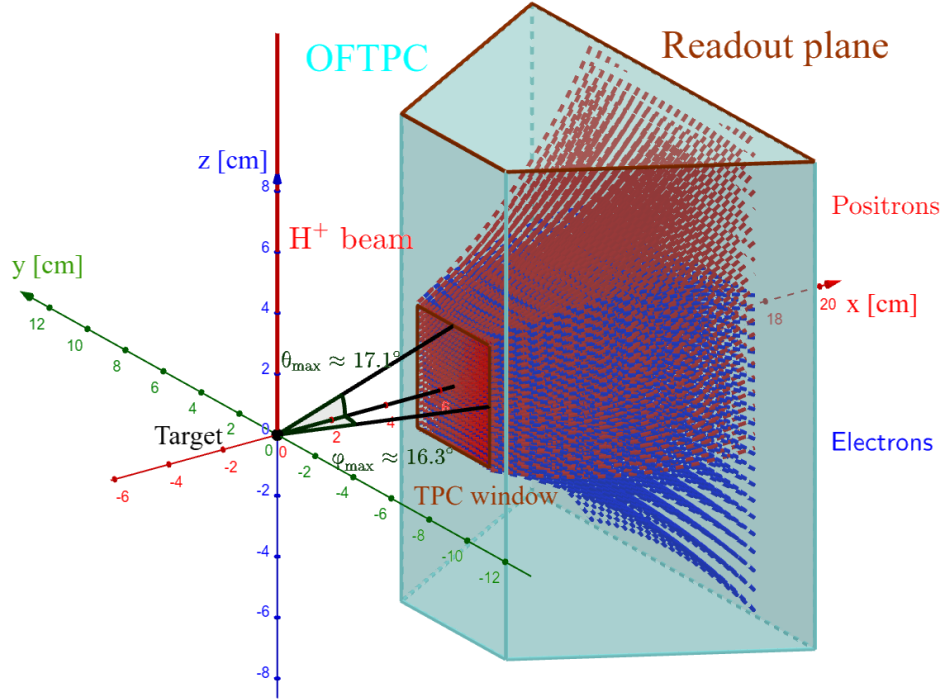


Figure 2.2: A visualization of a set of tracks from the grid-like testing sample with the same kinetic energy.

639 with an initial condition

$$\mathbf{y}(t_0) = \mathbf{y}_0, \quad (2.2)$$

640 we iteratively compute the estimate $\mathbf{y}_n = \mathbf{y}(t_n) = \mathbf{y}(t_0 + nh)$ as follows (citation?
641 common knowledge?):

$$\mathbf{k}_1 = \mathbf{f}(t_n, \mathbf{y}_n), \quad (2.3)$$

$$\mathbf{k}_2 = \mathbf{f}\left(t_n + \frac{h}{2}, \mathbf{y}_n + \frac{h\mathbf{k}_1}{2}\right), \quad (2.4)$$

$$\mathbf{k}_3 = \mathbf{f}\left(t_n + \frac{h}{2}, \mathbf{y}_n + \frac{h\mathbf{k}_2}{2}\right), \quad (2.5)$$

$$\mathbf{k}_4 = \mathbf{f}(t_n + h, \mathbf{y}_n + h\mathbf{k}_3), \quad (2.6)$$

642

$$\mathbf{y}_{n+1} = \mathbf{y}_n + \frac{1}{6}(\mathbf{k}_1 + 2\mathbf{k}_2 + 2\mathbf{k}_3 + \mathbf{k}_4). \quad (2.7)$$

643 Alternate forms (infinitely many) possible, accuracy vs computational cost. Runge-
644 Kutta-Fehlberg with adaptive step size also possible, can potentially save some
645 computation time especially in rapidly changing field (so maybe not in this case).

646 In our case, we want to integrate the equation of motion, given by the rela-
647 tivistic Lorentz force:

$$F_L^\mu = m \frac{du^\mu}{d\tau} = q F^{\mu\nu} u_\nu, \quad (2.8)$$

648 where the Einstein summation convention is used, m is the mass of the particle,
649 q is its charge, u^μ is its four-velocity, τ is the proper time (i.e., time in the particle's
650 frame of reference) and $F^{\mu\nu}$ is the electromagnetic tensor at given coordinates x^μ

651 (we consider it to be time-independent in our detector). Given the electric $\mathbf{E} =$
 652 $= (E_x, E_y, E_z)$ and the magnetic field $\mathbf{B} = (B_x, B_y, B_z)$ and using the metric
 653 signature $(+, -, -, -)$, the equation expands to

$$\frac{d}{d\tau} \begin{pmatrix} \gamma c \\ \gamma v_x \\ \gamma v_y \\ \gamma v_z \end{pmatrix} = \frac{q}{m} \begin{pmatrix} 0 & -\frac{E_x}{c} & -\frac{E_y}{c} & -\frac{E_z}{c} \\ \frac{E_x}{c} & 0 & -B_z & B_y \\ \frac{E_y}{c} & B_z & 0 & -B_x \\ \frac{E_z}{c} & -B_y & B_x & 0 \end{pmatrix} \begin{pmatrix} \gamma c \\ \gamma v_x \\ \gamma v_y \\ \gamma v_z \end{pmatrix}, \quad (2.9)$$

654 where c is the speed of light in vacuum, $\mathbf{v} = (v_x, v_y, v_z)$ is the particle's velocity
 655 and $\gamma = (1 - \frac{v^2}{c^2})^{-\frac{1}{2}}$ is the Lorentz factor (wrong magnetic field sign in the
 656 implementation???). Together with the equation

$$\frac{d}{d\tau} \begin{pmatrix} ct \\ x \\ y \\ z \end{pmatrix} = \begin{pmatrix} \gamma c \\ \gamma v_x \\ \gamma v_y \\ \gamma v_z \end{pmatrix} = u^\mu, \quad (2.10)$$

657 we get a system of eight first order differential equations for x^μ and u^μ , which
 658 we can integrate using the Runge-Kutta method described above. As a result of
 659 this integration, we get the position $\mathbf{x}(\tau_n)$, the velocity $\mathbf{v}(\tau_n)$ and the detector
 660 time $t(\tau_n)$ for every proper time $\tau_n = n\tau_{\text{step}}$. Integrating using the proper time
 661 means that the step size in t gets larger by the gamma factor $\frac{dt}{d\tau} = \gamma$ (maybe
 662 change it and integrate the detector time or adjust the step size accordingly). The
 663 only difference is in the step size (because t gets also calculated as it is among the
 664 8 variables). It might be even better to adjust the step size using approxi-
 665 mate distance traveled. As initial conditions, we use the origin of the track
 666 (x_0, y_0, z_0) , the initial velocity direction vector $\mathbf{n} = (\cos \varphi \cos \theta, \sin \varphi \cos \theta, \sin \theta)$
 667 and the kinetic energy E_{kin} (initial parameters of the simulation (fit is in chap-
 668 ter 4)), we then compute γ and $\|\mathbf{v}\|$:

$$\gamma = 1 + \frac{E_{\text{kin}}}{E_0}, \quad (2.11)$$

$$\|\mathbf{v}\| = c\sqrt{1 - \gamma^{-2}}. \quad (2.12)$$

669 2.2.1 Testing sample

670 Example of RK simulation – first testing track, randomized sample of 100000
 671 tracks (could also move them to circle 3D fit).

672 In order to test the simulation and reconstruction, a sample of 100 000 tracks
 673 with randomized parameters was generated:

- 674 the Runge-Kutta step was set to 0.1 ns (proper time, which wouldn't be a
 675 problem but this way the "spatial" step depends on energy),
- 676 the kinetic energy of the particle $E_{\text{kin}} \in [4, 12]$ MeV,
- 677 the starting point of the track is a random point in the OFTPC window,

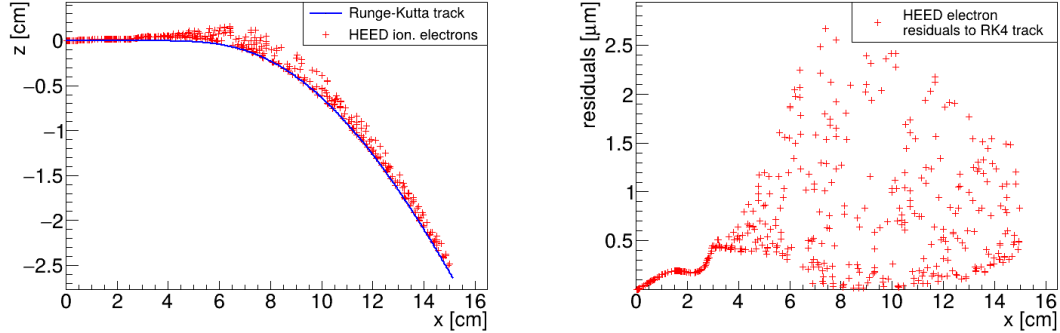


Figure 2.3: A comparison of the HEED track from the microscopic simulation in Section 2.1.1 with a Runge-Kutta track with the same initial parameters and $\tau_{\text{step}} = 0.1 \text{ ps}$ (reducing the step further doesn't make a visible difference). In the view of the tracks on the left, the distance of the HEED ionization electrons from the RK4 track is exaggerated $1000\times$. On the right, the dependence of the HEED electrons residuals (i.e., their shortest distance to the RK4 track) on their z -coordinate is shown. The images look the same even for $100,000\times$ smaller step, so the residuals are a result of something that HEED does (maybe a different interpolation technique for the magnetic field? the pattern looks similar for two different tracks so it can't be scattering).

When exaggerating, the HEED ionization electrons are moved away along the shortest line connecting them to the RK4 track. The computation of this distance is described in Section 4.3.

- 678 • the initial direction is given by the line connecting a random point on the
679 target¹ (a disc with 1 mm radius in the YZ plane).
- 680 Since the Runge-Kutta simulation is quite fast², it can be run locally on any
681 computer. Add a figure with simulated tracks (sample). An example Runge-
682 Kutta track is compared with the corresponding microscopic track in Fig. 2.3.

¹To generate a random point on the target, we generate a random angle α and a random square of the distance from origin r^2 to get a uniform distribution.

²One track with $\tau_{\text{step}} = 0.1 \text{ ps}$ takes less than one millisecond to simulate.

683 3. Track Reconstruction

684 As the first step of the reconstruction algorithm, we reconstruct the track of
685 a primary particle – either an electron or a positron. Then, using this information,
686 we determine the energy of the particle (Section 4).

687 The **Reconstruction Assuming Steady Drift** uses the standard TPC ap-
688 proach. With parallel fields, the drift inside a uniform electric field remains
689 undistorted (as shown in Equation 1.1). Therefore, we only need to reconstruct
690 the z -coordinate from the drift time using the known drift velocity. We also as-
691 sume that the readout coordinates (x' , y' , t) are known exactly, neglecting the
692 pads and time binning.

693 Reconstruction using an **Ionization Electron Map** (from now on referred
694 to as *the map*) uses a simulation of the drift of secondary (ionization) electrons
695 within the detector volume. This simulation can then be used to interpolate the
696 initial position of the secondary electrons. In the first iteration of this method
697 the readout is assumed to be continuous.

698 We present two algorithms using the map for reconstruction. The first one uses
699 a gradient descent algorithm along with trilinear interpolation (see Section 1.4.3)
700 of the map. The second method uses interpolation on the irregular inverse grid
701 with a polynomial.

702 The **Discrete Reconstruction** uses the map; instead of reconstructing the
703 exact position of each electron, we reconstruct the center of each hit pad together
704 with the time corresponding to the midpoint of the time bin. The electron count
705 in each TPC bin (consisting of the pad and the time bin) serves as an idealized
706 collected charge, which is then used as a weight in the energy reconstruction fit.

707 3.1 Reconstruction Assuming Steady Drift

708 As the first step, we tried to reconstruct a simulated electron track with a special
709 set of initial parameters, described in detail in Section 2.1.1. The starting point
710 is given by the origin of our coordinate system and its initial direction is given by
711 the positive x -axis. This means the magnetic field of our detector is perpendicular
712 to the momentum of the particle at all times, and we can reduce the problem to
713 two-dimensional space.

714 For the reconstruction, we decided to use the common method used in a stan-
715 dard TPC (similar to?, cite some source(s)!). This will allow us to explore the
716 significance of the atypical behavior in our OFTPC. Additionally, we assume the
717 readout is continuous to further simplify the problem. In this approximation, we
718 reconstruct the initial position of each ionization electron.

719 The reconstruction is then defined by the following relations between the
720 coordinates of the detector space and the readout space (see Section 1.4.2):

$$x = x', \tag{3.1}$$

$$y = y', \tag{3.2}$$

$$z = 8 \text{ cm} - d_r = 8 \text{ cm} - v_d t, \tag{3.3}$$

721 where d_r is the distance to the readout, and v_d is the drift velocity of electrons
722 in the given gas mixture. At a phenomenological level, this velocity can be con-

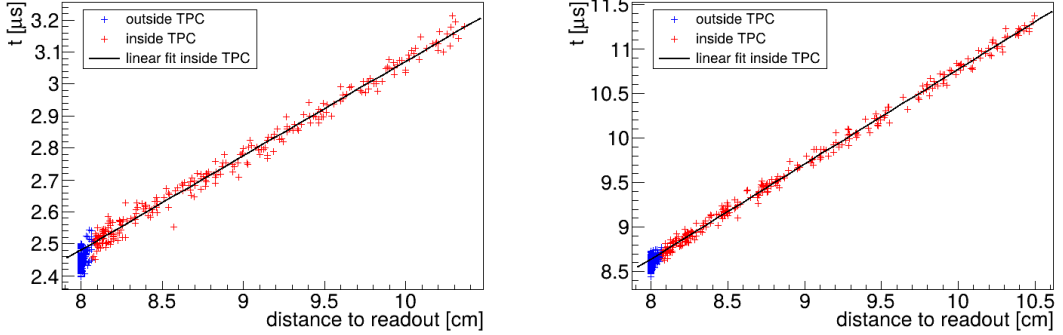


Figure 3.1: Linear fit of the drift time t dependence on the distance to the readout $d_r = 8 \text{ cm} - z$ for the ionization electrons in 90:10 (left) and 70:30 (right) Ar:CO₂ gas composition. Only electrons inside the TPC (red) are fitted. The parameters are $v_d = 3.39 \text{ cm}/\mu\text{s}$, $d_0 = -0.41 \text{ cm}$ for 90:10, and $v_d = 0.939 \text{ cm}/\mu\text{s}$, $d_0 = -0.11 \text{ cm}$ for 70:30 Ar:CO₂.

sidered as a function of the electric field \mathbf{E} and the magnetic field \mathbf{B} as shown in Equation 1.1. The Garfield++ toolkit uses this fact to accelerate their drift simulation with non-microscopic approaches (could mention in the simulation chapter). Since we assume a uniform electric field in the detector and in this approximation we want to neglect the effect of our unusual magnetic field, we consider the drift velocity constant. We can estimate the drift velocity by fitting the dependence $d_r(t)$ of ionization electrons from a simulated track with a linear function:

$$d_r(t) = v_d t + d_0. \quad (3.4)$$

The fit was applied on two tracks with different gas composition, the result is in Fig. 3.1. Compare with real drift velocities – a good indication of the tilt of drift lines. The obtained parameters are then used for the reconstruction shown in Fig. 3.2. From the residuals shown in Fig. 3.3, we can see that this reconstruction algorithm leads to significant deviations from the simulated track (up to 1.1 cm for 90:10, and up to 0.3 cm for 70:30 Ar:CO₂), especially in the faster gas mixture 90:10 (as expected – for a higher mean time between collisions in Equation 1.1, the effect of the magnetic field is bigger). These deviations are mainly caused by the shift in the x -coordinate due to the tilt of the drift lines in magnetic field. In order to account for this, we need to develop a better algorithm. There is also a small irregularity in the z -coordinate but it is comparable with the diffusion. We can/will also later show that this has a significant effect on the reconstructed energy.

3.2 Ionization Electron Map

Inside an OFTPC (more than one, also considering it a general concept rather than the specific OFTPC used at this experiment), the drift of the ionization electrons is significantly affected by its magnetic field as shown in Equation 1.1, see also Fig. 2.1. We need to take this into account for accurate reconstruction (should be easy to run the reconstruction without the map and show how much it improves the results). In the first approximation, we assume a continuous readout (i.e., we neglect the anode segmentation into pads). We can then

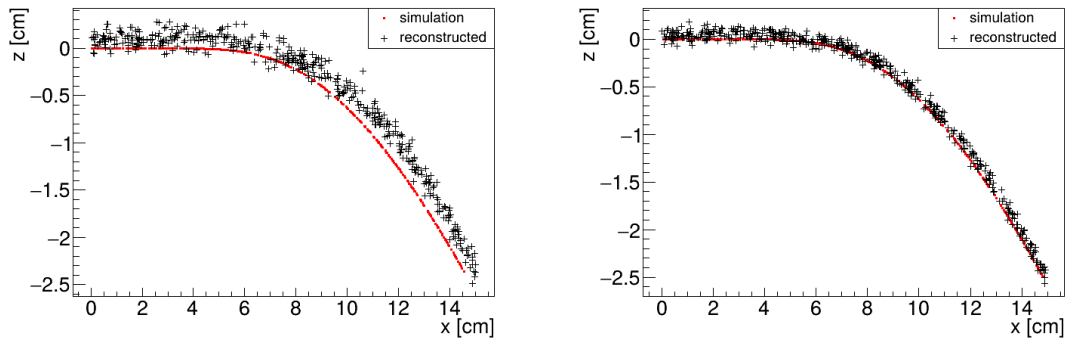


Figure 3.2: Reconstruction (black) of the starting position of ionization electrons (red) using parameters obtained from the fit (Fig. 3.1). Two gas compositions 90:10 (left) and 70:30 Ar:CO₂ (right) are compared.

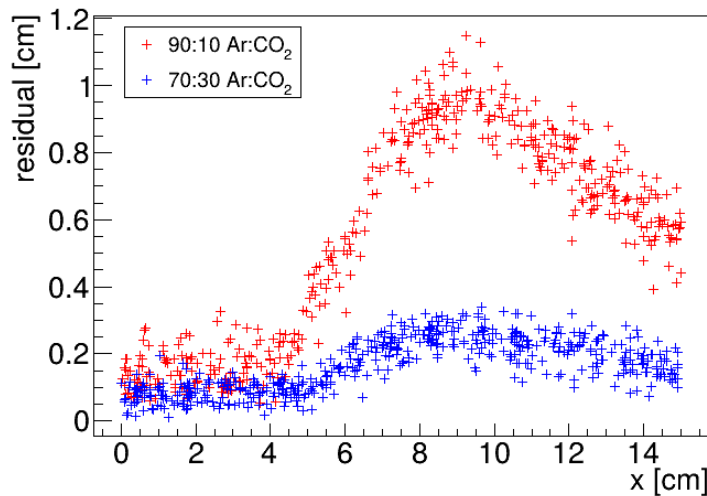


Figure 3.3: Comparison of residuals (i.e., the distance from the reconstructed point to the simulated ionization electron starting point) dependence on x for two gas mixtures 90:10 (red) and 70:30 Ar:CO₂ (blue).

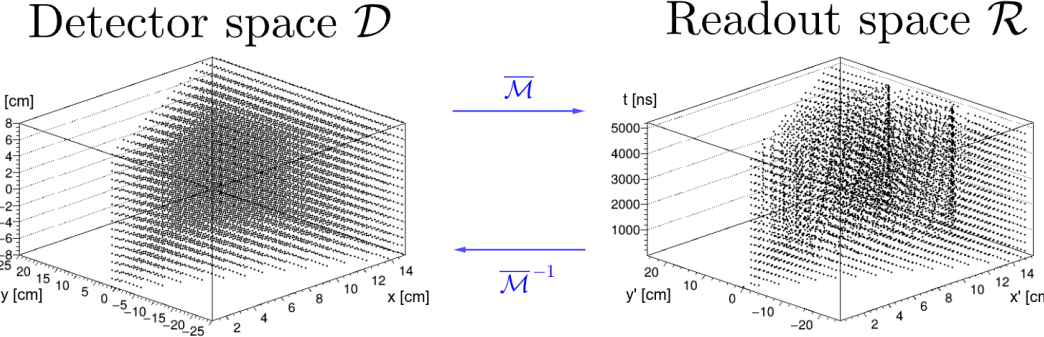


Figure 3.4: A 3D visualization of the mapping of means $\bar{\mathcal{M}}$ for the 90:10 Ar:CO₂ gas. A regular grid \mathbb{G} with $l = 1$ cm in the detector space is mapped to an irregular grid $\mathbb{G}^{-1} \equiv \bar{\mathcal{M}}(\mathbb{G})$ in the readout space.

751 reconstruct the original position of each ionization electron using its readout co-
752 ordinates. For this purpose, we use the ionization electron map.

753 The ionization electron map represents a mapping from the detector space
754 to the readout space (see Section 1.4.2). It tells us what readout coordinates
755 (x', y', t) we can expect on average for an ionization electron created at the detec-
756 tor coordinates (x, y, z). More precisely, it is a mapping to the distributions on
757 the readout space; we can simplify this as only the means $\bar{\mathcal{M}}$ and the covariance
758 matrices \mathcal{M}_Σ , assuming Gaussian distribution:

$$\bar{\mathcal{M}}: \mathcal{D} \longrightarrow \mathcal{R}, \quad (x, y, z) \longmapsto \bar{\mathbf{X}}^T \equiv (\bar{x}', \bar{y}', \bar{t}), \quad (3.5)$$

$$\mathcal{M}_\Sigma: \mathcal{D} \longrightarrow \mathbb{R}^{3 \times 3}, \quad (x, y, z) \longmapsto \Sigma \equiv \begin{pmatrix} \sigma_{x'}^2 & \text{cov}(x', y') & \text{cov}(x', t) \\ \text{cov}(y', x') & \sigma_{y'}^2 & \text{cov}(y', t) \\ \text{cov}(t, x') & \text{cov}(t, y') & \sigma_t^2 \end{pmatrix}, \quad (3.6)$$

$$\mathcal{M}: \mathcal{D} \longrightarrow D(\mathcal{R}), \quad (x, y, z) \longmapsto N(\mathbf{X}) \equiv \frac{\exp\left(-\frac{1}{2}(\mathbf{X} - \bar{\mathbf{X}})^T \Sigma (\mathbf{X} - \bar{\mathbf{X}})\right)}{\sqrt{(2\pi)^3 |\Sigma|}}. \quad (3.7)$$

759 To get an approximation of this mapping, we simulate the drift of ionization
760 electrons generated on a regular Cartesian grid $\mathbb{G} \subset \mathcal{D}$ with spacing l inside the
761 volume of our OFTPC¹ (see the visualization in Fig. 3.4). In Fig. 3.5, you can
762 see an example of drift lines from a test of the simulation. After testing runs, two
763 map simulations were made with different gas composition, their parameters are
764 shown in Table 3.1.

765 In order to get accurate results, we use the microscopic simulation of these
766 electrons described in Section 2.1 (Monte Carlo from *AvalancheMC* was also con-
767 sidered but it doesn't (didn't? CERES used it from MAGBOLTZ???) include
768 magnetic field, we can probably improve this anyway using the fast track sim-
769 ulation with map proposed in the future section). It is also useful to simulate
770 multiple (N) electrons originating from the same position so that we can account
771 for the random fluctuations due to collisions. Using the readout coordinates of
772 the electrons, we then estimate the means and the covariance matrix:

$$\bar{\mathbf{X}} = \frac{1}{N} \sum_{i=1}^N \mathbf{X}_i, \quad \Sigma = \frac{1}{N-1} \sum_{i=1}^N (\mathbf{X}_i - \bar{\mathbf{X}})(\mathbf{X}_i - \bar{\mathbf{X}})^T, \quad (3.8)$$

¹The detector walls are not considered and we simulate the drift even outside of the OFTPC which allows us to interpolate even close to the walls

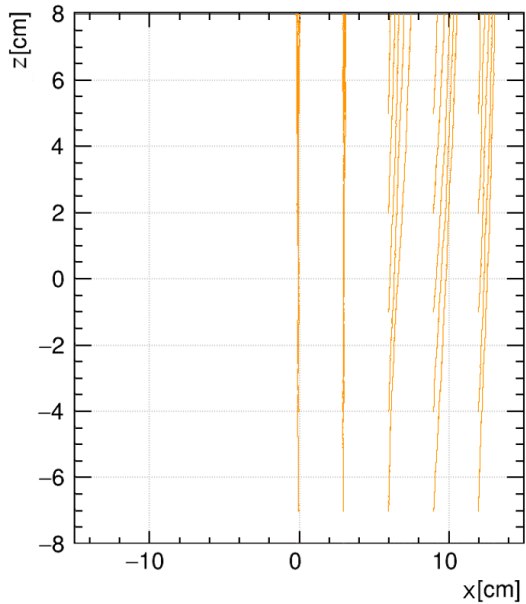


Figure 3.5: A test of the 90:10 Ar:CO₂ map simulation with spacing $l = 1.5$ cm. The resulting drift lines of evenly spaced electrons are displayed in orange.

Table 3.1: Comparison of parameters of two map simulations.

Parameter	90:10 Ar:CO ₂ map	70:30 Ar:CO ₂ map
N	100	100
l	1.0 cm	0.5 cm
z bounds	$[-8, 8]$ cm	$[-8, 8]$ cm
x bounds	$[0, 15]$ cm	$[-1.5, 15.0]$ cm
y bounds	$ y \leq x \cdot \tan \frac{\pi}{3}$	$ y \leq (x + 1.5 \text{ cm}) \cdot \tan \frac{\pi}{6}$

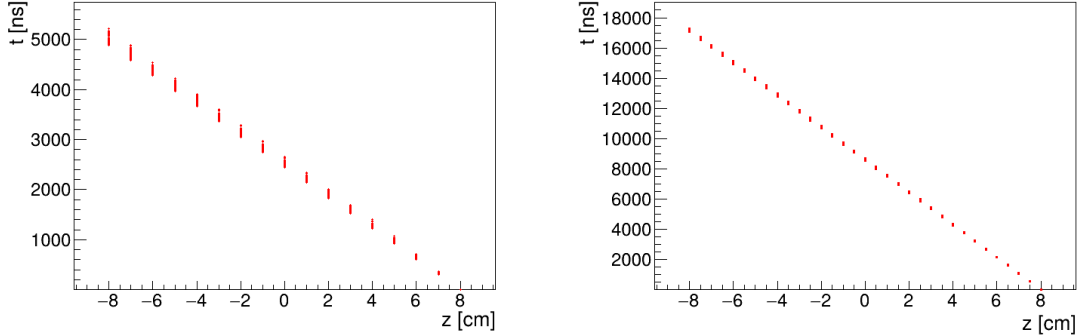


Figure 3.6: Dependence of the drift times of the simulated map $\bar{\mathcal{M}}$ on the z -coordinate. Two gas mixtures 90:10 (left) and 70:30 Ar:CO₂ (right) are compared. The spread is caused by varying Lorentz angles.

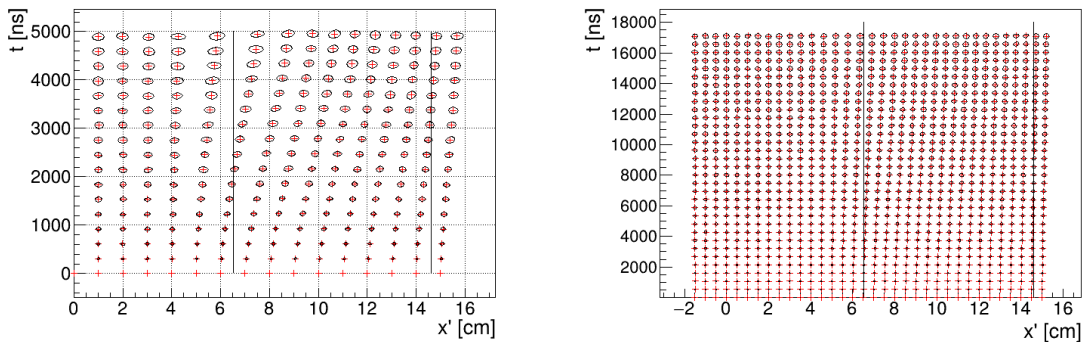


Figure 3.7: The $x't$ projection of the $\mathcal{M}(\mathbb{G}_{y=0})$ mapping of a part of the regular grid \mathbb{G} . The means $\bar{\mathcal{M}}(\mathbb{G}_{y=0})$ are marked with red crosses, and the diffusion error is denoted by black 95% confidence error ellipses computed from the diagonalized covariance matrices $\mathcal{M}_\Sigma(\mathbb{G}_{y=0})$. Two gas mixtures 90:10 (left) and 70:30 Ar:CO₂ (right) are compared. The first mixture shows differences of t for electrons with same initial z but different initial x . For the second mixture, these differences are negligible in comparison with the diffusion.

773 where \mathbf{X}_i represents the readout coordinates $(x'_i, y'_i, t_i)^T$ of the i -th electron. The
774 matrix (resp. its submatrix) can then be used to plot error ellipsoid (resp. el-
775 llipe). The axes correspond to the eigenvectors, errors along these axes for a given
776 confidence level p can be computed using the chi-squared distribution

$$\sigma_i = \sqrt{\lambda_i \chi_k^2(p)}, \quad (3.9)$$

777 where λ_i is the corresponding eigenvalue and k is the number of degrees of free-
778 dom.

779 As shown in Figs. 3.6 and 3.7, the drift times in the map are no longer propor-
780 tional to the z -coordinate due to the varying Lorentz angles in the inhomogeneous
781 magnetic field (see Equation 1.2). As expected, the effect is considerably larger in
782 gases with higher drift velocities. Similarly, the drift distortion (i.e., its deviation
783 from the vertical lines) is huge for the "faster" gas, but still significant for the
784 "slower" one, as demonstrated in Figs. 3.8 to 3.10.

785 When evaluating the map inside the grid, we use trilinear interpolation (see
786 Section 1.4.3). From now on, we will use the same symbol \mathcal{M} for this interpolated

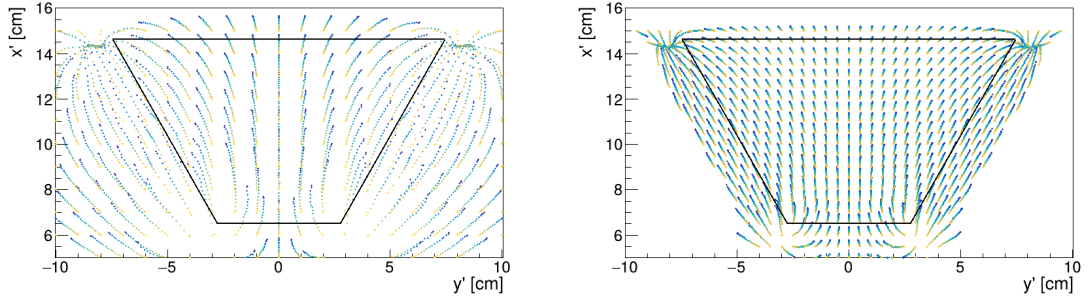
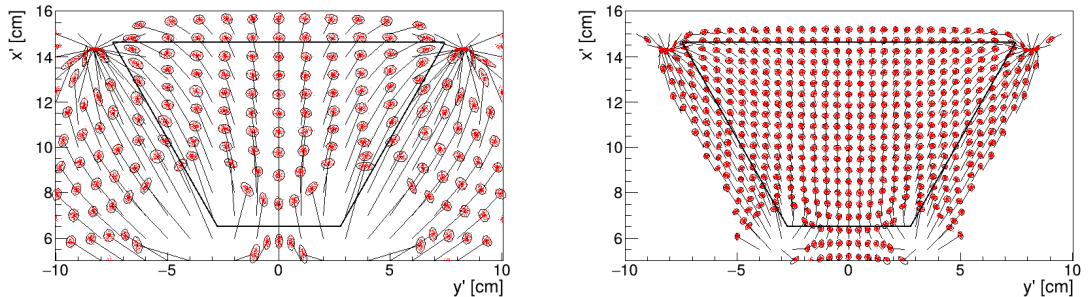
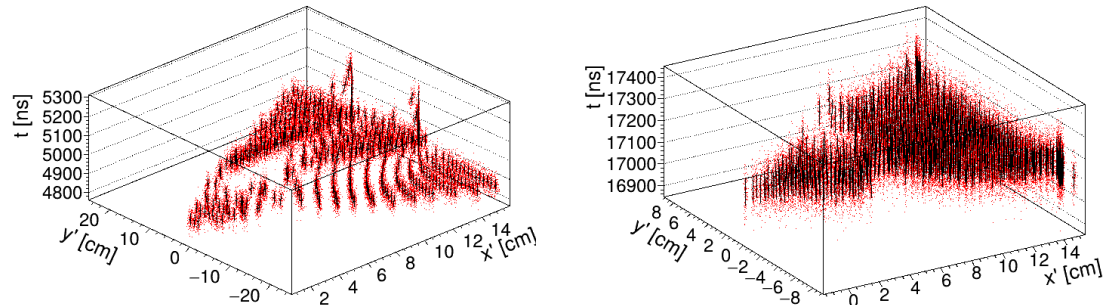


Figure 3.8: The regular grid \mathbb{G} projected by the mapping $\bar{\mathcal{M}}$ from the detector space onto the $x'y'$ plane (t is not plotted). Layers with lower z -coordinate (i.e., further away from the readout) are displayed with darker colors. The OFTPC volume is marked with black lines. Two gas mixtures 90:10 (left) and 70:30 Ar:CO₂ (right) are compared.



(a) The $x'y'$ projection of $\mathcal{M}(\mathbb{G}_{-8})$ (similar as in Fig. 3.8), the diffusion is denoted with the 95% error ellipses from the diagonalized sample covariance matrices $\mathcal{M}_{\Sigma}(\mathbb{G}_{-8}) \leftrightarrow$ Equation 3.8, and computed using Equation 3.9. The mean values $\bar{\mathcal{M}}(\mathbb{G}_{-8})$ are connected by black arrows with the corresponding starting position (x, y) of the simulated electrons. The OFTPC volume is marked with black lines.



(b) The full mapping $\mathcal{M}(\mathbb{G}_{-8})$, the diffusion is marked using standard error bars (black) from the diagonalized sample covariance matrices (Equations 3.8 and 3.9).

Figure 3.9: The $\mathcal{M}(\mathbb{G}_{-8})$ mapping of the bottom ($z = -8$ cm) layer \mathbb{G}_{-8} of the regular grid $\mathbb{G} \subset \mathcal{D}$. It includes both the mapping of means $\bar{\mathcal{M}}$ and of covariances \mathcal{M}_{Σ} . Individual electrons from the map simulation are marked with red dots. Two gas mixtures 90:10 (left) and 70:30 Ar:CO₂ (right) are compared.

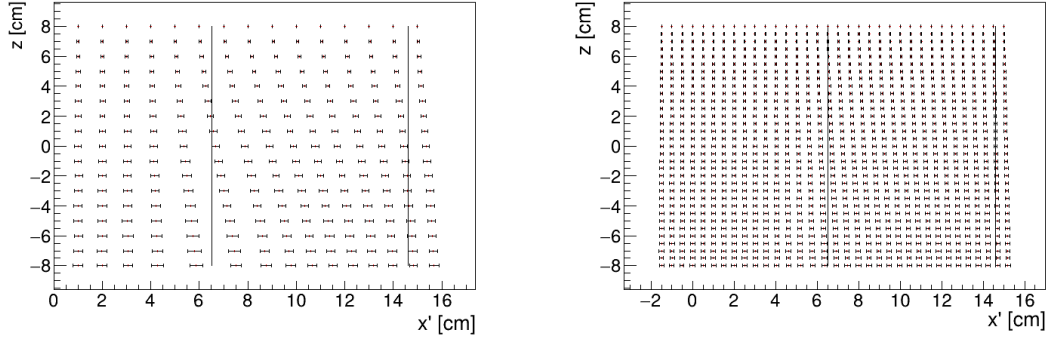


Figure 3.10: The readout coordinate x' for points on the grid $\mathbb{G}_{y=0}$ plotted against their initial coordinate z . The means are marked with red crosses, the diffusion in x' is denoted by standard error bars. Two gas mixtures 90:10 (left) and 70:30 Ar:CO₂ (right) are compared.

787 simulation.

788 Finally, we need to invert the map to get the original detector coordinates
 789 (x, y, z) from the given readout coordinates (x', y', t) . In our case, it is reasonable
 790 to assume that the mapping \mathcal{M} (we lose the information about the distribution
 791 (a wild idea how to recover this is in the Future section but it will only make sense
 792 if the GEM is already accounted for and is very preliminary as there are many
 793 factors to consider)) is one-to-one (as seen in the simulations). We implemented
 794 two methods for this purpose: the gradient descent search (Section 3.2.1) and
 795 interpolation on the inverse grid (Section 3.2.2).

796 The simulation (?) of the map is a computationally heavy task. For this rea-
 797 son, we use the MetaCentrum grid [3] to parallelize needed calculations. At first,
 798 this was done by evenly distributing the simulated electrons across the individual
 799 jobs in a simulation with only one electron per vertex in the regular grid \mathbb{G} with
 800 a spacing of one centimeter. Later, a more efficient approach was implemented,
 801 accounting for the varying lengths of the drift of individual electrons. If we index
 802 the vertices of \mathbb{G} in the order of increasing coordinates y, x, z (picture will make
 803 things clearer), we can express the number n_l of full XY layers (i.e., electrons
 804 with the same z coordinate, the mapping of one such layer is shown in Fig. 3.9b)
 805 with index less than or equal to i

$$n_l(i) = \left\lfloor \frac{i}{n_{xy}} \right\rfloor, \quad (3.10)$$

806 where n_{xy} is the number of electrons in each XY layer calculated simply by count-
 807 ing the electrons that satisfy boundary conditions for x and y . These conditions
 808 should be mentioned above; sector condition + maximal x value. The number of
 809 electrons remaining in the top layer is then

$$n_r(i) = i \bmod n_{xy}. \quad (3.11)$$

810 Finally, we can calculate the sum of the drift gaps of electrons up to index i

$$d_{\text{sum}} = (z_{\max} - z_{\min})n_{xy}n_l - \frac{n_l(n_l - 1)}{2}n_{xy}l + n_r(z_{\max} - z_{\min} - n_l l). \quad (3.12)$$

811 We then use a binary search algorithm to find the maximum index i such that
 812 the value of this sum is less than the fraction $\frac{\text{job id}}{\max \text{ job id}}$ of the total sum. This way
 813 we obtain the minimal and the maximal index of electrons simulated in the given
 814 job. Picture of the simulating grid (1 layer). zmin zmax also

815 The obtained map is then stored in a custom class template *Field*, could
 816 expand on that. Maybe earlier, since the same template is used for the magnetic
 817 field.

818 Simulation inside of one sector (at first double angle). Extra space on the
 819 sensor. Using qsub (not sure if important). Add plots of distortion of the coor-
 820 dinates.

821

822 Images to add (comparison of both simulations):

- 823 • Already have a simple 2D map visualization from the RD51 presentation,
 824 can use it or make something better
- 825 • z vs. t plot
- 826 • XY plane distortion for different z values; with arrows and error bars, for
 827 all z -layers with different colors
- 828 • XZ plane ($y = 0$) distortion in x (maybe not necessary?)
- 829 • XT plot ($y = 0$) showing (small) distortion in drift times

830

831 More images:

- 832 • Residuals of the continuous readout reconstruction.

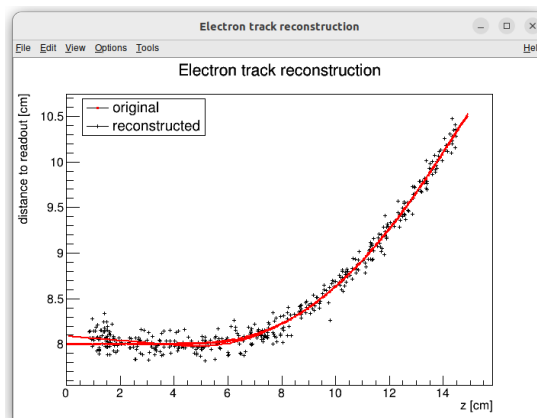


Figure 3.11: Example reconstruction with the map. Swap for better image, correct coordinates.

833 3.2.1 Gradient Descent Algorithm

834 The first implemented method of reconstruction uses a gradient descent algorithm
 835 to calculate an inversion of the map $\overline{\mathcal{M}}$ in a given point. Gradient descent is
 836 an iterative minimization algorithm for multivariate functions. Let $R \in \mathcal{R}$ be
 837 a point in the readout space; we want to find a point $D = (x, y, z) \in \mathcal{D}$ in the
 838 detector space such that

$$839 \quad \overline{\mathcal{M}}(D) = R = (x'_R, y'_R, t_R). \quad (3.13)$$

839 We define a function f_R in the readout space as a distance in this space:

$$f_R(x', y', t) = \sqrt{(x' - x'_R)^2 + (y' - y'_R)^2 + v_d^2(t - t_R)^2}, \quad (3.14)$$

840 where v_d is an approximation of the drift velocity in the TPC, obtained from the
 841 reconstruction in Section 3.1 (there will be an image with the linear fit here). We
 842 make an initial guess (actually in the original code we just take $z = 0$):

$$D_0 = (x'_R, y'_R, v_d t). \quad (3.15)$$

843 Assuming we have the n -th estimate D_n , we calculate the i -th component of the
 844 gradient of $f_R \circ \bar{\mathcal{M}}$ numerically using central differences: (signs look correct)

$$[\nabla(f_R \circ \bar{\mathcal{M}})]^i(D_n) \approx \frac{f_R(\bar{\mathcal{M}}(D_n + s \cdot e^i)) - f_R(\bar{\mathcal{M}}(D_n - s \cdot e^i))}{2s}, \quad (3.16)$$

845 where $e^i \in \mathcal{D}$ is the i -th coordinate vector and s is the step size. The step size
 846 should be sufficiently small; initially, we set it as a fraction $s = \frac{l}{10}$ of the map's
 847 grid spacing l . During the minimization, we check that $f_R(\bar{\mathcal{M}}(D_n)) < 10s$ at all
 848 times (s can (?) change – check). When using trilinear interpolation, it would be
 849 more efficient to calculate the gradient explicitly (\pm same result). This could be
 850 implemented inside the *Field* template class. The next iteration can be calculated
 851 as follows:

$$D_{n+1} = D_n - \gamma \nabla(f_R \circ \bar{\mathcal{M}})(D_n), \quad (3.17)$$

852 where $\gamma \in \mathbb{R}^+$ is the damping coefficient. It should be set to a small enough
 853 value to ensure convergence, but large enough for sufficient converging speed.
 854 The minimization stops either when the error $f_R(\bar{\mathcal{M}}(D_n))$ drops below a specified
 855 value or when the number of iterations exceeds a certain limit (in this case,
 856 a message is printed into the console). The parameters of this method can be
 857 further optimized (e.g., a better choice of γ , gradient computation); instead, we
 858 later decided to use the interpolation on the inverse grid described in the next
 859 section.

860 Measure reconstruction duration and compare it with the inverse grid inter-
 861 polation? Also compare the result? Typical evolution of D_n during search. Not
 862 sure if this has to be cited.

863 3.2.2 Interpolation on the Inverse Grid

864 Interpolation should be generally faster than the gradient descent since we don't
 865 need to iterate. We also don't need to optimize it to improve performance, if
 866 it's too slow we can even calculate the coefficients for the entire map before
 867 reconstruction (again, do some profiling).

868 The best current algorithm uses the interpolation on the inverse grid. Rather
 869 than inverting the trilinearly interpolated map using a numerical minimization
 870 method as in the previous section, we take advantage of the fact that the map
 871 $\bar{\mathcal{M}}$ is one-to-one (isomorphism is supposed to preserve structure, not sure how
 872 to interpret that here, not the best description, we already (kind of) assume it
 873 is a bijection by saying we will invert it). Since we have simulated values of this
 874 map on a regular grid in the detector space \mathcal{D} , we also know the inverse map $\bar{\mathcal{M}}^{-1}$

875 on the irregular inverse grid in the readout space \mathcal{R} . To get an approximation
 876 of the inverse map in the entire readout space, we can use interpolation (**general**
 877 **concept, the specific choice is described below**).

878 Since the inverse grid is irregular, trilinear interpolation cannot be applied.
 879 Given that the simulated map is dense enough to provide a good approximation
 880 considering the size of our pads, we can adopt a similar approach.² As shown in
 881 Equation 1.21 in Section 1.4.3, trilinear interpolation (**shouldn't need an article**
 882 **when talking about a general concept**) can be expressed as a polynomial:

$$\hat{f}(x, y, z) = axyz + bxy + cxz + dyz + ex + fy + gz + h, \quad (3.18)$$

883 where a, b, c, d, e, f, g, h are coefficients uniquely determined by the values of the
 884 function at the vertices of the interpolation cell (**can be calculated in the way**
 885 **shown in the mentioned equation, not sure what more to add**). We can generalize
 886 this for a function defined on an irregular grid. Given the function values at any
 887 eight points, we can write a system of eight linear equations

$$\begin{pmatrix} x_1y_1z_1 & x_1y_1 & x_1z_1 & y_1z_1 & x_1 & y_1 & z_1 & 1 \\ \vdots & \vdots \\ x_8y_8z_8 & x_8y_8 & x_8z_8 & y_8z_8 & x_8 & y_8 & z_8 & 1 \end{pmatrix} \begin{pmatrix} a \\ \vdots \\ h \end{pmatrix} = \begin{pmatrix} f(x_1, y_1, z_1) \\ \vdots \\ f(x_8, y_8, z_8) \end{pmatrix}, \quad (3.19)$$

888 which has a unique solution for the coefficients for most values of (x_n, y_n, z_n) and
 889 $f(x_n, y_n, z_n)$, where $n \in \{1, \dots, 8\}$.

890 This approach introduces a small complication: finding the correct pseudocell
 891 (i.e., the image of eight vertices forming a cubic cell in the regular grid) in
 892 the inverse grid. The eight irregularly spaced vertices of this pseudocell do not
 893 define a unique volume, so there are multiple possible ways to partition \mathcal{R} into
 894 pseudocells, with no obvious choice among them.

895 We are currently ignoring this problem and performing binary search along
 896 x, y, z (in this order). It shouldn't matter too much because the 70/30 map
 897 doesn't cause such a big distortion and was even accidentally extrapolated for all
 898 z different from the central plane.

²A more complicated and computationally heavy alternative would be natural neighbor interpolation or Kriging.

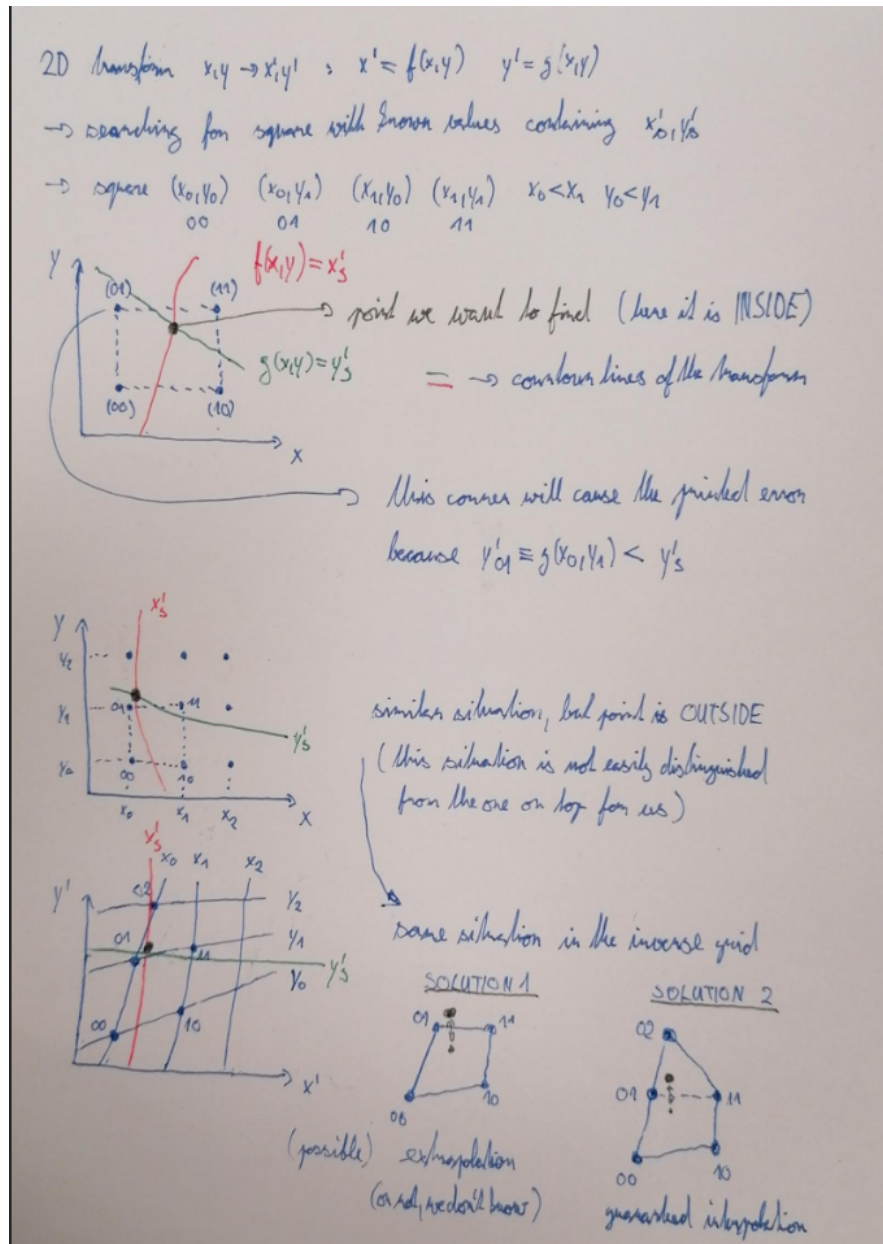


Figure 3.12: Selection of the points for interpolation. Create better images; use the explanation interpolation vs. extrapolation strange property. Solution 2 probably does not make much sense.

899 3.3 Discrete Reconstruction

900 Reconstruction with pads and time bins. Maybe testing different pads.

901 It is also possible to make this a subsection of the map, making the previous
902 subsections parts of a new subsection 'Map Inversion'.

903 In order to get a more realistic representation of a track measured in the
904 OFTPC, we need to take the discretization of the position and time data into
905 account. The readout of the OFTPC will consist of 128 pads, their layout is
906 shown in Fig. 1.13. Time is read out in discrete bins of size $t_{\text{bin}} = 100$ ns.

907 As the first approximation, we can neglect the multiplication in the triple-GEM.

and assume an ideal charge readout. The time measurement starts at the beginning of the electron/positron simulation (depending on the specific simulation it can correspond to the production in the target or when entering the OFTPC, here the specific time doesn't matter too much since the primary particle travels basically at light speed (30 ps/cm) which is circa immediate given the time binning). Randomize this time a bit and see what it does to the reconstruction. The readout coordinates $(x', y', t) \in \mathcal{R}$ of each ionization electron can be mapped to the pad coordinates $(n_{\text{pad}}, n_t) \in \mathcal{P}$:

$$n_{\text{pad}} = n: (x', y') \in \left[x_{1,n} - \frac{g}{2}, x_{2,n} + \frac{g}{2} \right] \times \left[y_{1,n} - \frac{g}{2}, y_{2,n} + \frac{g}{2} \right], \quad (3.20)$$

$$n_t = \left\lceil \frac{t}{t_{\text{bin}}} \right\rceil, \quad (3.21)$$

where $x, y_{1,n}$ and $x, y_{2,n}$ are the opposing pad corner coordinates, and g is the gap between the pads (described in detail in Section 1.4.2). This way, the closest pad is assigned to each readout position within the OFTPC volume³. Makes sense since the pads attract the electrons, the inhomogeneity of electric field is neglected. The number of electrons collected by each pad (i.e., collected charge) in each time bin is then counted and serves as a weight for the energy reconstruction. The reconstructed track consists of points for each $(n, n_t) \in \mathcal{P}$, we get these by reconstructing the position of a hypothetical electron with the readout coordinates of the pad/time bin center.⁴

$$\mathcal{D} \ni (x, y, z) = \overline{\mathcal{M}} \left(x_{c,n}, y_{c,n}, \left(n_t - \frac{1}{2} \right) t_{\text{bin}} \right). \quad (3.22)$$

³Some positions near the wall are not handled and some pads extend beyond the OFTPC volume. This is where an electric field simulation would come in handy.

⁴Mapping the center of the pad (along with the midpoint of the time bin) isn't necessarily the best approach since it might not correspond to the average parameters of an electron with these readout parameters.

925 4. Energy Reconstruction

926 The second stage is the reconstruction of the particle's energy using a fit of its
927 reconstructed track (see Section 3). We have tested three ways of reconstructing
928 the energy. Fitting is done using the MINUIT algorithm implemented in
929 ROOT [2]. Cite some CERN article directly on MINUIT, can add a section. Or
930 is it done using MIGRAD? The circle and RK4 probably was.

931 The **Cubic Spline Fit** was a tested and later rejected method of energy
932 reconstruction. It uses smoothly connected piecewise cubic polynomials between
933 uniformly spaced nodes. The reconstructed energy is calculated using the fit
934 parameters by computing the radius of curvature in different points of the fitted
935 curve using the known magnitude of the magnetic field perpendicular to the
936 trajectory. We rejected this method because the tuning of the fit turned out
937 to be unpractical compared to the other used methods. Reconstructs energy at
938 every position (even though the actual energy doesn't change much) and it might
939 be slower but no profiling has been done yet. Of course, it wasn't tested on the
940 newer track reconstruction methods at all.

941 The **Circle and Lines Fit** was chosen as an alternative since this corresponds
942 to the shape of a trajectory of a charged particle crossing a finite volume with
943 a homogeneous magnetic field. The energy of the particle can be estimated using
944 the fitted radius and the magnitude of the perpendicular magnetic field in the
945 middle of the TPC.

946 The **Runge-Kutta Fit** uses the 4th order Runge-Kutta numerical integration
947 described in Section 2.2. Initial parameters of the track (including the particle's
948 energy) are optimized so that the integrated trajectory fits to the reconstructed
949 one. This fit can also be performed as a single parameter (i.e., energy) fit if we
950 get the initial position and orientation of the particle on the entrance to the TPC
951 from previous detectors (TPX3 and MWPC, see Section 0.2).

952 4.1 Cubic Spline Fit

953 The first method for the estimation of the kinetic energy of the particle uses
954 a cubic spline fit. We use an electron track simulated using the microscopic

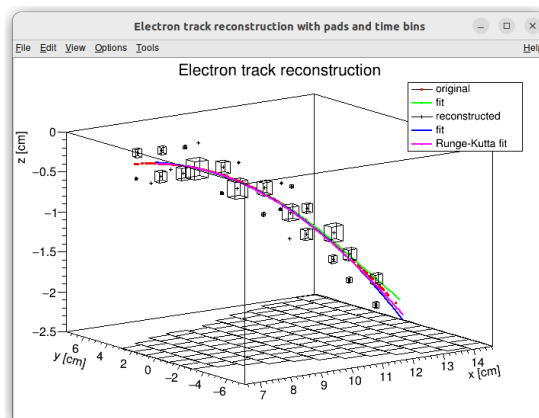


Figure 4.1: Example of a fitted reconstructed track. Swap for better image.

simulation, described in detail in Section 2.1.1. The track was reconstructed using the map described in Section 3.2.

In order to calculate the spline, we use the class *TSplines3* from ROOT. This allows us to evaluate the spline using the coordinates (x_n, z_n) of each node and the derivatives d_1, d_2 in the first and the last node. We can fit these parameters of a fixed amount of nodes to the simulated trajectory. We use the IMPROVE algorithm provided by the *TMinuit* class in ROOT (there are some guidelines for fonts in MFF UK template (Czech version) that I will eventually apply (see notes in the conclusion)). This algorithm attempts to find a better local minimum after converging (could reformulate a bit, taken word for word from some manual).

After the fit converges, we calculate an energy estimate using the radius of curvature, which we can extract from the fitted spline equation at every point of the trajectory. The part of the spline corresponding to a given node is defined as

$$z(x) = z_n + b\Delta x + c(\Delta x)^2 + d(\Delta x)^3, \quad (4.1)$$

where $\Delta x = x - x_n$ and b, c, d are coefficients. Using this equation, we derive the radius of curvature¹ as:

$$r(x) = \frac{(1 + z'^2(x))^{\frac{3}{2}}}{z''(x)} = \frac{(1 + (b + 2c\Delta x + 3d(\Delta x)^2)^2)^{\frac{3}{2}}}{2c + 6d\Delta x}. \quad (4.2)$$

Based on the geometry of our detector, we assume that the magnetic field satisfies $\mathbf{B}(x, 0, z) = (0, B(x, z), 0)$ for a track in the XZ plane. Since the electron is relativistic, the effect of the electric field on its trajectory is negligible. The Lorentz force F_L is then always perpendicular to the momentum of the electron and acts as a centripetal force F_c (not quite sure how to handle this then?):

$$\begin{aligned} \mathbf{F}_L &= \mathbf{F}_c, \\ \|e\mathbf{v} \times \mathbf{B}\| &= \frac{\gamma m_e v^2}{r}, \\ ec\beta B &= \frac{E_{0e}\beta^2}{r\sqrt{1 - \beta^2}}, \end{aligned} \quad (4.3)$$

$$\sqrt{1 - \beta^2} = \frac{E_{0e}\beta}{ecBr},$$

$$\beta^2(x) = \left[1 + \left(\frac{E_{0e}}{ecB(x, z(x))r(x)} \right)^2 \right]^{-1}, \quad (4.4)$$

where e is the elementary charge, c is the speed of light in vacuum, m_e is the rest mass of electron, $E_{0e} = m_e c^2$ is its rest energy, γ is the Lorentz factor, \mathbf{v} is the velocity of the electron, and $\beta = \frac{v}{c}$. The kinetic energy for a given point on the trajectory is then given as

$$E_{\text{kin}}(x) = \left(\frac{1}{\sqrt{1 - \beta^2(x)}} - 1 \right) E_{0e}. \quad (4.5)$$

¹For the general formula see https://en.wikipedia.org/wiki/Curvature#Graph_of_a_function.

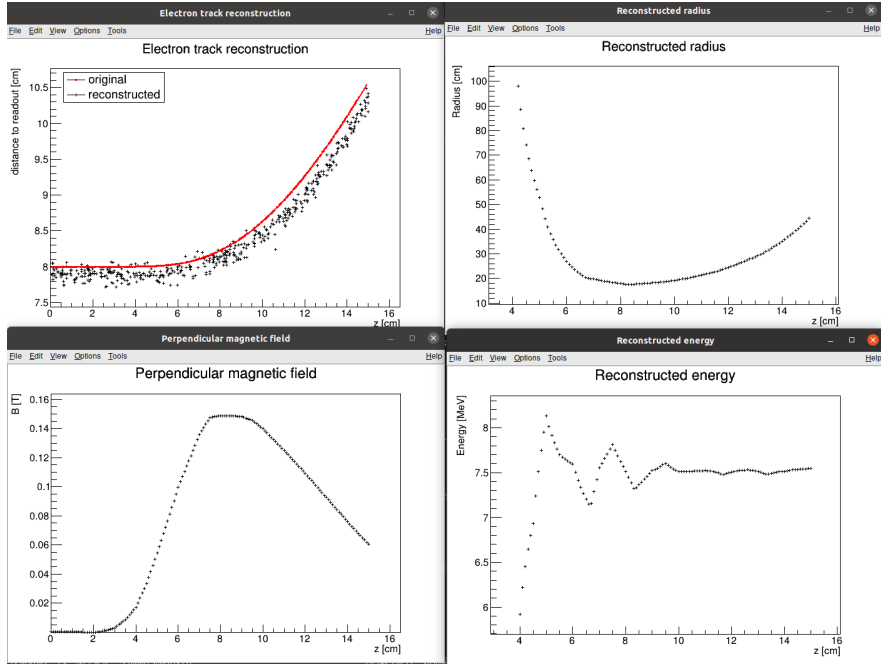


Figure 4.2: First attempt at a track reconstruction using only the drift velocity. Spline energy reconstruction attempt. Swap for better image(s) – subfigure environment, correct coordinates.

We can then average these estimates at multiple points (possibly using some weights to account for the change in accuracy, this wasn't optimized and we just ended with the graph) to get a single value. This method was later rejected in favor of the circle and lines fit (the name was already established at the beginning of the chapter) described in the next section. Add some figures.

4.2 Circle and Lines Fit

Another way to estimate the particle's kinetic energy is to fit its (??) trajectory with a circular arc with lines attached smoothly. This shape of trajectory corresponds to a movement of a charged particle through a homogeneous magnetic field perpendicular to the particle's momentum and limited to a certain volume. In general, the shape of such a trajectory with a non-perpendicularly oriented momentum is a spiral. In our case, the magnetic field is approximately toroidal and the particle motion is nearly perpendicular to it (verify, could add some magnetic field plots in different vertical planes; shouldn't have a big effect on the reconstructed radius anyway). At first, we tested a 2D version of this fit, then we adapted it to 3D.

The field in our detector is not homogeneous, it is therefore not entirely clear what value of magnetic field should be used along with the fitted radius (using equations 4.4 and 4.5) to get the best estimate for the kinetic energy. Since we only use this method as the first iteration of the particle's energy that we later refine, an optimal solution of this problem is not required. Instead, we tested two options: taking the value of the field in the middle of the fitted circular arc (or is it in the middle x of the OFTPC?) and taking the average field along it. We

haven't really tried to plot this for multiple tracks, but these estimates are saved somewhere and could be plotted.

4.2.1 Two-dimensional fit

In the 2D case, the fitted function used for the electron track² described in Section 2.1.1 (one specific track at the time, technically this function doesn't work for a curvature that gets outside of the semicircle) is defined as follows:

$$z(x) = \begin{cases} a_1x + b_1 & x < x_1 \\ z_0 + \sqrt{r^2 - (x - x_0)^2} & x_1 \leq x \leq x_2 \\ a_2x + b_2 & x > x_2 \end{cases}, \quad (4.6)$$

where $a_{1,2}$ and $b_{1,2}$ are the parameters of the lines, (x_0, z_0) is the center of the circle, r is its radius, and $(x_{1,2}, z_{1,2})$ are the coordinates of the function's nodes. That means we have 9 parameters ($z_{1,2}$ are not used in the function) along with 2 continuity conditions and 2 smoothness conditions (9 parameters of the described function, 5 of them independent after taking the conditions into account). For the fit, we use the coordinates of the nodes and the radius of the circle, which gives us 5 independent parameters (only the radius has to be larger than half of the distance between nodes). The continuity conditions (combined with the relations for $z_{1,2}$) are

$$z_{1,2} = a_{1,2}x_{1,2} + b_{1,2} = z_0 - \sqrt{r^2 - (x_{1,2} - x_0)^2}, \quad (4.7)$$

the smoothness conditions are

$$a_{1,2} = \frac{x_0 - x_{1,2}}{\sqrt{r^2 - (x_{1,2} - x_0)^2}}. \quad (4.8)$$

Together with the Equation 4.7 we get the values of $b_{1,2}$

$$b_{1,2} = z_{1,2} - a_{1,2}x_{1,2}. \quad (4.9)$$

For the coordinates of the center of the circle, we can use the fact that the center has to lie on the axis of its chord. In other words, there is a value of a parameter t such that, using the parametric equation of the axis

$$\begin{pmatrix} x_0 \\ z_0 \end{pmatrix} = \begin{pmatrix} \frac{x_1+x_2}{2} \\ \frac{z_1+z_2}{2} \end{pmatrix} + t \begin{pmatrix} \frac{z_2-z_1}{2} \\ \frac{x_1-x_2}{2} \end{pmatrix}. \quad (4.10)$$

At the same time, the center has to be in a distance of r from the nodes:

$$\begin{aligned} (x_1 - x_0)^2 + (z_1 - z_0)^2 &= r^2, \\ \left(\frac{x_1 - x_2}{2} + \frac{z_1 - z_2}{2}t \right)^2 + \left(\frac{z_1 - z_2}{2} + \frac{x_2 - x_1}{2}t \right)^2 &= r^2, \\ \left(\left(\frac{x_2 - x_1}{2} \right)^2 + \left(\frac{z_2 - z_1}{2} \right)^2 \right)t^2 + \left(\frac{x_2 - x_1}{2} \right)^2 + \left(\frac{z_2 - z_1}{2} \right)^2 - r^2 &= 0. \end{aligned} \quad (4.11)$$

²Electron tracks bend towards negative z , we need to use the upper part of the circle.

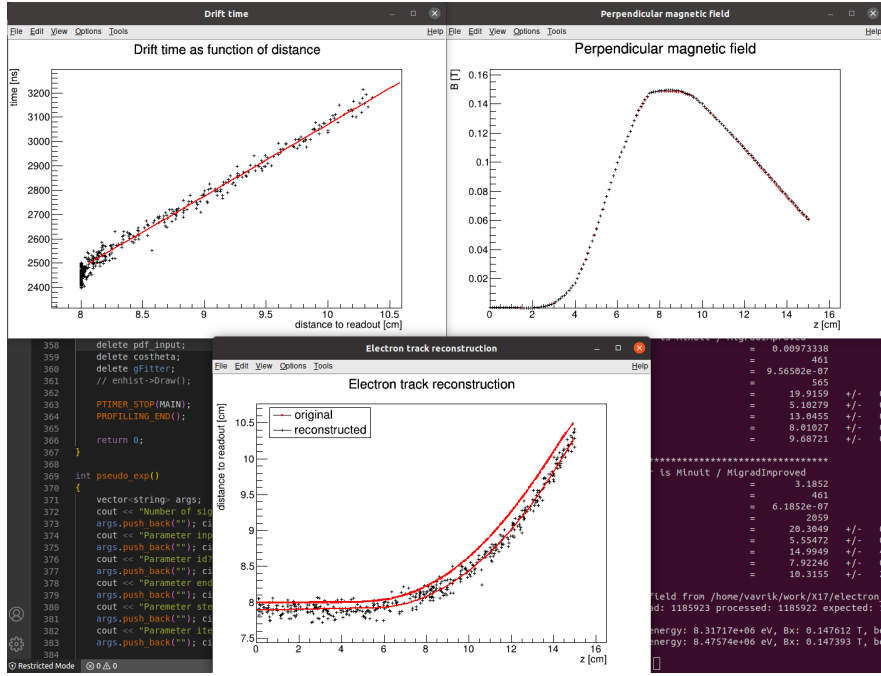


Figure 4.3: First attempt at a track reconstruction using only the drift velocity. Circle and Lines Fit in 2D. Swap for better image, correct coordinates. Bias should be described in the previous chapter, not here.

1023 Since our electron track bends towards negative z and $x_2 > x_1$, we only care
 1024 about the solution with $t > 0$

$$t = \sqrt{\frac{r^2}{\left(\frac{x_2-x_1}{2}\right)^2 + \left(\frac{z_2-z_1}{2}\right)^2} - 1}, \quad (4.12)$$

$$x_0 = \frac{x_1 + x_2}{2} + \frac{z_2 - z_1}{2} \sqrt{\frac{r^2}{\left(\frac{x_2-x_1}{2}\right)^2 + \left(\frac{z_2-z_1}{2}\right)^2} - 1}, \quad (4.13)$$

$$z_0 = \frac{z_1 + z_2}{2} - \frac{x_2 - x_1}{2} \sqrt{\frac{r^2}{\left(\frac{x_2-x_1}{2}\right)^2 + \left(\frac{z_2-z_1}{2}\right)^2} - 1}.$$

1025 The function defined in Equation 4.6 along with equations 4.8, 4.9, and 4.13
 1026 derived using the continuity and smoothness conditions (combined with the re-
 1027 lations for $z_{1,2}$) fully define our fitted function with parameters $r, x_{1,2}, z_{1,2}$. Some
 1028 pictures of the fit on the tested track. Results of the fit. Again, the actual fit
 1029 uses 8-z. Use GeoGebra schematics to generate a picture of 2D geometry.

1030 4.2.2 Three-dimensional fit

1031 In three dimensions, the shape of a trajectory of a charged particle in a uniform
 1032 magnetic field is a cylindrical helix. Nevertheless, since we assume that the
 1033 field is approximately perpendicular to the particle's momentum at all times,
 1034 we will further approximate the trajectory with a circular arc $\mathbf{X}_C(\phi)$ (with lines
 1035 $\mathbf{X}_{L1}(t), \mathbf{X}_{L2}(s)$ attached smoothly).

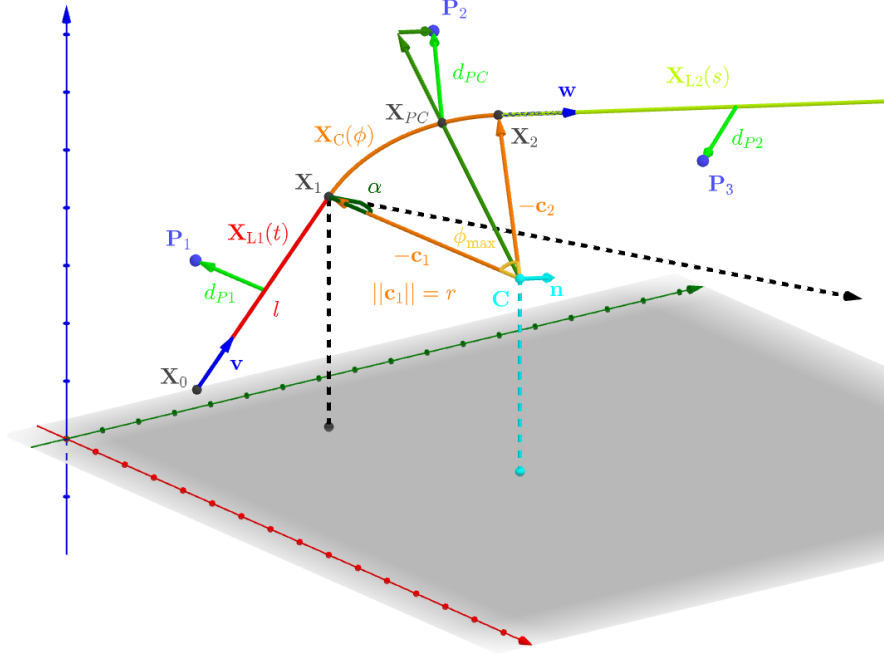


Figure 4.4: Visualization of the 3D geometry of the Circle and Lines Fit and its parameters.

We assume that the initial position $\mathbf{X}_0 = (x_0, y_0, z_0)$ and direction θ, φ (spherical angles as in Section 1.4.2) are known, since this information will be provided by TPX3 and MWPC layers. We could further refine it at the end of the current algorithm with some kind of global fit (all detector layers). The fit then has four free parameters (see Fig. 4.4):

- the length of the first line l (as measured from the initial position),
- the radius of the circular arc r ,
- the central angle of the arc $\phi_{\max} \in [0, 2\pi]$,
- the direction of the curvature given by the angle $\alpha \in [0, 2\pi]$ (right-handed with respect to the particle direction, $\alpha = 0$ if the particle curves towards negative z in a plane given by $\hat{\mathbf{z}}$ and the direction vector).

Using these parameters, we can derive a parametrization of the whole curve. Let \mathbf{v} be the initial unit direction vector, i.e., using the spherical angles

$$\mathbf{v} = (\cos \varphi \cos \theta, \sin \varphi \cos \theta, \sin \theta)^T, \quad (4.14)$$

then we can parameterize the first line as follows:

$$\mathbf{X}_{L1}(t) = \mathbf{X}_0 + t\mathbf{v} \quad t \in [0, l]. \quad (4.15)$$

This gives us the starting point of the arc

$$\mathbf{X}_1 = \mathbf{X}_{L1}(l) = \mathbf{X}_0 + l\mathbf{v}. \quad (4.16)$$

The vector \mathbf{c}_1 that lies in the plane of curvature and points from \mathbf{X}_1 to the center of curvature can be calculated using a composition of rotations. First, we rotate \mathbf{v} to point in the $\hat{\mathbf{x}}$ direction, the normal for $\alpha = 0$ than points in the $-\hat{\mathbf{z}}$ direction,

1054 we apply the α rotation and reverse the rotations into the $\hat{\mathbf{x}}$ direction: (parameters
1055 are explained in the bullet points above)

$$\begin{aligned}
\mathbf{c}_1 &= R_z(\varphi)R_y(-\theta)R_x(\alpha)R_y\left(\frac{\pi}{2}\right)R_y(\theta)R_z(-\varphi)\mathbf{v}, \\
&= R_z(\varphi)R_y(-\theta)R_x(\alpha)(-\hat{\mathbf{z}}), \\
&= \begin{pmatrix} \cos \varphi & -\sin \varphi & 0 \\ \sin \varphi & \cos \varphi & 0 \\ 0 & 0 & 1 \end{pmatrix} \begin{pmatrix} \cos \theta & 0 & -\sin \theta \\ 0 & 1 & 0 \\ \sin \theta & 0 & \cos \theta \end{pmatrix} \begin{pmatrix} 1 & 0 & 0 \\ 0 & \cos \alpha & -\sin \alpha \\ 0 & \sin \alpha & \cos \alpha \end{pmatrix} \begin{pmatrix} 0 \\ 0 \\ -1 \end{pmatrix}, \quad (4.17) \\
&= \begin{pmatrix} -\sin \alpha \sin \varphi + \cos \alpha \cos \varphi \sin \theta \\ \sin \alpha \cos \varphi + \cos \alpha \sin \varphi \sin \theta \\ -\cos \alpha \cos \theta \end{pmatrix}.
\end{aligned}$$

1056 Signs should be correct because right-handed rotation around y rotates z into x
1057 and this one is the opposite. Seems like in this part of the code θ is actually taken
1058 from the pole. Instead of the equator plane. Similarly by rotating $\hat{\mathbf{y}}$, we can get
1059 the normal vector $\mathbf{n} = \mathbf{v} \times \mathbf{c}_1$ perpendicular to the plane of the trajectory:

$$\mathbf{n} = R_z(\varphi)R_y(-\theta)R_x(\alpha)\hat{\mathbf{y}} = \begin{pmatrix} -\cos \alpha \sin \varphi - \sin \alpha \cos \varphi \sin \theta \\ \cos \alpha \cos \varphi - \sin \alpha \sin \varphi \sin \theta \\ \sin \alpha \cos \theta \end{pmatrix}. \quad (4.18)$$

1060 This allows us to express the coordinates of the center \mathbf{C} of the circular arc:

$$\mathbf{C} = \mathbf{X}_1 + r\mathbf{c}_1. \quad (4.19)$$

1061 We can then get the parametrization and the endpoint of the circular arc using
1062 Rodrigues' rotation formula: (all parameters explained in the bullet points above)

$$\begin{aligned}
\mathbf{c}_2 &= \mathbf{c}_1 \cos \phi_{\max} + (\mathbf{n} \times \mathbf{c}_1) \sin \phi_{\max} + \mathbf{n}(\mathbf{n} \cdot \mathbf{c}_1)(1 - \cos \phi_{\max}), \\
&= \mathbf{c}_1 \cos \phi_{\max} - \mathbf{v} \sin \phi_{\max},
\end{aligned} \quad (4.20)$$

$$\mathbf{X}_C(\phi) = \mathbf{C} - r(\mathbf{c}_1 \cos \phi - \mathbf{v} \sin \phi) \quad \phi \in [0, \phi_{\max}], \quad (4.21)$$

$$\mathbf{X}_2 = \mathbf{X}_C(\phi_{\max}) = \mathbf{C} - r\mathbf{c}_2, \quad (4.22)$$

1063 and if we define the direction vector of the second line, we also get its parametriza-
1064 tion

$$\mathbf{w} = \mathbf{v} \cos \phi_{\max} + (\mathbf{n} \times \mathbf{v}) \sin \phi_{\max} = \mathbf{v} \cos \phi_{\max} + \mathbf{c}_1 \sin \phi_{\max}, \quad (4.23)$$

$$\mathbf{X}_{L2}(s) = \mathbf{X}_2 + s\mathbf{w} \quad s \in [0, \infty). \quad (4.24)$$

1065 The fit is performed as a (weighted) least square minimization (MIGRAD
1066 ROOT), therefore we need to derive the distance of any point \mathbf{P} to the fitted
1067 curve. For the first line, we simply compute the parameter value of the closest
1068 point on the line:

$$\begin{aligned}
t_P &= \mathbf{v} \cdot (\mathbf{P} - \mathbf{X}_1), \\
d_{P1} &= \|\mathbf{P} - \mathbf{X}_{L1}(t_P)\|.
\end{aligned} \quad (4.25)$$

1069 If the parameter value is outside of its bounds defined above, we take the boundary
1070 value instead. The distance to the second line is computed likewise. For the

1071 circular arc (specific circular arc in the fit), we find the closest point (on the arc)
1072 by projecting the center connecting line onto the arc plane:

$$\mathbf{X}_{PC} = \mathbf{C} + r \frac{(\mathbf{P} - \mathbf{C}) - (\mathbf{n} \cdot (\mathbf{P} - \mathbf{C}))\mathbf{n}}{\|(\mathbf{P} - \mathbf{C}) - (\mathbf{n} \cdot (\mathbf{P} - \mathbf{C}))\mathbf{n}\|}, \quad (4.26)$$

$$d_{PC} = \|\mathbf{P} - \mathbf{X}_{PC}\| \quad (4.27)$$

1073 If the point \mathbf{X}_{PC} lies outside of the arc, distance to the closest endpoint is taken
1074 instead. The shortest distance out of d_{P1}, d_{PC}, d_{P2} is then taken as the distance
1075 to the curve. When calculating energy with the average field, only the arc is
1076 considered. Middle field in the current implementation taken in the middle x
1077 plane (intersection with the curve). TVirtualFitter+MIGRAD, maximal num of
1078 iterations, toleration. Different uncertainties in x, y, z not taken into account.

1079 Fit details (parameter bounds, initial setting).

1080 4.2.3 Testing on a Runge-Kutta sample

1081 The three dimensional circle and lines fit was tested on a sample of Runge-Kutta
1082 tracks with randomized parameters described in Section 2.2.1. These tracks of
1083 primary electrons and positrons consist of points calculated with the RK4 algo-
1084 rithm for a given proper time step (step can be adjusted by dividing by the gamma
1085 factor → detector time). Fitting with circle only was also partially implemented
1086 (didn't work but could be fixed/tuned).

1087 4.3 Runge-Kutta Fit

1088 The Runge-Kutta fit uses the Runge-Kutta 4th order (RK4) numerical integra-
1089 tion of the equation of motion (see Section 2.2) to find the best values of the track
1090 parameters – the track origin, initial velocity direction and the kinetic energy. In
1091 order to speed up the energy reconstruction, an initial guess of these parameters
1092 can be obtained from the 3D circle fit described in the previous section. Fur-
1093 thermore, assuming we know the track origin and orientation, we can perform
1094 a single parameter fit of the kinetic energy (do some profiling and show that it is
1095 faster – below in the microscopic testing).

1096 The fit is performed as a least square minimization of the (weighted) distances
1097 of the track points (true ionization vertices from the simulation or reconstructed
1098 points). The simulated RK4 track consists of line segments with known endpoints,
1099 therefore we can calculate the distance of a point from this segment analogically
1100 to Equation 4.25 with \mathbf{v} given as a unit vector in the direction of the segment.

1101 We need to find the segment with the lowest distance. We assume, that the
1102 distance $d_{\mathbf{P}}(\tau)$ of a point \mathbf{P} to the point on the track (a curve parameterized
1103 by the proper time τ) $\mathbf{X}(\tau)$ has a single minimum (local and global), no local
1104 maximum (except the interval endpoints) and no saddle point

$$\exists! \tau_{\min} \in [0, \tau_N]: (\forall \tau \in [0, \tau_N]: d_{\mathbf{P}}(\tau) \geq d_{\mathbf{P}}(\tau_{\min})) \vee \frac{dd_{\mathbf{P}}}{d\tau}(\tau_{\min}) = 0, \quad (4.28)$$

1105 where N is the number of RK4 steps. This is a reasonable assumption for a track
1106 with an approximate shape of a circular arc with a radius r , since the distance d

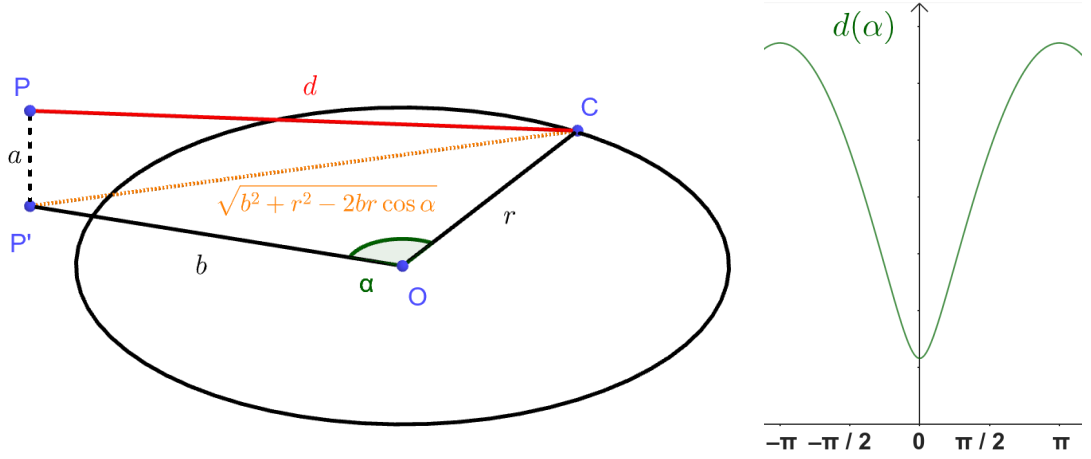


Figure 4.5: Demonstration of the convexity of the distance function $d(\alpha)$ for a circular track (see Equation 4.29).

from a point **C** on the corresponding circle of a point **P** offset by a from the arc plane and by b from the arc's center when projected on its plane is given by the law of cosines:

$$d^2 = a^2 + b^2 + r^2 - 2br \cos \alpha, \quad (4.29)$$

where α is the angle between points **C** and **P** as seen from the center of the arc (see Fig. 4.5). This function is strictly convex for $\alpha \in (-\frac{\pi}{2}, \frac{\pi}{2})$ and in our case, the center of the arc lies outside of the detector and α is restricted to a small interval around zero (especially considering that the initial guess should make the fitted trajectory reasonably close to any relevant point, in the worst-case scenario, the distance is overestimated which should keep the fit from converging to such solutions).

In a more general case, if we consider the vector $\mathbf{a}(\tau) = \mathbf{P} - \mathbf{X}(\tau)$ whose size is $\|\mathbf{a}(\tau)\| = d_{\mathbf{P}}(\tau)$, then we get

$$2d_{\mathbf{P}} \frac{dd_{\mathbf{P}}}{d\tau} = \frac{dd_{\mathbf{P}}^2}{d\tau} = 2\mathbf{a} \cdot \frac{d\mathbf{a}}{d\tau} = -2\mathbf{a} \cdot \frac{d\mathbf{X}}{d\tau}, \quad (4.30)$$

therefore for the derivative of $d_{\mathbf{P}}(\tau)$ to be zero, $\mathbf{a}(\tau)$ has to be perpendicular to the tangent of the track. In 3D, for a given $\mathbf{X}(\tau)$, this condition restricts **P** to a plane. This means that on a curving track, for any two points $\mathbf{X}(\tau_1), \mathbf{X}(\tau_2)$ with non-parallel tangents, we can find a point **P** that has $\frac{dd_{\mathbf{P}}}{d\tau}(\tau_1) = \frac{dd_{\mathbf{P}}}{d\tau}(\tau_2) = 0$, which violates the assumption 4.28. If we have a circle-and-lines track as described in the previous sections, such a point has to lie outside of the circular sector given by the arc.

For a planar track $\mathbf{X}(\tau) = (X_1(\tau), X_2(\tau))$, the envelope of all its normals is the evolute of the curve (i.e., the set of centers of all its osculating circles). If the track has a monotonous tangent angle

$$\alpha(\tau) = \text{atan} \frac{\frac{dX_2}{d\tau}}{\frac{dX_1}{d\tau}} \quad (4.31)$$

with minimal and maximal α differing by less than π (i.e., the track changes direction by less than 180°), then all intersections of the track's normals must lie

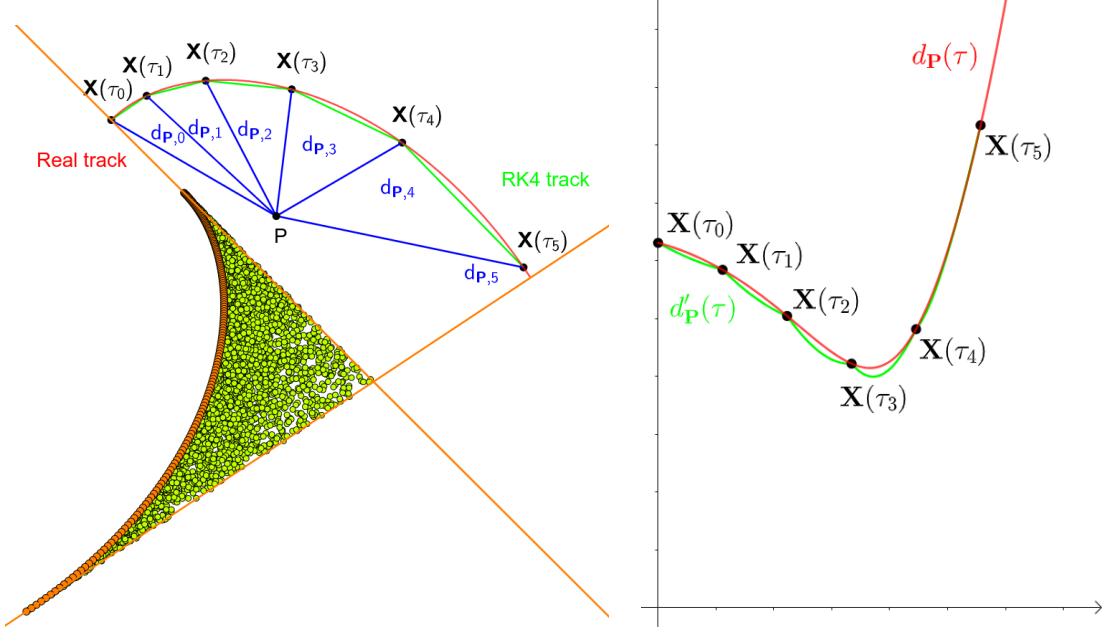


Figure 4.6: An example track (red) with a polygonal chain approximation (green, representing a RK4 simulation). The distance of the point \mathbf{P} from the chain is found using a binary search among the distances to the vertices $d_{\mathbf{P}}(\tau_i)$ (blue) and subsequently calculating the distance to segments neighboring the found vertex (thus finding the minimum of the function $d'_{\mathbf{P}}(\tau)$, function $d_{\mathbf{P}}(\tau)$ for the actual track is showed for reference). This approach works if the condition 4.28 is satisfied, which is not the case for a point from the green area bordered by the normals at endpoints and the evolute of the track (orange).

in an area bordered by the evolute and the normals at the beginning and the end of the curve (from their intersection with the evolute to their mutual intersection, see Figs. 4.6 and 4.7). Together, these three boundaries define a closed shape that will lie outside of the OFTPC for a typical track in our detector³.

With the assumption 4.28, we can find the segment on the RK4 track with the lowest distance to a given point \mathbf{P} using a binary search algorithm. Let the distance of the point from the n -th vertex be $d_{\mathbf{P},n} = d_{\mathbf{P}}(\tau_n)$. Then the difference $\Delta d_{\mathbf{P},n} = d_{\mathbf{P},n} - d_{\mathbf{P},n-1}$ satisfies

$$\begin{aligned}\Delta d_{\mathbf{P},n} &< 0 \quad \forall n \text{ such that } \tau_n < \tau_{\min}, \\ \Delta d_{\mathbf{P},n} &> 0 \quad \forall n \text{ such that } \tau_{n-1} > \tau_{\min}.\end{aligned}\tag{4.32}$$

Therefore, we can search for the segment containing $d_{\mathbf{P},\min} = d_{\mathbf{P}}(\tau_{\min})$ with binary search starting with $\Delta d_{\mathbf{P},1}$ and $\Delta d_{\mathbf{P},N}$, then calculate the difference $\Delta d_{\mathbf{P},m}$ for the middle index $m = \left\lfloor \frac{N+1}{2} \right\rfloor$. If $\Delta d_{\mathbf{P},m} > 0$ (minor bug in the implementation – if the value for the maximal index is negative, it shouldn't change anything), we can replace the higher index with m , otherwise we replace the lower index. The search stops when the difference between the minimal and maximal index is one. Would it be better if they were the same (maybe not)? Then the minimal

³The smallest anticipated radius of curvature is 39 cm for an electron or positron with a kinetic energy 3 MeV in a 0.3 T magnetic field. All points in the exclusion area must be farther from the track and therefore outside the OFTPC.

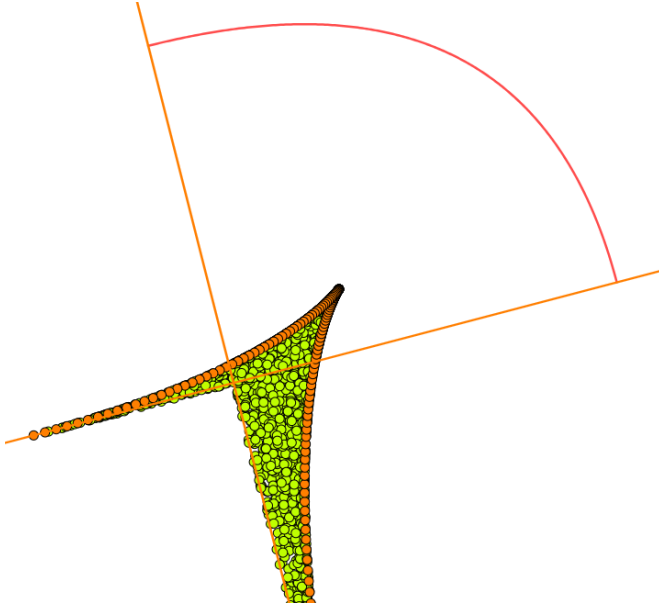


Figure 4.7: An exclusion area (green) of a track (red) bordered by its evolute and the normals at endpoints (orange), where the assumption 4.28 is violated. Unlike the track in Fig. 4.6, this track has a minimal curvature point in the middle, corresponding to the cusp on its evolute.

1146 value is $d_{P,n-1}$ or $d_{P,N}$ and we can take the minimum of the distances from the two
 1147 segments connected to $n - 1$. Currently taking the maximal index (and starting
 1148 at $N - 2$ maximal index $\leftrightarrow N - 1$ -th point), this should be equivalent, since either
 1149 $\Delta d_{P,\max} > 0$ (in the code is equivalent to max-1 here) or we are at $N - 1$. The
 1150 minimum of the two distances still taken.

1151 Same details with MIGRAD etc. as previously.

1152 4.3.1 Testing on a microscopic sample

1153 The Runge-Kutta fit together with the 3D circle-and-lines pre-fit was tested on
 1154 a sample of tracks simulated using the microscopic simulation described in Sec-
 1155 tion 2.1. At first, few tracks with randomized initial parameters (same as the
 1156 Runge-Kutta sample in Section 2.2.1) were generated for preliminary testing.
 1157 Later, a sample with a grid-like distribution of track parameters was generated
 1158 (see Section 2.1.2 for details).

1159 Initial parameters of the HEED track (also should be in the first testing track).
 1160 Initial parameters set in the circle fit (if electron set alpha one way, otherwise
 1161 other way) and parameter bounds.

1162 Conclusion

1163 Here or at the end of each section. Something about the future of this work?

1164

1165 Notes

1166 General notes about the thesis:

- 1167 • Check that all of the classes and other code are marked the same way in
1168 the text. I used italics somewhere, could use different font for this instead.
- 1169 • Check unbreakable space in front of articles. Remove excessive article usage
1170 with proper nouns.
- 1171 • Currently using margins for single-sided printing (bigger on the left side).
- 1172 • Check that present tense is used
- 1173 • Active vs passive voice usage
- 1174 • American English quotation marks (") instead of British English (').
- 1175 • Some of the overfull hbox warnings might change if duplex printing is used
1176 (they generate black rectangles on the edge of the page), leaving them be
1177 for now
- 1178 • Check nobreakdash usage (is it always necessary)
- 1179 • Check capitalized references (e.g., Figure, Section, Equation)
- 1180 • Check $\backslash(...\backslash)$ math mode instead of $\$...$$. (actually unlike $\backslash[...\backslash]$ math mode,
1181 there is apparently no real benefit to this clumsy syntax)
- 1182 • Use siunitx package to ensure correct formatting, physics package for derivatives.
- 1184 • Check other stuff that's written in the MFF UK template. Apparently it
1185 has since been updated and there are some differences (check for them).
- 1186 • Check correct subscripts in equation (italics vs no italics)
- 1187 • Consistent bold marking of points/vectors
- 1188 • Correct footnotes (capital letters, etc.).
- 1189 • Might have to mention GeoGebra as per the non-commercial license agree-
1190 ment (Made with GeoGebra®) – maybe put it into acknowledgments next
1191 to the MetaCentrum credit? And list all of the figures where GeoGebra was
1192 used?
- 1193 • Maybe make some section outside of References specifically for literature?
1194 (such as the old CERN TPC review, ATOMKI review is currently not
1195 mentioned, not sure if some Wikipedia articles should get a mention or how
1196 do these things work)
- 1197 • Consistent use of `bm` vs `mathbf`

- Consistent use of $\bar{\mathcal{M}}$ instead of \mathcal{M} when talking about the map of the means (so most of the time)
 - Proper equation numbering when deriving a relation
 - Hugo should be mentioned somewhere in the title pages probably?
 - Consistent itemize/enumerate style (namely spacing) that looks good (ideally set by some macro? maybe the new MFF UK template will solve this?)
 - Consistent gas mixture notation (e.g., 90:10 Ar:CO₂). Maybe mention at the beginning that it is a molar ratio.
 - Labels of figures and tables – maybe in bold? Abbreviated?
 - Check graph labels, make them bigger if needed.
 - "The map" can be viewed as a mapping between spaces or just as a coordinate transform.
 - Maybe switch to cleverref.
 - siunitx qty not SI
 - Correct em dash?
 - In the future, it might be useful to save pictures as tex files whenever possible and using siunitx for the labels
- 1215 Random notes:
- Terminology consistency – ionization/primary/secondary electrons
 - Consistent TPC vs OFTPC acronym usage in the text or individual chapters.
 - Only electrons that start and end in the sector closer than 0.5 cm are used for reconstruction (newest version).
 - Attachment, Penning transfer and secondary ionization not considered in the microscopic simulation.
 - Suspicious artifacts of trilinear interpolation in Fig. 1.14. **Fixed – integers instead of doubles in the implementation, influenced reconstruction SIGNIFICANTLY (but not simulation).**
 - Profiling of the reconstruction!!!! Find out what's taking the most time (probably Runge-Kutta integration which the fit calls a lot). Could gradually decrease the step size to refine the fit instead of making it small right away (arbitrarily small – the effect of this was never tested). This could take some time to do properly (find a profiler or make profiling macros).
 - Slow drift velocity good for z reconstruction, too low leads to recombination
 - Could add link to the GitHub repository, mention CMake? Details about simulating on MetaCentrum?
 - The first used track had 8 MeV momentum $p = \gamma mv$ (not kinetic energy $E_{\text{kin}} = (\gamma - 1)mc^2 = \sqrt{p^2c^2 + m^2c^4} - mc^2 \approx 7.5$ MeV)

- Maybe cite Garfield++ user manual instead?
- Using TRandom3 for random number generation.
- Does the RK fit error correlate with the actual error?
- Some Garfield settings in micro track generation probably not mentioned

1240 Future

1241 Things planned for the future:

- Testing the reconstruction algorithm by measuring real particles with a known energy distribution (at first just laser, muons?).
- The **Fast Simulation with Ionization Electron Map** is planned for the future. It will use the HEED program [44] to simulate the primary particle and the Ionization Electron Map (see Section 3.2) to simulate the drift of secondary electrons. It should be significantly faster than the Microscopic Simulation but offer comparable precision since it will rely on an already simulated drift map. (Primary track simulated in HEED. Readout parameters by interpolating the map. Diffusion from the map for randomization.)
- Account for GEM, delta electrons, ...
- Likelihood approach instead of least squares (if it improves the reconstruction significantly), we should at least use a better method than taking the center of the TPC bin.
- More detailed electric field simulation (if needed, GEM will have more complex field, some irregularities in the field should be considered)
- Account for the triggering in MWPC/TPX3 (particle travels from TPX3 to MWPC basically immediately – fraction of a nanosecond so there should be no significant difference)

1260

1261 Likelihood - inverse map

1262 If we wanted to further improve this procedure, taking into account the whole
 1263 map \mathcal{M} , we could make an "inverse map" from \mathcal{R} to distributions on \mathcal{D} . We could
 1264 achieve this by taking the normalized probability density of an electron with initial
 1265 coordinates (x, y, z) having readout coordinates (x', y', t) . If we fix (x', y', t) , we
 1266 get an unnormalized probability density $f(x, y, z) = \mathcal{M}_{(x,y,z)}(x', y', t)$ (assuming
 1267 that all initial coordinates are a priori equally likely). This could potentially
 1268 improve the discrete reconstruction if we take the mean value of this probability
 1269 density across the pad and time bin

$$f_{\text{pad, bin}}(x, y, z) = \frac{1}{A_{\text{pad}} \Delta t_{\text{bin}}} \int_{\text{pad, bin}} \mathcal{M}_{(x,y,z)}(x', y', t) dx' dy' dt \quad (4.33)$$

1270 and using it for a likelihood fit instead of using least squares. This still assumes
 1271 that all initial coordinates are equally likely which is clearly not the case for

1272 a primary particle track. In the future, we could even use the fast track simulation
1273 with the map (should be possible to make around 1000 tracks per minute per core
1274 with current settings), create a big set of tracks with reasonable parameters and
1275 use these to get an approximation of the probability distribution of the detector
1276 response. Some approximations would be necessary when interpreting the data to
1277 decrease the degrees of freedom of this distribution (we would have to pick a set of
1278 parameters and assume that some of them are independent). This could give us
1279 an idea about the best achievable resolution (how significantly will the detector
1280 response differ for a given change in energy). If the difference is significant, we
1281 could try to further improve the likelihood fit.

¹²⁸² Bibliography

- ¹²⁸³ 1. *Garfield++* [<https://garfieldpp.web.cern.ch/garfieldpp/>]. [N.d.]. Accessed: 2023-05-18.
- ¹²⁸⁵ 2. BRUN, Rene; RADEMAKERS, Fons. Root — An Object Oriented Data Analysis Framework. *Nucl. Instrum. Methods Phys. Res. Sect. A: Accel. Spectrom. Detect. Assoc. Equip.* 1997, vol. 389, no. 1–2, pp. 81–86. Available from DOI: 10.1016/s0168-9002(97)00048-x. Proceedings AIHENP'96 Workshop, Lausanne, Sep. 1996, See also <https://root.cern/>, Paper published in the Linux Journal, Issue 51, July 1998.
- ¹²⁹¹ 3. *About MetaCentrum* [<https://metavo.metacentrum.cz/en/about/index.html>]. 2023. Accessed: 2024-11-27.
- ¹²⁹³ 4. ROSE, M. E. Internal Pair Formation. *Phys. Rev.* 1949, vol. 76, pp. 678–681. Available from DOI: 10.1103/PhysRev.76.678.
- ¹²⁹⁵ 5. ESSIG, R. et al. *Dark Sectors and New, Light, Weakly-Coupled Particles*. 2013. Available from arXiv: 1311.0029 [hep-ph].
- ¹²⁹⁷ 6. DE BOER, F.W.N. et al. A deviation in internal pair conversion. *Phys. Lett. B*. 1996, vol. 388, no. 2, pp. 235–240. ISSN 0370-2693. Available from DOI: [https://doi.org/10.1016/S0370-2693\(96\)01311-1](https://doi.org/10.1016/S0370-2693(96)01311-1).
- ¹³⁰⁰ 7. BOER, F W N de et al. Excess in nuclear pairs near 9 MeV/ invariant mass. *J. Phys. G: Nucl. Part. Phys.* 1997, vol. 23, no. 11, p. L85. Available from DOI: 10.1088/0954-3899/23/11/001.
- ¹³⁰³ 8. BOER, F W N de et al. Further search for a neutral boson with a mass around 9 MeV/c². *J. Phys. G: Nucl. Part. Phys.* 2001, vol. 27, no. 4, p. L29. Available from DOI: 10.1088/0954-3899/27/4/102.
- ¹³⁰⁶ 9. VITÉZ, Attila et al. Anomalous Internal Pair Creation in ⁸Be as a Signature of the Decay of a New Particle. *Acta Phys. Pol. B - ACTA PHYS POL B*. 2008, vol. 39, p. 483.
- ¹³⁰⁹ 10. KRASZNAHORKAY, A. et al. Searching for a light neutral axial-vector boson in isoscalar nuclear transitions. *Frascati Phys. Ser.* 2012, vol. 56, p. 86.
- ¹³¹¹ 11. KRASZNAHORKAY, A. J. et al. Observation of Anomalous Internal Pair Creation in ⁸Be: A Possible Indication of a Light, Neutral Boson. *Phys. Rev. Lett.* 2016, vol. 116, no. 4. ISSN 1079-7114. Available from DOI: 10.1103/physrevlett.116.042501.
- ¹³¹⁵ 12. TILLEY, D.R. et al. Energy levels of light nuclei A=8,9,10. *Nucl. Phys. A*. 2004, vol. 745, no. 3, pp. 155–362. ISSN 0375-9474. Available from DOI: <https://doi.org/10.1016/j.nuclphysa.2004.09.059>.
- ¹³¹⁸ 13. SAS, N. J. et al. *Observation of the X17 anomaly in the ⁷Li(p,e⁺e⁻)⁸Be direct proton-capture reaction*. 2022. Available from arXiv: 2205.07744 [nucl-ex].
- ¹³²¹ 14. KRASZNAHORKAY, A. J. et al. New anomaly observed in ⁴He supports the existence of the hypothetical X17 particle. *Phys. Rev. C*. 2021, vol. 104, no. 4. ISSN 2469-9993. Available from DOI: 10.1103/physrevc.104.044003.

- 1324 15. TILLEY, D.R. et al. Energy levels of light nuclei A = 4. *Nucl. Phys. A*.
1325 1992, vol. 541, no. 1, pp. 1–104. ISSN 0375-9474. Available from DOI: [https://doi.org/10.1016/0375-9474\(92\)90635-W](https://doi.org/10.1016/0375-9474(92)90635-W).
- 1326
1327 16. KRASZNAHORKAY, A. J. et al. New anomaly observed in ^{12}C supports the
1328 existence and the vector character of the hypothetical X17 boson. *Phys. Rev.*
1329 *C*. 2022, vol. 106, p. L061601. Available from DOI: 10.1103/PhysRevC.106.
1330 L061601.
- 1331 17. AJZENBERG-SELOVE, F. Energy levels of light nuclei A = 11,12. *Nucl. Phys.*
1332 *A*. 1990, vol. 506, no. 1, pp. 1–158. ISSN 0375-9474. Available from DOI:
1333 [https://doi.org/10.1016/0375-9474\(90\)90271-M](https://doi.org/10.1016/0375-9474(90)90271-M).
- 1334 18. KÁLMÁN, Péter; KESZTHELYI, Tamás. Anomalous internal pair creation.
1335 *The Eur. Phys. J. A*. 2020, vol. 56. Available from DOI: 10.1140/epja/
1336 s10050-020-00202-z.
- 1337 19. ALEKSEJEVS, A. et al. *A Standard Model Explanation for the "ATOMKI*
1338 *Anomaly"*. 2021. Available from arXiv: 2102.01127 [hep-ph].
- 1339 20. FENG, Jonathan L. et al. Protophobic Fifth-Force Interpretation of the Ob-
1340 served Anomaly in ^8Be Nuclear Transitions. *Phys. Rev. Lett.* 2016, vol. 117,
1341 p. 071803. Available from DOI: 10.1103/PhysRevLett.117.071803.
- 1342 21. ANH, Tran The et al. Checking the 8Be Anomaly with a Two-Arm Electron
1343 Positron Pair Spectrometer. *Universe*. 2024, vol. 10, no. 4, p. 168. ISSN 2218-
1344 1997. Available from DOI: 10.3390/universe10040168.
- 1345 22. ABRAAMYAN, Kh. U. et al. *Observation of structures at ~ 17 and ~ 38 MeV/c 2*
1346 *in the $\gamma\gamma$ invariant mass spectra in pC, dC, and dCu collisions at p_{lab} of a*
1347 *few GeV/c per nucleon*. 2023. Available from arXiv: 2311.18632 [hep-ex].
- 1348 23. THE MEG II COLLABORATION et al. *Search for the X17 particle in $^7\text{Li}(p, e^+e^-)^8\text{Be}$*
1349 *processes with the MEG II detector*. 2024. Available from arXiv: 2411.07994
1350 [nucl-ex].
- 1351 24. HILKE, H J. Time Projection Chambers. *Rep. Prog. Phys.* 2010, vol. 73, no.
1352 11, p. 116201. Available from DOI: {10.1088/0034-4885/73/11/116201}.
- 1353 25. NAVAS, S. et al. Review of particle physics. *Phys. Rev. D*. 2024, vol. 110,
1354 no. 3, p. 030001. Available from DOI: 10.1103/PhysRevD.110.030001.
- 1355 26. ABED ABUD, Adam et al. A Gaseous Argon-Based Near Detector to En-
1356 hance the Physics Capabilities of DUNE. 2022. Available from DOI: 10.
1357 48550/arXiv.2203.06281.
- 1358 27. AIHARA, H. et al. Spatial Resolution of the PEP-4 Time Projection Cham-
1359 ber. *IEEE Trans. on Nucl. Sci.* 1983, vol. 30, no. 1, pp. 76–81. Available
1360 from DOI: 10.1109/TNS.1983.4332223.
- 1361 28. LOKEN, Stewart C. et al. Performance of the Signal Processing System for
1362 the Time Projection Chamber. *IEEE Trans. on Nucl. Sci.* 1983, vol. 30, no.
1363 1, pp. 162–166. Available from DOI: 10.1109/TNS.1983.4332243.
- 1364 29. COWAN, G. D. *Inclusive π^\pm , K^\pm , and p , \bar{p} production in e^+e^- annihilation*
1365 *at $\sqrt{s} = 29$ GeV*. 1988. Available from DOI: 10.2172/5188194. Lawrence
1366 Berkeley National Lab. (LBNL), Berkeley, CA (United States).

- 1367 30. ALME, J. et al. The ALICE TPC, a large 3-dimensional tracking device
1368 with fast readout for ultra-high multiplicity events. *Nucl. Instrum. Methods*
1369 *Phys. Res. Sect. A: Accel. Spectrom. Detect. Assoc. Equip.* 2010, vol. 622,
1370 no. 1, pp. 316–367. ISSN 0168-9002. Available from DOI: <https://doi.org/10.1016/j.nima.2010.04.042>.
- 1372 31. HAUER, Philip. The upgraded ALICE TPC. *Nucl. Instrum. Methods Phys.*
1373 *Res. Sect. A: Accel. Spectrom. Detect. Assoc. Equip.* 2022, vol. 1039, p. 167023. ISSN 0168-9002. Available from DOI: <https://doi.org/10.1016/j.nima.2022.167023>.
- 1376 32. DI MAURO, A. Particle identification methods other than RICH. *Nucl. Instrum.*
1377 *Methods Phys. Res. Sect. A: Accel. Spectrom. Detect. Assoc. Equip.* 2020, vol. 952, p. 162124. ISSN 0168-9002. Available from DOI: <https://doi.org/10.1016/j.nima.2019.04.078>. 10th International Workshop on
1379 Ring Imaging Cherenkov Detectors (RICH 2018).
- 1381 33. ADAMOVÁ, D. et al. The CERES/NA45 radial drift Time Projection Chamber.
1382 *Nucl. Instrum. Methods Phys. Res. Sect. A: Accel. Spectrom. Detect.*
1383 *Assoc. Equip.* 2008, vol. 593, no. 3, pp. 203–231. ISSN 0168-9002. Available
1384 from DOI: [10.1016/j.nima.2008.04.056](https://doi.org/10.1016/j.nima.2008.04.056).
- 1385 34. BIAGI, S.F. Monte Carlo simulation of electron drift and diffusion in counting
1386 gases under the influence of electric and magnetic fields. *Nucl. Instrum.*
1387 *Methods Phys. Res. Sect. A: Accel. Spectrom. Detect. Assoc. Equip.* 1999,
1388 vol. 421, no. 1, pp. 234–240. ISSN 0168-9002. Available from DOI: [https://doi.org/10.1016/S0168-9002\(98\)01233-9](https://doi.org/10.1016/S0168-9002(98)01233-9).
- 1390 35. ALBAYRAK, I. et al. Design, construction, and performance of the GEM
1391 based radial time projection chamber for the BONuS12 experiment with
1392 CLAS12. *Nucl. Instrum. Methods Phys. Res. Sect. A: Accel. Spectrom. Detect.*
1393 *Assoc. Equip.* 2024, vol. 1062, p. 169190. ISSN 0168-9002. Available from
1394 DOI: <https://doi.org/10.1016/j.nima.2024.169190>.
- 1395 36. ANDERSON, E. et al. Observation of the effect of gravity on the motion of
1396 antimatter. *Nature*. 2023, vol. 621, pp. 716–722. Available from DOI: [10.1038/s41586-023-06527-1](https://doi.org/10.1038/s41586-023-06527-1).
- 1398 37. Design of a Radial TPC for Antihydrogen Gravity Measurement with ALPHA-g. In: *Proceedings of the 12th International Conference on Low Energy Antiproton Physics (LEAP2016)*. [N.d.]. Available from DOI: [10.7566/JPSCP.18.011015](https://doi.org/10.7566/JPSCP.18.011015).
- 1402 38. CAPRA, A. Antihydrogen annihilation detection: the ALPHA-g radial TPC.
1403 *PoS*. 2025, vol. EXA-LEAP2024, p. 063. Available from DOI: [10.22323/1.480.0063](https://doi.org/10.22323/1.480.0063).
- 1405 39. WIECHULA, Jens; CHRISTIANSEN, Peter. *The ALICE Time Projection Chamber* [https://www.hep.lu.se/staff/christiansen/teaching/spring_2013/the_alice_tpc.pdf]. 2013. Slides credited to J. Wiechula; hosted on
1406 Lund University website.

- 1409 40. HILDÉN, T. et al. Optical quality assurance of GEM foils. *Nucl. Instrum.*
1410 *Methods Phys. Res. Sect. A: Accel. Spectrom. Detect. Assoc. Equip.* 2015,
1411 vol. 770, pp. 113–122. ISSN 0168-9002. Available from DOI: 10.1016/j.nima.2014.10.015.
- 1412
- 1413 41. AHMED, Misbah Uddin. *Simulation of the electron and ion movement through a 4-GEM stack.* 2021. Institut für Kernphysik.
- 1414
- 1415 42. MARMELAD. *3D interpolation2.svg.* 2025. Available also from: https://commons.wikimedia.org/wiki/File:3D_interpolation2.svg. Licensed
1416 under CC BY-SA 3.0 (<https://creativecommons.org/licenses/by-sa/3.0/legalcode>). Accessed: 9-April-2025.
- 1417
- 1418
- 1419 43. CMGLEE. *Trilinear interpolation visualisation.* 2025. Available also from:
1420 https://commons.wikimedia.org/wiki/File:Trilinear_interpolation_visualisation.svg. Licensed under CC BY-SA 3.0 (<https://creativecommons.org/licenses/by-sa/3.0/legalcode>). Accessed: 26-March-2025.
- 1421
- 1422
- 1423 44. SMIRNOV, I.B. Modeling of ionization produced by fast charged particles in
1424 gases. *Nucl. Instrum. Methods Phys. Res. Sect. A: Accel. Spectrom. Detect.*
1425 *Assoc. Equip.* 2005, vol. 554, no. 1, pp. 474–493. ISSN 0168-9002. Available
1426 from DOI: <https://doi.org/10.1016/j.nima.2005.08.064>.

1427 **Acknowledgments:** Computational resources were provided by the e-INFRA
1428 CZ project (ID:90254), supported by the Ministry of Education, Youth and Sports
1429 of the Czech Republic. **Figures that were drawn with GeoGebra. Maybe grant?**

1430 List of Figures

1431	0.1	The ATOMKI anomalous IPC measured for different nuclei.	5
1432	0.2	Results from the Hanoi spectrometer – angular e^+e^- pair correlations measured in the ${}^7\text{Li}(p, e^+e^-){}^8\text{Be}$ reaction at $E_p = 1225$ keV [21].	6
1433	0.3	Results from the MEG II experiments – angular correlation of e^+e^- pairs with $E_{\text{sum}} \in [16, 20]$ MeV measured in the ${}^7\text{Li}(p, e^+e^-){}^8\text{Be}$ reaction with proton beam energies 500 and 1080 keV. The 500 keV dataset is fitted with Monte Carlo of both the IPC deexcitation and the EPC produced by gammas [23].	7
1434	0.4	Schematics of the detector at the Van der Graaff facility at IEAP CTU (ref).	7
1440	1.1	Particle identification in the PEP-4 TPC at SLAC based on the energy loss per distance $\frac{dE}{dx}$ in the 80:20 Ar:CH ₄ filling at 8.5 atm pressure [26]. <small>The reference doesn't point to the original PEP-4 article because this adapted version of the original picture that they used in the DUNE article looks better.</small>	9
1441	1.2	Schematic view of the PEP-4 TPC [28]. A charged particle produced in a collision in the beam pipe creates a spiral ionization track in the magnetic field. The central cathode then accelerates ionization electrons towards the endcap anode wires where they are multiplied and read out. A TPC sector with a detailed view of one of the pad rows is shown on the right [29].	12
1442	1.3	Schematic view of the ALICE TPC [31]. The readout at each endcap is divided into 18 sectors, each subdivided into an Inner Readout Chamber (IROC) with one GEM stack and Outer Readout Chamber (OROC) with three GEM stacks. A visualization of a GEM stack is on the right [32].	13
1443	1.4	Experimental setup of the CERES/NA45 experiment with two Ring Imaging Cherenkov Counters (RICHs) on the left and a rTPC on the right. The magnetic field (red) is generated by two solenoidal coils (blue) with opposite polarity. Produced ionization electrons drift outward radially towards the readout chamber (yellow) [33].	14
1444	1.5	Cross section of a CERES/NA45 readout MWPC. The wires are stretched in the azimuthal direction above the pad plane. The gating grid controls the passage of electrons and ions. [33].	14
1445	1.6	Schematic view of the BONuS12 rTPC [35].	15
1446	1.7	Schematic view of the ALPHA-g detector [37].	16
1447	1.8	Schematic view of the ALICE MWPC readout (working principle) [39].	17
1448	1.9	Gas Electron Multiplier (GEM).	18
1449	1.10	Garfield simulation of an avalanche in a GEM hole [41]. An incoming electron (orange) is accelerated in the strong electric field of the GEM and causes further ionization multiplying the number of free electrons (orange). Most of the produced cations (red) are captured by the GEM cathode.	18
1450	1.11	MICRO-MEsh GAseous Structure (Micromegas) [25].	19

1475	1.12 Schematics of the first sector OFTPC with detector space coordinates.	21
1476		
1477	1.13 Pad layout of the OFTPC and its parameters. Pads 102, 124 and 127 are irregular, the rest has the same dimensions.	22
1478		
1479	1.14 Magnetic field simulation results. The OFTPC volume and the vacuum tube are marked with black lines, the magnets are marked with red lines. The coordinates of the magnets from the CAD drawing seem to be 9/10 of the ones from the magnetic simulation (confirm and fix).	23
1480		
1481		
1482		
1483		
1484	1.15 Visualization of trilinear interpolation as a composition of linear interpolations (inspired by [42]). We want to interpolate the value in the red point C . First we interpolate between the four pairs of blue points sharing the last two indices along the x -axis (Eq. 1.15), then between the two pairs of the resulting green points along the y -axis (Eq. 1.16) and finally between the two resulting orange points along the z -axis to get the final red value (Eq. 1.17).	24
1485		
1486		
1487		
1488		
1489		
1490		
1491	1.16 Geometric interpretation of trilinear interpolation as expressed in Equation 1.19. The colored dots represent the values in given points and the colored boxes represent the volume in the opposite corner by which the corresponding values are multiplied. The black dot represents the interpolated value which is multiplied by the entire volume [43].	25
1492		
1493		
1494		
1495		
1496		
1497	2.1 Comparison of drift lines for two different gas mixtures 90:10 and 70:30 Ar:CO ₂ . The electron track is marked in black, the drift lines of the ionization electrons are marked in orange. In this example, we assume a larger OFTPC volume with readout at $z = 8$ cm.	28
1498		
1499		
1500		
1501	2.2 A visualization of a set of tracks from the grid-like testing sample with the same kinetic energy.	29
1502		
1503	2.3 A comparison of the HEED track from the microscopic simulation in Section 2.1.1 with a Runge-Kutta track with the same initial parameters and $\tau_{\text{step}} = 0.1$ ps (reducing the step further doesn't make a visible difference). In the view of the tracks on the left, the distance of the HEED ionization electrons from the RK4 track is exaggerated 1000 \times . On the right, the dependence of the HEED electrons residuals (i.e., their shortest distance to the RK4 track) on their z -coordinate is shown. The images look the same even for 100,000x smaller step, so the residuals are a result of something that HEED does (maybe a different interpolation technique for the magnetic field? the pattern looks similar for two different tracks so it can't be scattering).	31
1504		
1505		
1506		
1507		
1508		
1509		
1510		
1511		
1512		
1513		
1514		
1515	3.1 Linear fit of the drift time t dependence on the distance to the readout $d_r = 8$ cm – z for the ionization electrons in 90:10 (left) and 70:30 (right) Ar:CO ₂ gas composition. Only electrons inside the TPC (red) are fitted. The parameters are $v_d = 3.39$ cm/ μ s, $d_0 = -0.41$ cm for 90:10, and $v_d = 0.939$ cm/ μ s, $d_0 = -0.11$ cm for 70:30 Ar:CO ₂	33
1516		
1517		
1518		
1519		
1520		

1521	3.2 Reconstruction (black) of the starting position of ionization elec-	
1522	trons (red) using parameters obtained from the fit (Fig. 3.1). Two	
1523	gas compositions 90:10 (left) and 70:30 Ar:CO ₂ (right) are compared.	34
1524	3.3 Comparison of residuals (i.e., the distance from the reconstructed	
1525	point to the simulated ionization electron starting point) dependence	
1526	on x for two gas mixtures 90:10 (red) and 70:30 Ar:CO ₂	
1527	(blue).	34
1528	3.4 A 3D visualization of the mapping of means $\bar{\mathcal{M}}$ for the 90:10	
1529	Ar:CO ₂ gas. A regular grid \mathbb{G} with $l = 1$ cm in the detector space	
1530	is mapped to an irregular grid $\mathbb{G}^{-1} \equiv \bar{\mathcal{M}}(\mathbb{G})$ in the readout space.	35
1531	3.5 A test of the 90:10 Ar:CO ₂ map simulation with spacing $l = 1.5$ cm.	
1532	The resulting drift lines of evenly spaced electrons are displayed in	
1533	orange.	36
1534	3.6 Dependence of the drift times of the simulated map $\bar{\mathcal{M}}$ on the	
1535	z -coordinate. Two gas mixtures 90:10 (left) and 70:30 Ar:CO ₂	
1536	(right) are compared. The spread is caused by varying Lorentz	
1537	angles.	37
1538	3.7 The $x't$ projection of the $\mathcal{M}(\mathbb{G}_{y=0})$ mapping of a part of the regu-	
1539	lar grid \mathbb{G} . The means $\bar{\mathcal{M}}(\mathbb{G}_{y=0})$ are marked with red crosses, and	
1540	the diffusion error is denoted by black 95% confidence error ellipses	
1541	computed from the diagonalized covariance matrices $\mathcal{M}_\Sigma(\mathbb{G}_{y=0})$.	
1542	Two gas mixtures 90:10 (left) and 70:30 Ar:CO ₂ (right) are com-	
1543	pared. The first mixture shows differences of t for electrons with	
1544	same initial z but different initial x . For the second mixture, these	
1545	differences are negligible in comparison with the diffusion.	37
1546	3.8 The regular grid \mathbb{G} projected by the mapping $\bar{\mathcal{M}}$ from the detector	
1547	space onto the $x'y'$ plane (t is not plotted). Layers with lower	
1548	z -coordinate (i.e., further away from the readout) are displayed	
1549	with darker colors. The OFTPC volume is marked with black	
1550	lines. Two gas mixtures 90:10 (left) and 70:30 Ar:CO ₂ (right) are	
1551	compared.	38
1552	3.9 The $\mathcal{M}(\mathbb{G}_{-8})$ mapping of the bottom ($z = -8$ cm) layer \mathbb{G}_{-8} of the	
1553	regular grid $\mathbb{G} \subset \mathcal{D}$. It includes both the mapping of means $\bar{\mathcal{M}}$ and	
1554	of covariances \mathcal{M}_Σ . Individual electrons from the map simulation	
1555	are marked with red dots. Two gas mixtures 90:10 (left) and 70:30	
1556	Ar:CO ₂ (right) are compared.	38
1557	3.10 The readout coordinate x' for points on the grid $\mathbb{G}_{y=0}$ plotted	
1558	against their initial coordinate z . The means are marked with red	
1559	crosses, the diffusion in x' is denoted by standard error bars. Two	
1560	gas mixtures 90:10 (left) and 70:30 Ar:CO ₂ (right) are compared.	39
1561	3.11 Example reconstruction with the map. Swap for better image, cor-	
1562	rect coordinates.	40
1563	3.12 Selection of the points for interpolation. Create better images; use	
1564	the explanation interpolation vs. extrapolation strange property.	
1565	Solution 2 probably does not make much sense.	43
1566	4.1 Example of a fitted reconstructed track. Swap for better image. . .	45

1567	4.2	First attempt at a track reconstruction using only the drift velocity. Spline energy reconstruction attempt. Swap for better image(s) – subfigure environment, correct coordinates.	47
1569			
1570	4.3	First attempt at a track reconstruction using only the drift veloc- ity. Circle and Lines Fit in 2D. Swap for better image, correct coordinates. Bias should be described in the previous chapter, not here.	49
1571			
1572	4.4	Visualization of the 3D geometry of the Circle and Lines Fit and its parameters.	50
1573			
1574	4.5	Demonstration of the convexity of the distance function $d(\alpha)$ for a circular track (see Equation 4.29).	53
1575			
1576	4.6	An example track (red) with a polygonal chain approximation (green, representing a RK4 simulation). The distance of the point \mathbf{P} from the chain is found using a binary search among the distances to the vertices $d_{\mathbf{P}}(\tau_i)$ (blue) and subsequently calculating the dis- tance to segments neighboring the found vertex (thus finding the minimum of the function $d'_{\mathbf{P}}(\tau)$, function $d_{\mathbf{P}}(\tau)$ for the actual track is showed for reference). This approach works if the condition 4.28 is satisfied, which is not the case for a point from the green area bordered by the normals at endpoints and the evolute of the track (orange).	54
1577			
1578	4.7	An exclusion area (green) of a track (red) bordered by its evolute and the normals at endpoints (orange), where the assumption 4.28 is violated. Unlike the track in Fig. 4.6, this track has a minimal curvature point in the middle, corresponding to the cusp on its evolute.	55
1579			
1580			
1581			
1582			
1583			
1584			
1585			
1586			
1587			
1588			
1589			
1590			
1591			
1592			

List of Tables

1593	3.1 Comparison of parameters of two map simulations.	36
------	--	----

¹⁵⁹⁵ List of Abbreviations

- ¹⁵⁹⁶ **ALPHA** Antihydrogen Laser Physics Apparatus
- ¹⁵⁹⁷ **BONuS12** Barely Off-shell NeUtron Structure 12 GeV
- ¹⁵⁹⁸ **GEM** Gas Electron Multiplier
- ¹⁵⁹⁹ **HEED** High Energy Electro-Dynamics
- ¹⁶⁰⁰ **IEAP CTU** Institute of Experimental and Applied Physics, Czech Technical
¹⁶⁰¹ University in Prague
- ¹⁶⁰² **IPC** Internal Pair Creation
- ¹⁶⁰³ **EPC** External Pair Creation
- ¹⁶⁰⁴ **LArTPC** Liquid Argon TPC
- ¹⁶⁰⁵ **Micromegas** MICRO-MEsh Gaseous Structure
- ¹⁶⁰⁶ **MPGD** Micro-Pattern Gaseous Detector
- ¹⁶⁰⁷ **MWPC** Multi-Wire Proportional Chamber
- ¹⁶⁰⁸ **OFTPC** Orthogonal Fields TPC
- ¹⁶⁰⁹ **PCB** Printed Circuit Board
- ¹⁶¹⁰ **RICH** Ring Imaging Cherenkov Counter
- ¹⁶¹¹ **RK4** Runge-Kutta 4th order
- ¹⁶¹² **RPC** Resistive Plate Chamber
- ¹⁶¹³ **RPWELL** Resistive Plate WELL
- ¹⁶¹⁴ **rTPC** radial-drift TPC
- ¹⁶¹⁵ **THGEM** THick GEM
- ¹⁶¹⁶ **ToA** time-of-arrival
- ¹⁶¹⁷ **ToT** time-over-threshold
- ¹⁶¹⁸ **TPC** Time Projection Chamber
- ¹⁶¹⁹ **TPX3** Timepix3
- ¹⁶²⁰ **μ -PIC** Micro-Pixel Gas Chamber
- ¹⁶²¹ **μ -RWELL** Micro-RWELL